Development of Elastomeric Optofluidic Devices for Lasing and Sensing

THÈSE N^{O} 5451 (2012)

PRÉSENTÉE LE 31 AOÛT 2012

À LA FACULTÉ DES SCIENCES ET TECHNIQUES DE L'INGÉNIEUR

LABORATOIRE D'OPTIQUE

PROGRAMME DOCTORAL EN PHOTONIQUE

ÉCOLE POLYTECHNIQUE FÉDÉRALE DE LAUSANNE

POUR L'OBTENTION DU GRADE DE DOCTEUR ÈS SCIENCES

PAR

Wuzhou SONG

acceptée sur proposition du jury:

Prof. C. Moser, président du jury
Prof. D. Psaltis, directeur de thèse
Prof. A. Kristensen, rapporteur
Prof. J. Perruisseau-Carrier, rapporteur
Prof. D. Rabus, rapporteur

ÉCOLE POLYTECHNIQUE
FÉDÉRALE DE LAUSANNE

Suisse
2012

To my parents, to whom I owe what I am,

to my sisters I could ever have had,

to my teachers and friends,

Many thanks!

Acknowledge

First of all, I would like to thank my thesis adviser **Prof. Demetri Psaltis** for giving me the opportunity to pursue research in his group. He can always motivate my research interest and strongly support my research activity. I also appreciate his valuable input in many aspects of science, life and human interaction. Absolutely my study in Switzerland is my precious experience in all my life. Meanwhile, many thanks go to **all my colleagues** in our lab, particularly to **Dr. Andreas Vasdekis** who gave me much guidance at beginning on the optofluidic dye laser projects, eventually we have built a deep friendship through our numeric discussions and arguments. Our lab is a big harmonic group; we often exchanged our different opinions, helped each other and we have shared a fruitful time in the past 4 years. I am grateful to **CMI staffs** for their patient and assistance in teaching me and helping to solve many technical issues. I am also grateful to **Dr. Catana Andre** from the Technology Transfer Office (SRI EPFL) who gave me lots of substantial support to file the patent and make an elegant demo for it. He also helped us to build a close relationship with our industry partner in order to commercialize the patent. Thanks to **Mr. Charles Dubout** who is a PhD candidate in computer science. He helped me to develop software for the demo kit regarding the patent. I appreciate the help from **Prof. Jürgen Brugger** and **Prof. Martinus Gijs** who supported my application of SNSF fellowship. I am also grateful to **many other professors and staff in EPFL** who have taught me and helped me. In addition, I'd like to express my thanks to **all of my friends**; I will cherish all the happiness forever that we have shared in the past. Finally, my gratitude and love go to **my family**, for their deep love, silent care and consistent inspiration on me.

Abstract

The term of optofluidics defines an emergent research field that combines microfluidics and optics. In many lab-on-a-chip applications, these two technologies are used in combining the microfluidics for sample delivery and optics for sensing and controlling. Optofluidic represents the implementation of optics in microfluidic platform that produces an unprecedented level of integration. Moreover, optofluidic devices are easily and highly reconfigurable, which can be a significant advantage to the traditional solid optical components.

As an elastomer, PDMS (polydimethylsiloxane) is one of the most popular materials in microfluidics. It exhibits excellent elasticity, bio-compatibility and optical transparence. Most microfluidic chips are made of PDMS using soft lithography. And multi-layer soft lithography has enabled large-scale integration of monolithic microfluidic valves and pumps on a single chip. Thus to develop the optofluidic elements within PDMS microfluidic chip is one of the most promising and desirable ways towards further integration of optofluidic and microfluidic functions together for more complex lab-on-a-chip applications.

During my doctoral research, we worked on a batch of optofluidic devices that are based on PDMS material and soft lithography. They include the optofluidic dye lasers, optofluidic interferometer, optofluidic switch, and optofluidic differential spectroscopy. Such optofluidic elements provide a broad spectrum of toolbox with different optical functions that can be easily into many other PDMS microfluidic chips. They are compatible to the conventional PDMS microfluidic chip in terms of fabrication, operation and control. And they could provide important optical functions in lab-on-a-chip systems. For examples, the optofluidic dye laser can be integrated as a widely tunable coherent source for chip-scale fluorescence spectroscopy or cell flow cytometry. The optofluidic membrane interferometer can be easily integrated into conventional PDMS microfluidic chip for multi-site pressure and flow monitoring with high precision. Optofluidic switch can compose a reconfigurable optical circuit on single microfluidic

chip. Optofluidic differential spectroscopy provides a simple and highly sensitive method for in-line measuring of solution concentration. Among these devices, we have also developed and summarized a series of novel optofluidic turning methods that are controlled by pneumatic actuation. These simple turning methods also take the advantages of high precision and reliability.

In addition to these elastomeric optofluidic devices, we are also working on several other optofluidic projects. In the last chapter of this thesis, we will give a partial preview of these works and also our perspective on the nano-optofluidics which represents a new trend of optofluidics.

Keywords:

Optofluidic, microfluidic, optics, microfabrication, nanofabrication, PDMS, dye laser, pressure sensor, optical switch, spectroscopy and lab on a chip

Résumé

La durée de optofluidics définit un domaine de recherche émergent qui combine la microfluidique et de l'optique. Dans de nombreux laboratoires sur une puce les applications, ces deux technologies sont utilisées dans la combinaison des microfluidique pour la livraison d'échantillons et de l'optique pour la détection et le contrôle. Optofluidic représente la mise en œuvre de la plate-forme microfluidique dans l'optique qui produit un niveau d'intégration sans précédent. En outre, les dispositifs optofluidic sont facilement et très reconfigurable, qui peut être un avantage significatif pour les traditionnelles solides composants optiques.

Comme un élastomère, le PDMS (polydiméthylsiloxane) est l'un des matériaux les plus populaires de la microfluidique. Il présente une excellente élasticité, la bio-compatibilité et la transparence optique. La plupart des puces microfluidiques sont en PDMS en utilisant la lithographie douce. Et multi-couche lithographie douce a permis intégration à grande échelle des vannes microfluidiques monolithiques et des pompes sur une seule puce. Ainsi, pour développer les éléments optofluidic au sein des puces microfluidiques en PDMS est l'un des moyens les plus prometteurs et souhaitable vers une intégration plus poussée des fonctions optofluidic et microfluidique ensemble depuis plus complexes lab-on-a-chip applications.

Au cours de ma recherche doctorale, nous avons travaillé sur un lot de dispositifs optofluidic qui sont basées sur le matériel PDMS et lithographie douce. Ils comprennent les lasers optofluidic teinture, l'interféromètre optofluidic, interrupteur optofluidic, et la spectroscopie différentielle optofluidic. Ces éléments optofluidic fournir un large éventail de boîte à outils avec différentes fonctions optiques qui peuvent être facilement dans de nombreux autres puces microfluidiques en PDMS. Ils sont compatibles avec la puce microfluidique PDMS classique en termes de fabrication, le fonctionnement et le contrôle. Et ils pourraient fournir d'importantes fonctions optiques dans le laboratoire-sur-une-puce systèmes. Pour des exemples, le laser

optofluidic colorant peut être intégré en tant que source largement accordable cohérente pour la puce échelle spectroscopie de fluorescence ou cytométrie en flux des cellules. L'interféromètre membrane optofluidic peut être facilement intégré dans conventionnelle PDMS des puces microfluidiques pour le multi-site de la pression et la surveillance du débit avec une grande précision. Commutateur optofluidic pouvez composer un circuit optique reconfigurable sur puce microfluidique unique. Spectroscopie différentielle optofluidic fournit une méthode simple et très sensible pour la mesure en ligne de concentration de la solution. Parmi ces dispositifs, nous avons également développé et résumé d'une série de nouvelles méthodes de tournage optofluidic qui sont contrôlées par commande pneumatique. Ces méthodes simples de tournage aussi prendre les avantages de haute précision et de fiabilité.

En plus de ces dispositifs en élastomère optofluidic, nous travaillons également sur plusieurs autres projets optofluidic. Dans le dernier chapitre de cette thèse, nous allons donner un aperçu partiel de ces travaux et aussi notre point de vue sur la nano-optofluidics qui représente une nouvelle tendance de optofluidics.

Mots-clés:

Optofluidic, microfluidique, l'optique, la microfabrication, la nanofabrication, PDMS, le laser à colorant, capteur de pression, optique commutateur, la spectroscopie et de laboratoire sur une puce

Contents

List of Figures

Chapter 1

Introduction

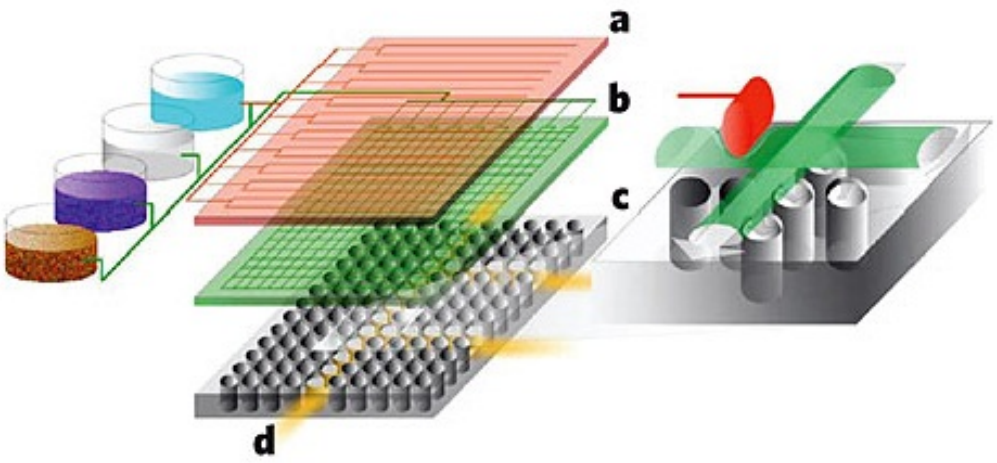

Figure 1.1: An artist rending of an integrated optofluidic device presented in year of 2006 [1]. The optofluidic device typically consists of three layers. a, The top layer consists of the microfluidic controls. b, The middle layer contains the microfluidic channels. c, The third layer is the optical structure and may contain photonic crystal structures, sensors, sources and waveguides. d, Light can be guided within the third layer.

During the last few years, as a multidisciplinary research field, optofluidic has been gaining significant progresses by combining the microfluidics with optical components and methods [1]. Although the idea of fluid-optical devices can be traced back at least as far as the 18th century, when spinning pools of mercury were proposed (and eventually developed) as liquid mirror telescopes. In the 20th century, such as dye lasers and liquid core waveguides were developed

and take advantages of the tunability and physical adaptability of liquids. The field of optofluidics formally began to emerge in the mid-2000s when the fields of microfluidics and micro/nano photonics were maturing and the researchers began to look for the synergies between these two areas [2-4]. Various methods have been used to implement optofluidic devices with recently developed microfluidic technologies that allow accurate control of liquids on small spatial scales. And optofluidics represents the combining of microfluidics and optics in an unprecedented level.

Integration and reconfigurability are the two major advantages associated with optofluidics. Whereas microfluidics has made it possible to integrate multiple fluidic tasks on a chip, most optical components, such as the light source, sensors, lenses and waveguides, remained off the chip. Optofluidic integration combines the optics and microfluidics on a same chip by building the optics out of the same fluidic toolkit thus increases the portability and sensitivity of the whole device. The second advantage of optofluidics lies in the ease with which one can change the optical properties of the devices by manipulating the fluids. Optofluidics device has shown extreme capability for adaptation and tunability benefitted from the constructing materials of fluids. Liquids can hold a wide choice of different refractive index and nonlinear property. Specific refractive index can be easily realized by fluidic mixing. The liquids can be also doped with different gain or absorbing medium, such as fluorescence dye or plasmonic particle [5-6]. Meanwhile, the flowing liquid can naturally form optical quality smooth boundaries which are crucial for liquid-liquid waveguide [7-8]. Moreover, due to the inherent flowing property of liquid state, the shape of the fluid can be variable. For instance, by using the electrowetting effect, multiple tunable optofluidic devices have transformed into significant commercial successes, such as the tunable liquid lens and electronic papers [9-12]. In addition to the fluidic tuning, there is also a group of soft optofluidic devices which can be reshaped by applying an external force, hence changing the scale or position of optical boundary geometry. A typical example is the mechanical tunable optofluidic distributed feedback (DFB) dye laser, in

which the wavelength tuning can be achieved by compressing or stretching the PDMS based dye laser chip [13].

The significant impact on lab-on-a-chip domain is a strong driving force for the developing of optofluidics. For example, optical detection technologies are extensively utilized in the cell and molecular detection. Compared to electronic method, the optic methods mostly exhibit many advantages including the high sensitivity, non-contact, immune to electromagnetic interference, and multiplexed interrogation. Based on the joint between the optics and microfluidics, optofluidic devices have enabled a group of various novel optical functions for measuring or manipulating the liquid, matters and light [14-15].

It is worthy to notice that PDMS (Polydimethylsiloxane) is one of the most preferred materials for making the microfluidic devices. As a silicone elastomer, PDMS exhibits excellent elasticity and optical properties. PDMS is biocompatible [16], inexpensive, transparent (240 nm–1100 nm) with low autofluorescence [17], and it can be molded with resolution down to several nanometers using a modified chemical composition of PDMS [18]. PDMS has a refractive index of around 1.41 with a visible and negative thermo-optic coefficient corresponding to $dn/dT = -4.5 \times 10^{-4}\ ^{\circ}C^{-1}$ [19]. Figure 1.2 shows a typical fabrication process for a PDMS microfluidic chip. The PDMS replica was covalently attached to a glass substrate using a simple plasma treatment to form a sealed microfluidic device. Large-scale integration of monolithic microfluidic valves and pumps on PDMS chip has been realized by multilayer soft lithography [20]. Due to the excellent optical transparence of PDMS, many pioneering optofluidic efforts were made using PDMS chips, such as the integrated liquid waveguide and optofluidic microscope on chip [21-22]. Eventually PDMS has become the most popular and versatile material for both microfluidics and optofluidics. As an advantage of PDMS, it allows the integration of optofluidics with many other microfluidic components on a single PDMS chip, which is desirable to achieve a complex functions in a lab-on-a-chip system.

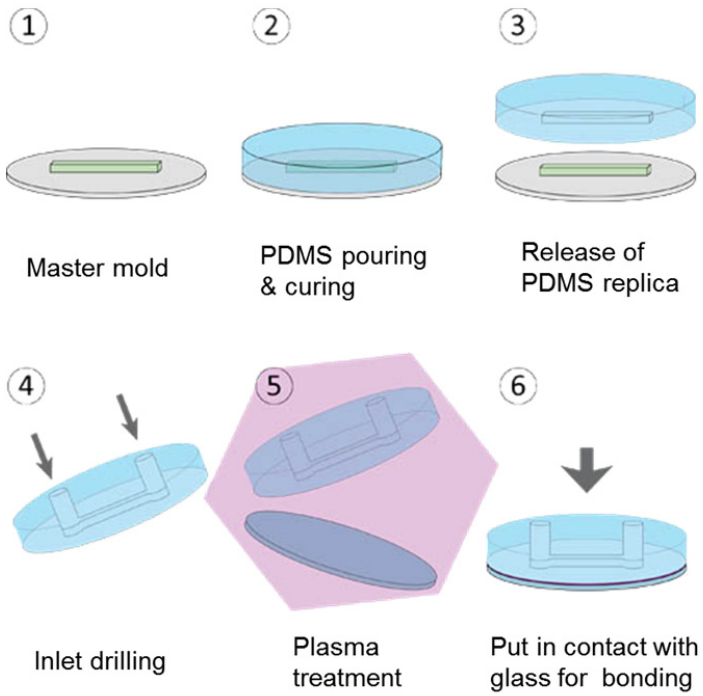

Figure 1.2: A typical fabrication process for a PDMS microfluidic chip.

In this thesis, we mainly focus on developing a broad spectrum of novel optofluidic devices based on PDMS and soft lithography. As a motivation of my work, those optofluidic devices are desired to be able to easily integrate into many other microfluidic chips for more advancing biological or optical functions.

At the beginning of my PhD research, we worked on optofluidic dye lasers which can be employed as a tunable laser source for chip-scale cell flow cytometry and fluorescence spectroscopy. Then we worked on the optofluidic interferometer which can be utilized as sensitive microfluidic pressure and flow sensors. It is compatible with most of PDMS based microfluidic chips due to the common in design and fabrication. Later we worked on planar optofluidic 2×2 switch, based on which we demonstrated a reconfigurable optical circuit on chip for dual channel spectroscopy. In the end, we worked on optofluidic differential spectroscopy which provides a simple but sensitive method for in-line measuring of solution's concentration.

Among these works, we developed a series of novel optofluidic turning methods with different scheme, but they are all based on the elastic property of the PDMS construction material. These optofluidic devices are either actively or passively tuned by the pressure force. For example, the tunable optofluidic dye laser, optofluidic switch and optofluidic modulator were all actively controlled by pneumatic pressure; the optofluidic interferometer was passively tuned by the fluidic pressure for sensing functions. From the experimental results, we found these pressure turning methods have decent precision and reliability. And such controlling methods turn out to be compatible with many microfluidic chips where the controlling on fluids is also realized by pneumatic or fluidic pressure.

In the last chapter of this thesis, I will give a preview of several other optofluidic projects that we are pursuing in addition to the elastomeric optofluidic devices. Meanwhile, I will also present our perspective on the nano-optofluidics.

Chapter 2

Low order distributed feedback optofluidic dye laser

In this chapter, we report the demonstration of low order distributed feedback (DFB) optofluidic dye lasers with reduced threshold. The laser chips were realized in polydimethylsiloxane (PDMS) using replica molding with two masters. A comparison between 1st, 2nd and 3rd order DFB dye laser was performed. All the lasers were longitudinally pumped and exhibited single mode operation, while the 2nd order DFB dye laser exhibited the lowest pump threshold of 78 nJ/pulse. Compared to the previous reports on higher order Bragg grating structures, this laser shows significantly reduced threshold owning to the reduction of the cavity losses and the more efficient pumping configuration.

In the developing of the optofluidic toolboxes for integrated optics and lab-on-a-chip applications, an open challenge is the integration of a tunable light source with microfluidic circuits. It is a key element towards a complete optical circuit on microfluidic chip platforms.[1-2, 23], To this end, optically pumped microfluidic dye lasers are of particular interest, since they exhibit the advantages of laser emission, combined with cost-effective processing and a wide choice of emission wavelengths. More importantly, they can be integrated with other microfluidic and optical devices towards complete lab-on-a-chip systems.

Several resonator configurations have been demonstrated for microfluidic dye lasers, such as the Fabry-Perot cavity [24], micro-droplet [25], capillary tube [26] and photonics crystal fiber [27], while the distributed feedback (DFB) resonators were the more efficient ones which enable narrow line-width single mode lasing operation and easy fabrication [28-29]. A DFB microfluidic dye laser was first demonstrated by Balslev et al. who used a 130^{th} order Brag grating in a multimode waveguide with a threshold of 20 μJ/pulse [28]. Then a pure single mode optofluidic dye laser with significant lower pump threshold of 3.2 μJ/pulse was achieved by Li et al [29]. It consists of a liquid core waveguide with an embedded phase shifted 15^{th} order DFB grating. However, microfluidic dye lasers still rely on bulky pumping laser systems due to their high thresholds, thus placing a restriction on their practicality. Hence, further reduction of the lasing threshold is highly desirable especially for compact diode pumping, as recently demonstrated for solid state organic semiconductor lasers [30].

In this chapter, we present low order liquid core DFB microfluidic dye lasers with reduced lasing threshold. Our strategy to lower the pump threshold was based on reducing the out-of-plane diffraction losses by employing low order diffraction gratings and increasing the pumping efficiency by a longitudinal pumping geometry. The threshold gain g_{th} for a DFB laser can be expressed as:

$$g_{th} = a + a_m \tag{1}$$

Where a is the propagation loss coefficient in the cavity due to optical scattering, absorption and out of plane diffraction; a_m is the loss coefficient due to the finite reflection from the grating, also referred to as mirror loss coefficient [31]. By decreasing the grating order, both propagation loss a and mirror loss a_m can be decreased due to the reduced out-of-plane diffraction and enhanced in-plane coupling respectively. By overcoming the previous technical limitation [29], we developed a two-step replica molding process that allowed fabricating low order DFB structures with periods down to 200 nm. In addition, the relationship between the gain at threshold g_{th} and the pump power at threshold P_{th} can be determined by solving the exciton density rate equations [32]:

$$g_{th} = \frac{2\,\kappa\,\eta_a\,P_{th}}{V\,h\nu} \tag{2}$$

Where κ is the product of the confinement factor, singlet exciton lifetime, photoluminescence quantum yield and stimulated emission cross-section; η_a is the absorption efficiency of the pump light; V is the cavity volume and $h\nu$ is the pump photon energy. For certain cavity and gain medium the κ and V are set; hence the pump threshold can be reduced by increasing the absorption efficiency of the pump light η_a. In order to address the low absorption efficiency in the transverse pumping geometry, a more efficient pumping configuration was implemented in this work by using longitudinal pumping to further reduce the pump threshold.

As shown in Fig.2.1 (a), the laser chip was entirely made of PDMS which is widely used for fabricating microfluidic chips and lab-on-a-chip systems. It consisted of two monolithic layers: the top one had a microfluidic channel acting as the waveguide structure (Fig. 2.1 (b)); while the bottom one had an array of nano grooves acting as the DFB grating (Fig. 2.1 (c)). After aligning and bonding them together (Fig.2.1 (c)), the microfluidic channel was then filled with a

Rhodamine 6G solution (1 mg/ml) with a slightly higher refractive index than that of PDMS (n_{pdms}=1.4123). Thus a liquid core / PDMS cladding waveguide can be formed inside the chip, while the optical feedback was provided by the DBF gratings on the bottom side of the channel. The dye solvent had a refractive index of 1.4140 produced by mixing water and dimethylsulfoxide (DMSO) at a ratio of 55:45. The waveguide had cross-sectional dimension of 4 μm × 4 μm supporting a single TEM mode in the spectral region of the dye gain. All the gratings were 5 mm long, while the 1st, 2nd and 3rd order DFB gratings had periods of 204, 408 and 612 nm respectively.

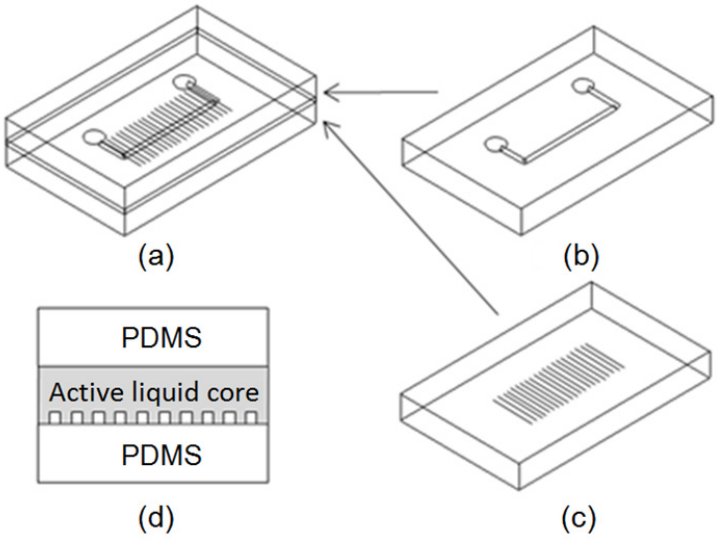

Figure 2.1: (a) - (c). The fabrication steps followed to construct the DFB dye laser. (d) Schematic cross-section view of an optofluidic DFB dye laser.

The laser chip was fabricated in two steps. The top and bottom PDMS layers were prepared by standard replica molding method respectively (Fig. 2.1 (b) and (c)). The master mold for microfluidic channel was defined using standard UV lithography on a 4 μm thick SU-8 film (GM-1040, Gersteltec Inc., spin speed of 800 rpm) on a silicon wafer. While the master grating mold was defined by electron beam lithography (Vistec EBPG5000, 100kV acceleration voltage).

The electron-beam resist was a 100 nm thick hydrogen silsesquioxane (HSQ) film (FOX-12, Dow Corning, spin speed of 5000 rpm, dose of 800 μCb/cm^2) coated on a silicon wafer. HSQ was chosen for its high resolution and being a negative photoresist allowed its direct usage as a mold.

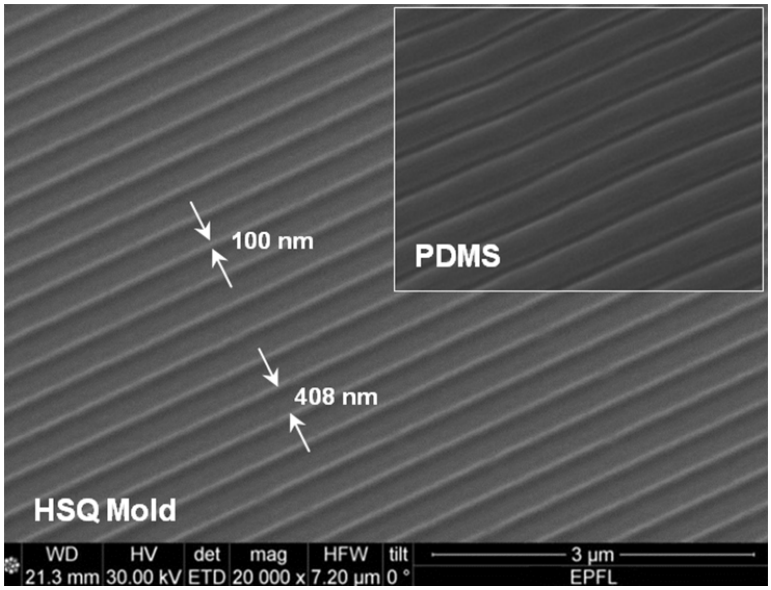

Figure 2.2: Scanning electron microscopy images of the second order grating in HSQ, the corresponding PDMS replica (coated with10nm gold) image is also shown in the inset picture.

The SEM picture of 2nd order grating structure with a period of 408 nm is shown in Fig. 2.2, each line had an approximate width of 100 nm. Subsequent to treating with Trimethylchlorosilane vapor, the pattern of the structured SU-8 and HSQ films were transferred into two PDMS slabs (Dow Corning Sylgard 184) by replica molding (Fig. 2.1(b) and (c)). After oxygen plasma treatment (25 W, 10 seconds), the two PDMS slabs were immediately aligned under a microscope and brought in contact to permanently bond (Fig. 2.1(a)). Subsequent to bonding, the PDMS chip was cut into appropriate size and its side facets were planarized by a final molding step using a flat wafer.

As shown in Fig.2.3 of the experimental setup, a longitudinal pumping method was implemented to improve the pumping efficiency. The laser beam from the Q-switched Nd: YAG

laser (wavelength of 532 nm, pulse duration of 4.5 ns, and repetition rate of 100 Hz) was focused through a 5× magnification objective lens (numerical aperture of 0.1), thus forming a low divergence beam near the focus point (beam waist radius of 20μm, divergence of 50mrad).

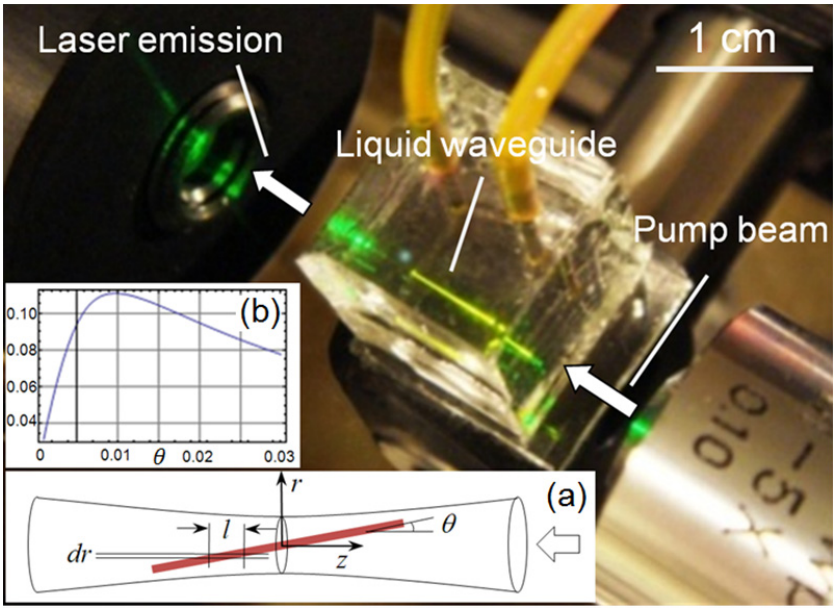

Figure 2.3: The picture of experiment setup for longitudinal pumping. Insets (a) illustrate the longitudinal pumping geometry and (b) the calculated dependence of the absorption efficiency as a function of the angle.

As shown in the inset Fig.2.3 (a), to get maximum pump efficiency, the waveguide needs to be at a small tilt angle θ relative to the pump beam axis. The absorbed power P can be expressed as:

$$P = \int_{-\frac{a}{2}-L\sin\theta}^{\frac{a}{2}+L\sin\theta} I(z,r)(1-e^{-\beta l})\, a \cdot \mathrm{d}r \tag{3}$$

Where $\mathrm{I(z,r)}$ is the intensity distribution of Gaussian beam and $\mathrm{z = r/\tan\theta}$; L is the waveguide length; a denotes both the waveguide width and thickness; l is the effective absorption length ($\mathrm{l = a/\sin\theta}$) and β is the absorption coefficient. Therefore the absorption efficiency η_a can be

written as $\eta_a = P/P_0$; P_0 is the total power of the input Gaussian beam. As shown in inset graph Fig.2.3 (b), the simulation result gives an optimized η = 11 % when θ = 0.01rad. For the transverse (top) pumping scheme in previous works [9-10], the absorption length of the pump light was mainly limited by the waveguide thickness of several micrometers which is far less than the typical extinction length in dye solutions. Based on the same waveguide, the absorption efficiency is calculated to be 1.6 % for transverse pumping (with cylindrical lens $f = 5$ mm). So an enhancement factor of 7 in the absorption efficiency can be realized in the longitudinal pumping scheme.

The laser emission was collected from the side and delivered to a fiber coupled CCD spectrometer with 1.2 Å resolutions (Ocean Optics HR4000). A typical single mode lasing spectrum above threshold from the 2nd order DFB dye laser is shown in Fig. 2.4(a). The laser mode appears at the wavelength of 569.1 nm. The wavelength is approximately 1.5 % lower than calculations due to the PDMS shrinkage after solidification. The laser had a linewidth of less than 0.2 nm. Fig. 2.4(b) shows the input-output relationship of this laser. The threshold pump energy was measured to be 78 nJ/pulse. As shown in Fig. 2.4(c), the edge emitting laser beam pattern was also characterized by a CCD (charge-coupled device) camera. The divergence of the laser beam was measured to be about 12 degrees. The good quality of the lasing beam is attributed to the symmetric cross-section of liquid waveguide cavity. The dye laser output energy was measured with a power meter and a fluorescence filter. According to the output energy from one end, the energy efficiency of the 2nd order dye laser is calculated to be 2% at 300 nJ/pulse pump energy.

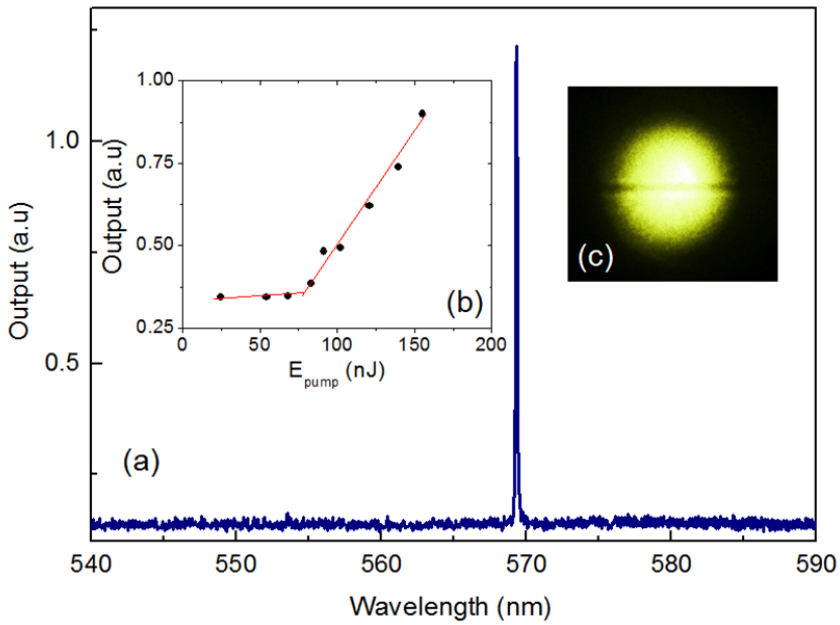

Figure 2.4: (a). The typical laser emission spectrum above threshold from second order DFB optofluidic dye laser. (b) The plot of output energy versus the pumping energy which indicates a threshold of 78 nJ/pulse. (c) The intensity pattern of the edge emitting laser beam from second order DFB dye laser.

To investigate the effect of the grating order on the threshold pump energy, three groups of devices corresponding to 1st, 2nd and 3rd order diffraction grating were fabricated and tested. The results are plotted in Fig.2.5. In contrast to the expected behavior, the 2nd order DFB microfluidic dye laser was found to exhibit the lowest average pump threshold of 90 nJ/pulse, lower even than the 1st order of 133 nJ/pulse. This is attributed to the fabrication limitation of replica molding with soft PDMS. Due to its low modulus and high viscosity, the commercial PDMS used for this experiment is unsuitable for replication of patterns below 250 nm [33]. Particularly, for the high density nano-scale relief structure of the master, such as our 1st order gratings, the surface tension of PDMS inhibits its filling into the nano gap, in analogy to the hydrophobic effect [34]; hence the grating depth of the 1st order on PDMS is lower than that of 2nd order thus resulting in weaker coupling in the 1st order. Also as shown in Fig.2.5, the 3rd order

DFB laser has much higher average pump threshold of 157 nJ/pulse than 2nd one. This is mainly attributed to the lower coupling coefficients and higher out of plane diffraction losses of the 3rd order gratings than 2nd order one at the same conditions of grating depth and waveguide configuration [32].

Compared to the previous 15th order DFB dye lasers [29], the 2nd order DFB microfluidic dye laser presented in this work exhibits about 40 times lower pump threshold energy. Beside the reduction of the out of plane diffraction loss from 15th to 2nd order grating, the more efficient pumping scheme is another main factor for reducing the pump threshold. Thanks to the liquid core waveguide embedded in a transparent PDMS chip, longitudinal pumping can be effectively implemented; thus the interaction length between the pumping beam and waveguide is much longer than the value of waveguide thickness in the previous work.

In summary, a two steps replica molding process was developed to effectively combine UV and electron-beam lithography for realizing liquid DFB waveguide in a PDMS chip. By exploiting the longitudinal pumping scheme, the 2nd order DFB optofluidic dye laser exhibited the lowest pump threshold of 78 nJ/pulse, which is significantly lower than previous results [29, 35-36]. As the material and fabrication method implemented in this work are both compatible with microfluidics, this dye laser can lead to a low cost, coherent light source for integrated lab-on-a-chip systems. In addition, due to the excellent elastomeric property of PDMS, the lasing wavelength can be continuously tuned by simply stretching or compressing the chip along the waveguide direction [13]. The low pump threshold and compact size of this laser also provide the possibility to integrate multiple DFB dye lasers in an array configuration for multi-wavelength emission. In future work, we will explore the implementation of high quality 1st order gratings in alternative materials, in addition with novel gain media and cavity designs, to further reduce the pump threshold of DFB optofluidic dye lasers.

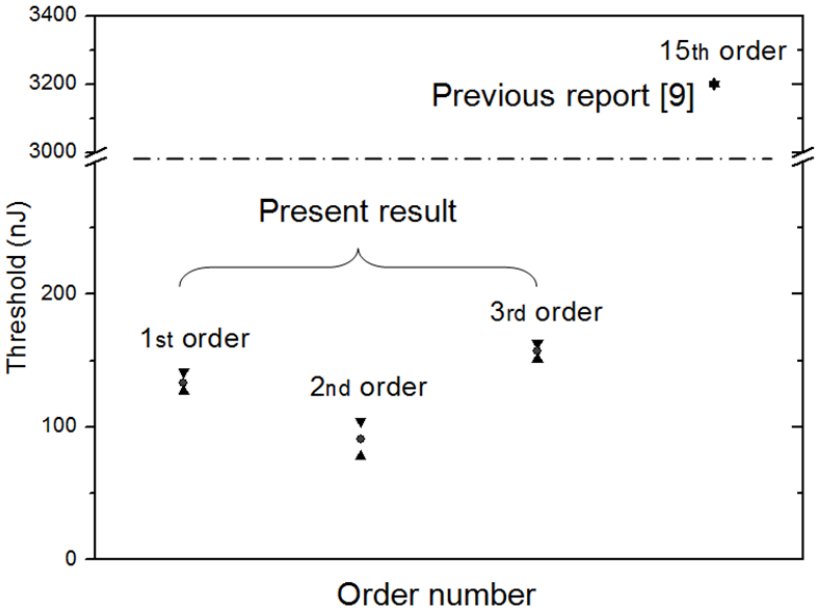

Figure 2.5: The threshold pump energy comparison between different order DFB dye lasers.

Chapter 3

Optofluidic evanescent dye laser

In this chapter, we demonstrate an optofluidic evanescent laser based on a circular distributed feedback grating with the dye solution acting as the cladding layer. The laser Bloch mode is confined within the solid grating and experiences optical gain via the interaction between its evanescent components with the dye solution. Above a pump energy of 9.5 μJ/pulse, the laser exhibited single mode operation at 571.09 nm. Stable narrow-linewidth emission was observed for a wide range of fluid refractive indices, even for those lower than of PDMS. We attribute this property to the separation of the propagating mode with the fluidic gain.

To this end, various cavity configurations have been demonstrated [24-26]. And in the previous chapter, we have demonstrated a high performance optofluidic single mode dye laser based on liquid core waveguide [5]. Optofluidic dye lasers are particularly attractive for spectroscopic applications due to the wide choice of emission wavelengths and the possibility of avoiding photobleaching by flowing the gain medium. In all these previous devices, the guided mode is confined inside the fluid gain medium and thus the refractive index of the solution determines the emission wavelength. Although this enables the tuning of the lasing wavelength by fluidic mixing, in practice stable and single mode operation require high control of the refractive index of the fluid and moderate flow rates across the waveguides.

To overcome this, evanescent field dye lasers have been proposed in the past [37-38] . In these, the liquid gain medium surrounds a solid waveguide and is optically excited. The excited chromophore in the near-field of the waveguide is evanescently coupled with the laser mode, thus providing optical gain. To date, several evanescent gain optofluidic dye lasers have been demonstrated, based mostly on whispering gallery mode resonators, such as the infilled silica capillary tubes, or the fibers embedded in dye solutions [26, 39-40] . These structures are usually characterized to exhibit multimode. More recently, evanescent lasers operating in the telecommunication wavelength range have found applications in the field of silicon photonics [41] .

In this chapter, we demonstrate an optofluidic evanescent dye laser, exhibiting single mode operation. It comprises of a solid second order circular DFB grating and a PDMS chamber filled with dye solution. The thin layer of the solution serves as the cladding and covers the entire surface of the solid DFB cavity. Due to the high waveguide mode confinement in the solid core, the mode selection and lasing wavelength are primarily determined by the properties of the solid DFB cavity. In comparison to liquid core dye lasers [13], stable and single mode operation can be achieved for a wide range of refractive indices of the dye solution.

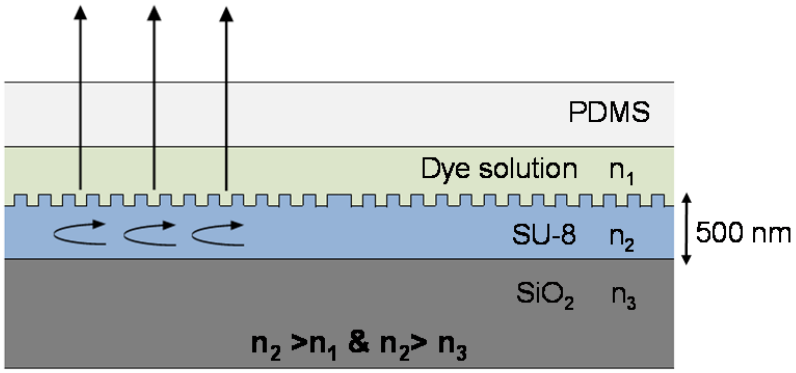

Figure 3.1: The schematic cross section of the dye laser chip.

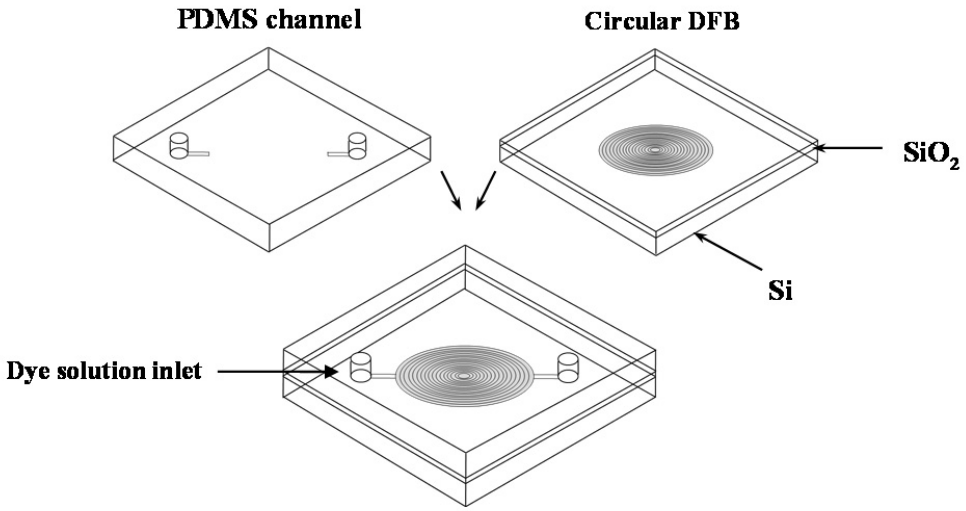

Figure 3.2: The fabrication process of the evanescent dye optofluidic laser.

In Fig. 3.1, a cross-sectional schematic of the circular DFB resonator is illustrated. It is made of the negative photoresist SU-8 (refractive index n_{SU8} = 1.59) patterned on top of silicon dioxide layer (n_{SiO2} = 1.46) on a silicon substrate. The PDMS (polydimethylsiloxane) (n_{PDMS} = 1.4128) forms a microfluidic chamber which envelops the entire surface of the solid DFB cavity. By infilling the dye solution into the PDMS chamber, a thin layer of liquid gain medium is formed on top of the grating serving as the upper cladding of the cavity. In comparison to a linear

grating, the circular DFB cavity has a large surface area and enables enhanced interaction area of the evanescent tail with the gain medium. The second order DFB grating provides both optical feedback and output coupling via second and first order diffraction respectively, thus forming a surface emitting optofluidic laser.

The fabrication process is illustrated in Fig.3.2. The grating was realized by electron beam lithography (Vistec EBPG5000, 100kV). The electron beam resist was a 500 nm thick film of the negative photoresist SU-8 (GM-1030, Gersteltec Inc., 8 μCb/cm^2) on a 5 μm wet oxide layer on a silicon wafer. SU-8 was selected for its optical transparency in the visible spectrum and its high sensitivity to the electron beam, thus allowing rapid patterning of large structures. The grating period was 370 nm in order to satisfy the second order Bragg condition $\Lambda = \lambda/n_{eff}$, where n_{eff} denotes the effective refractive index of the waveguide mode and λ is the emission wavelength. A scanning electron microscopy (SEM) image of the grating at a tilt angle of 30° is shown in Fig.3.3. The width of the grating grooves was approximately 130 nm. The PDMS structure for the microfluidic channel was prepared by replica molding. The master mold for the microfluidic channels was defined using UV lithography on a 4 μm thick SU-8 film (GM-1040, Gersteltec Inc.) on a silicon wafer. After oxygen plasma treatment (15 W, 20 seconds), the PDMS layer and the substrate with the circular grating were aligned under a microscope and brought in contact to permanently bond. As shown in Fig. 3.2, the PDMS layer had no structure in the area corresponding to the grating cavity, except for the two channels that enable fluidic connection. The dye solution could flow and fill the clearance between the grating and PDMS layer because of the elasticity of PDMS and the absence of bonding between PDMS and SU-8. In this way, the circular grating was covered entirely with a very thin fluidic layer. This microfluidic configuration was implemented to minimize the dye solution volume and thus the fluorescence which hinders the detection of stimulated emission. It still provide adequate for the evanescent dye laser operation due the near-field nature and thus very short penetration depth of the evanescent waves into the fluid. A Rhodamine 6G solution was used at a concentration of 1

mg/ml. The solvent was prepared by mixing water and dimethylsulfoxide (DMSO) at a ratio of 54:46 and had a refractive index of 1.401 lower than that of SU-8.

The optofluidic evanescent dye laser chip was optically pumped with a Q-switched Nd: YAG laser (532 nm, 4.5 ns pulses and repetition rate of 100 Hz). The experimental set-up is shown in the inset of Fig. 3.4(a). The pump laser beam was focused through a 10× magnification objective lens, reflected by a dichroic mirror (Chroma Inc.) in front of the chip and focused on the laser cavity. The laser emission was normal to the cavity surface. After passing through the same dichroic mirror, it was collected by a fiber coupled CCD spectrometer (Ocean Optics HR4000, 1.2 Å resolution). A typical single mode laser spectrum above threshold is shown in Fig. 3.4. The lasing mode appeared at the wavelength 571.09 nm and had a linewidth of less than 0.2 nm. A plot of the laser output energy versus the pump energy is shown in Fig.3.4(a), from which the threshold pump energy was estimated to be 9.5 μJ/pulse. This value is higher than previous reports on optofluidic lasers [5, 26, 29, 35, 42-43]. We attribute this to the reduced absorption length of the pump light and the small overlap of the laser mode with the gain medium.

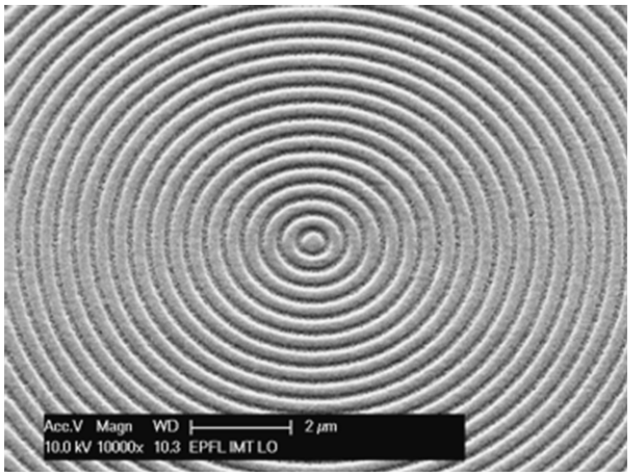

Figure 3.3: The SEM picture of the circular grating at tilt angle of 30°.

From the emission wavelength λ and the grating period, we deduced the waveguide effective index to be n_{eff} = 1.546. Based on a 1-D slab waveguide model, the refractive index of

SU-8 was calculated to be n_{core} = 1.585 . In addition, the emission spectrum was found to be stable both in intensity and wavelength. There was no detectable spectral shift of the lasing wavelength during the experiment even when there was rapid dye flow through the cavity. The fluctuation of output intensity was also below 10%, comparable to the fluctuation of the pump laser.

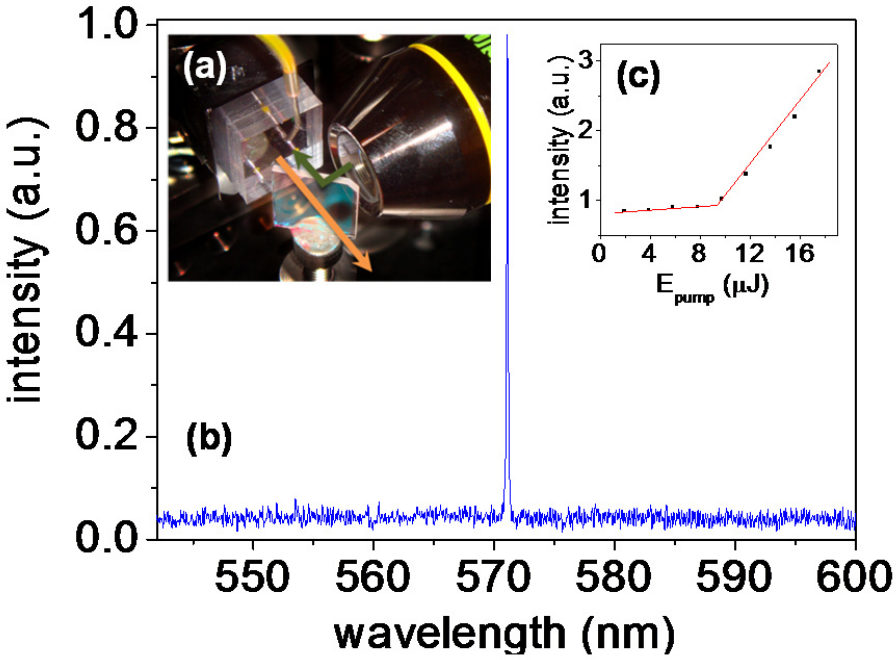

Figure 3.4: (a) The close-view of experimental set-up. (b) A typical laser emission spectrum above threshold and the input-output relationship (c).

Due to the high index contrast between the fluid cladding and the solid core, this dye laser maintained single mode operation over a wide range of the dye solution's refractive index. To explore the effect of the fluid refractive index on the emission wavelength, dye solutions of different refractive indices were employed on the same laser chip (Λ = 370 nm). The dependence of the emission wavelength as a function of the liquid's refractive index is plotted in Fig. 3.5(a). The square dots represent the experimental results and the line indicates the simulation result

based on a 1-D slab waveguide calculation. The fit between the experiment data and the simulation further confirm that the laser mode is confined within the solid waveguide.

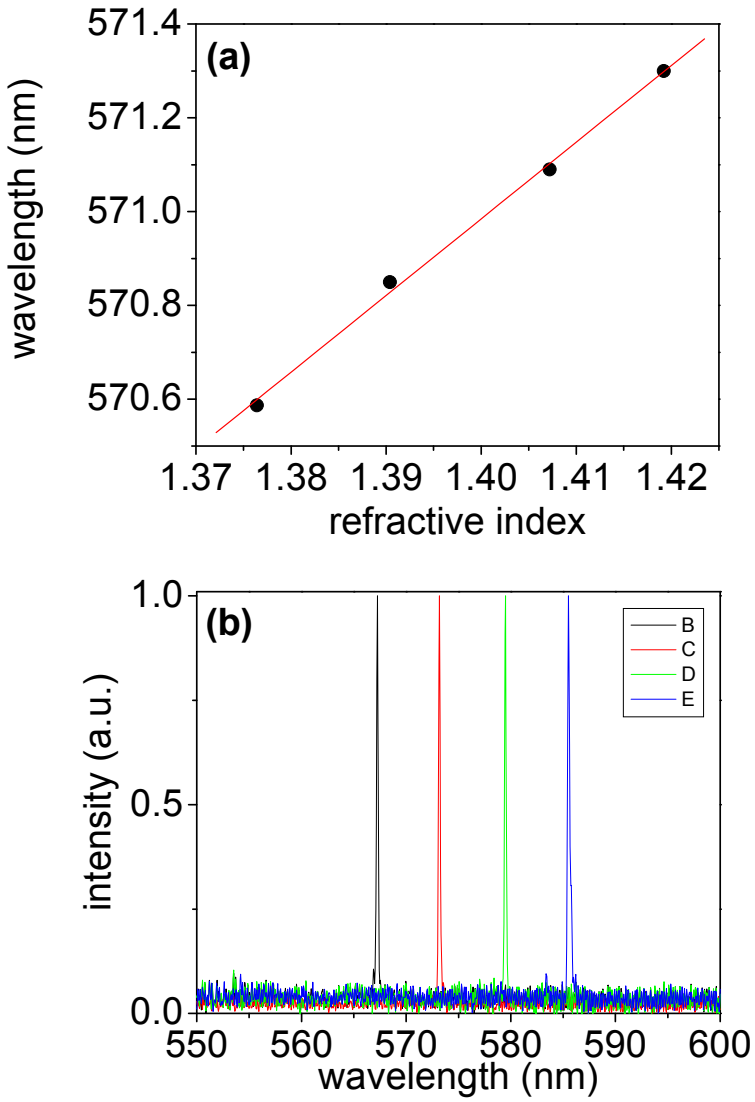

Figure 3.5: (a) The lasing wavelength versus refractive index of dye solution; the square dots represent the experimental data and the line indicates the simulation result. (b) The emission spectra of evanescent optofluidic dye laser of different grating periods.

We did not observe laser emission from dye solutions with refractive indices below n = 1.35, although waveguide modes are supported for these indices. This is attributed to the high

concentration of water in the solution, which has been shown to degrade the gain properties of Rhodamine 6G [44] . In addition, we investigated the tuning of the emission wavelength by changing the period of the circular DFB grating. The emission spectra are plotted in Fig. 3.5(b), denoting a tuning range between 567 nm to 586 nm.

In summary, we demonstrated an optofluidic evanescent dye laser based on a solid circular DFB grating. Under optical excitation, gain was provided by the interaction of the evanescent tail of the waveguide mode with the liquid cladding. The integration of a strongly wavelength selective periodic structure enabled single mode operation. Due to the evanescent coupling between the laser mode and the fluid, single mode operation was maintained for a wide range of refractive indices of the fluid. This laser was realized by constructing an optofluidic circuit on a silicon treated wafer. Further integration of strongly absorbing Si structures or metal electrodes can be implemented for electrical modulation or excitation, since in such evanescent wave coupled gain lasers these integration steps would induce minimal modal perturbation [39, 41, 45]. In future work, we should investigate ways to reduce the lasing threshold by modifying the pumping geometry and employing first order gratings, which we have shown in the past to reduce the lasing threshold.

Chapter 4

Pneumatically tunable optofluidic dye laser

In this chapter, we present a tunable optofluidic dye laser with integrated elastomeric air-gap etalon controlled by air pressure. The chip was fabricated with polydimethylsiloxane (PDMS) via replica molding. It comprises a liquid waveguide and micro-scale air-gap mirrors providing the feedback. The lasing wavelength is chosen by the interference between two parallel PDMS-air interfaces inside the internal tunable air-gap etalon, of which pneumatic tuning can be realized by inflating the air-gap etalon with compressed air. This dye laser exhibits a pumping threshold of 1.6 μJ/pulse, a lasing line-width of 3 nm and a tuning range of 14 nm.

Various types of resonators for microfluidic dye lasers have been demonstrated, a common method for tuning the wavelength of such microfluidic dye lasers is based on varying the refractive indices of dye solutions [42, 46]. Although this method is simple, it has several shortcomings. Firstly, the tuning range is very limited, especially for liquid core DFB dye lasers [5, 46], since the refractive index distribution must also satisfy the single mode condition of the waveguide. As a result, the refractive index of the dye solution can only change in a very small range. Secondly, due to the small transverse dimension of the liquid waveguide, the flow inside the microfluidic channel is very slow, hence the waveguide tuning timing is long. Another tuning mechanism for optofluidic DFB dye laser was reported by Li et al [13]. It is based on mechanical stretching or compressing a laser chip made of soft material (Polydimethylsiloxane (PDMS)), hence changing the period of the DFB grating to tune the lasing wavelength. However, the induced overall deformation of the chip would be at odds with the integration of such dye laser into more complex microfluidic system.

In this chapter, we present an optofluidic laser cavity structure in which the lasing wavelength is chosen by an integrated pneumatic tuning air-gap etalon. As the etalon is made of PDMS which is a kind of elastomer, the air-gap etalon can be inflated by compressed air and the lasing wavelength can be controlled by the air pressure. Compared with previous tuning method [13, 29, 42], this implementation is simpler and the dye laser wavelength can be remotely controlled. Fast laser tuning and a large tuning range can be realized. Meanwhile, since the deformation is localized in the etalon, the tuning process does not interfere with the other components on the chip.

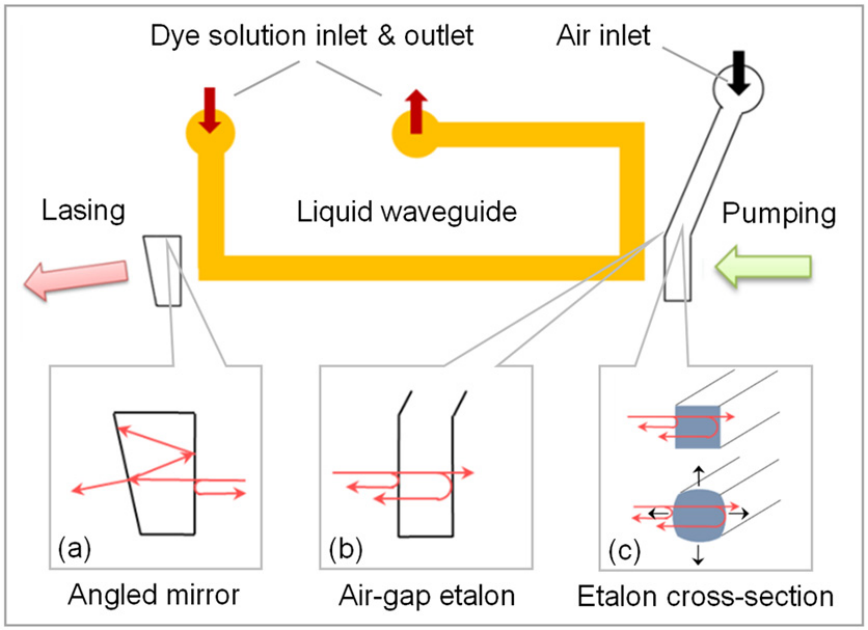

Figure 4.1: The schematic of the dye laser cavity structure.

The schematic of the laser cavity structure is illustrated in Fig.4.1. The whole chip is made of PDMS. It is composed of a liquid core waveguide, at the ends of which two micro-scale air chamber structures are integrated acting as the mirrors providing feedback. The beam reflections occur at the PDMS/air interfaces due the refractive index contrast. As shown in Fig. 4.1(a), the shape of the air chamber located on the left, was specially designed. Only the interface closer to the liquid waveguide is effective for the cavity as the reflected beam can couple back to the waveguide. The other interface has a tilted mirror, from which the reflected beam does not couple back to the waveguide. As a result, the air-gap mirror on the left acts as a simple end mirror for the laser cavity. On the other hand, the air chamber on the right of the waveguide, as shown in Fig.4.1(b), has two parallel PDMS/air interfaces that are both perpendicular to the waveguide. Owning to interference of the reflected beams between the two interfaces, this air chamber behaves as a low finesse air-gap Fabry-Perot (F-P) etalon. This cavity determines the lasing wavelength. Since the PDMS is elastic, the size of the air-gap can be tuned by varying the

gas pressure [47]. As shown in the schematic cross-sectional view of Fig. 4.1(c) of the devices, inflation of the "micro-airbag" with compressed air causes the effective air-gap to increase.

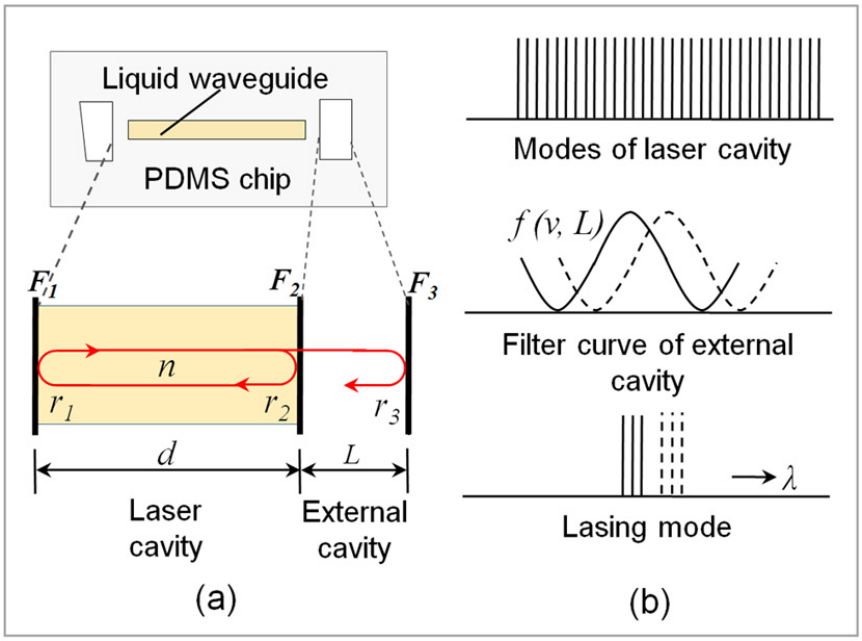

Figure 4.2: The schematic of the laser model based on F-P cavity laser with external mirror.

To further illustrate the working principle of this laser, a model of F-P cavity laser with external mirror is presented in Fig. 4.2 [48-49]. F_1, F_2 and F_3 denote the two facets of the F-P laser and the external mirror, r_1 and r_2 are the real values representing the amplitude reflectance of F_1 and F_2, respectively, while r_3 denotes the effective amplitude reflectance of the external mirror F_3. n is the effective refractive index of the lasing cavity. The length of the lasing cavity and the external cavity are d and L respectively. Due to the existence of the external mirror F_3, the effective reflectance r_{2eff} of the mirror F_2 is given by [49]:

$$r_{2eff} = r_2 - \frac{1-r_2^2}{r_2}\sum_{k=1}^{\infty}\left[r_2 r_3 \exp\left(-\frac{j4\pi L}{\lambda}\right)\right]^k \tag{4}$$

where λ is the wavelength in vacuum. Assuming the divergence of the beam reflected from mirror F_3 can be negligible, , $r = r_1 = r_2 = r_3 \approx 0.03$ using the refractive index of PDMS $n_{PDMS} = 1.412$. Due to the weak reflection coefficient, higher orders can be negligible. ($r^2 = 0.0009 << 1$), r_{2eff} can be expressed as:

$$r_{2eff} = R_2 \exp(j\phi_L) \tag{5}$$

$$R_2 = r\sqrt{2\left(1-\cos\left(\frac{4\pi L}{\lambda}\right)\right)} \tag{6}$$

$$\phi_L = -\arcsin\left[\sin\left(\frac{4\pi L}{\lambda}\right)/R_2\right] \tag{7}$$

where R_2 and ϕ_L represent the amplitude and phase of r_{2eff}.To obtain lasing, the following amplitude and phase condition must be simultaneity satisfied:

$$r_1 R_2 \exp[(g-\gamma)d] = r^2 \exp[(g-\gamma)d]\sqrt{2\left(1-\cos\left(\frac{4\pi L}{\lambda}\right)\right)} = 1 \tag{8}$$

$$\phi_L + \frac{4\pi nd}{\lambda} = 2\pi m \qquad \text{(m=integer)} \tag{9}$$

where g and γ represent the gain and loss of the cavity respectively. The influence of the external cavity can be observed from equations (8) and (9). In the absence of the external cavity ($R_2 = r$ and $\phi_L = 0$), the F-P laser oscillation is fully determined by its gain profile and longitude modes. The presence of the external cavity alters both the gain condition and the longitudinal mode wavelength positions. However, as $\phi_L << 2\pi m$, the mode positions of the laser cavity are almost as same as without external cavity. Therefore the external cavity mainly impacts the gain condition (Eq. (8)) which is equivalent to adding a tunable etalon inside the laser cavity. As illustrated in Fig.4.2(b), the laser cavity modes are selected by the center wavelength of the filtering curve formed by the reflectance spectrum of the air-gap etalon.

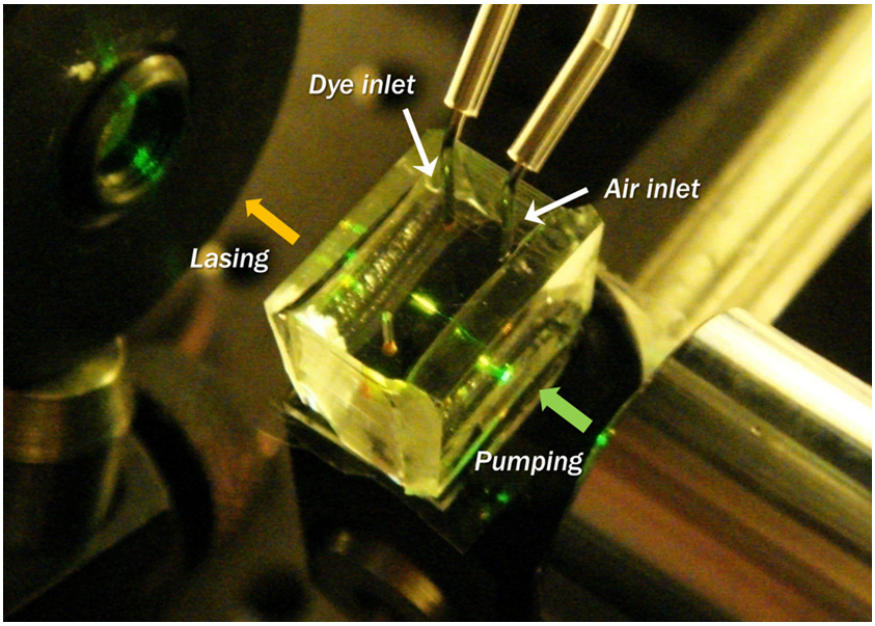

Figure 4.3: The picture of dye laser chip under testing.

The top PDMS layer of the chip was prepared by replica molding method. The master mold was defined using UV lithography on a 4 µm thick SU-8 film on silicon wafer. The length of the waveguide is 800 µm and the width 4 µm. The air chamber on the right acting as the external cavity has a gap width of 12 µm. The structured PDMS slab (Dow Corning Sylgard 184) was then bonded with a flat PDMS layer. A mixture of two different dyes was utilized to improve the tuning range. The chip was filled with a mixed dye solution containing rhodamine 6G and rhodamine B at the concentration of 0.9 and 0.15 mg/ml respectively. The solvent was prepared by mixing water and dimethylsulfoxide and had a refractive index of 1.4140. Fig.4.3 is the picture of a dye laser chip under testing. To improve the pumping efficiency, a longitude pumping scheme was adopted [8]. The air inlet of the chip was connected to a mechanical air pressure regulator (ControlAir Inc, Type 100-BA) providing arbitrary pressure in the range of 2 - 30 psi. The pressure was monitored by a digital pressure gauge (Omega Inc. DPG4000).

A comparison of the emission spectra from the dye laser is shown in Fig.4.4. The black line denotes a typical lasing spectrum above the pumping threshold, and the red shows the

emission spectrum bellow the lasing threshold. The laser emission appears at the wavelength of 588.4 nm with a linewidth of about 3 nm. By calculating the FSR (free spectral range) of the liquid waveguide cavity, this lasing emission was expected to contain about 19 longitudinal laser modes. The plot of pumping pulse energy versus output pulse energy is shown in the inset of Fig. 4.4. The threshold pump energy was measured to be 1.6 μJ/pulse. The dye laser tuning was controlled by air pressure. As shown in the superposition graph of the laser emission spectra in Fig. 4.5, a tuning range of 14 nm was realized which agrees with the estimated free spectral range (FSR) of the etalon. The inset of Fig.4.5 shows the relationship of the lasing wavelength versus air pressure. As limited by FSR of the etalon and also the dye solution's gain profile, the laser tuning shows clear cycle behavior with the air pressure.

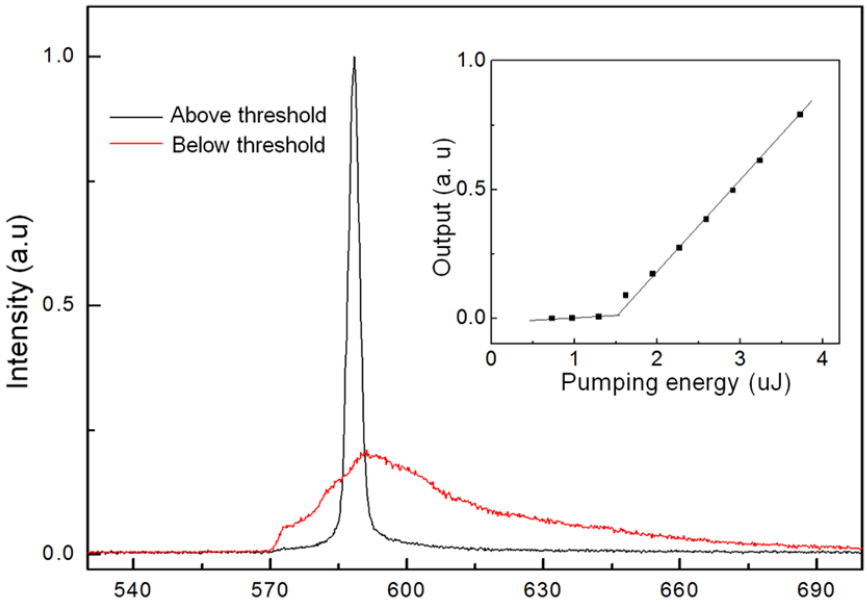

Figure 4.4: The caparison of the emission spectrum below and above lasing threshold. The inset shows the plots of output versus pumping energy.

There are two contributing factors to the wavelength tuning: the geometrical variation of the etalon cavity and the refractive index change of the air inside the cavity. From the calculation, during the increment of air pressure, the cavity length has an increment rate of 33 nm/psi and air

refractive index has an increment rate of 2×10^{-5}/psi, in which the cavity geometric modification can be considered as the primary factor for the wavelength tuning. Due to the low viscosity, the air flow has a much higher circulating rate inside the micro-channels compared to the liquid. Thus such pneumatic tuning can exhibit much faster response time compared to the tuning methods using liquid flow. In addition, thanks to the separate air-gap etalon for selecting the lasing wavelength, this dye laser shows nice wavelength stability compared to the liquid-core waveguide DFB dye laser, in which the variation of refractive index induced by thermal fluctuation can shift the lasing wavelength. In contrast, this dye laser chip showed negligible wavelength variation by locking the pressure with the mechanical air regulator.

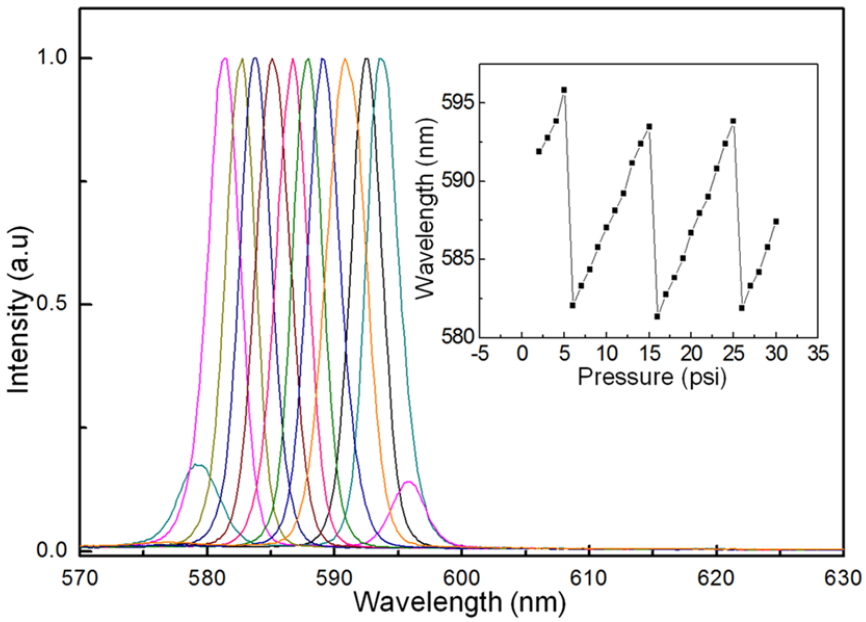

Figure 4.5: The superposition of the lasing spectrum in whole tuning range (enhanced on line). The inset shows the relationship of lasing wavelength versus air pressure.

In conclusion, we demonstrated a pneumatically tunable optofluidic dye laser with integrated elastomeric air-gap etalon. As the fabrication process and control method are

compatible with conventional a PDMS based microfluidic chip [20], the design of this optofluidic dye also promises a practical way for the integration of dye laser source into lab-on-a-chip system.

Chapter 5

Imaging based optofluidic air flow meter

In this chapter, we present an optofluidic chip with integrated polymer interferometers for measuring both the microfluidic air pressure and flow rate. The chip contains a microfluidic circuit and optical cavities on polymer which was defined by soft lithography. The pressure can be read out by imaging the interference pattern of the cavities. The air flow rate was then calculated from the differential pressure across a microfluidic Venturi circuit. Air flow rate measurement in the range of 0-2mg/second was demonstrated. This device provides a simple and versatile way for in situ measuring the micro-scale air pressure and flow on chip.

In the past years optofluidic has attained substantial attention in both microfluidics and optics. With the development of microtechnology, multiple optofluidic devices have been realized by merging the optics and fluidics synergistically [1-2], such as dye lasers [5, 36, 50], tunable photonics crystal [51], optical switches [52] and fluidic lens [53]. In such devices, the optical functional fluids are normally in the liquid form. On the other hand, as another form of the microfluidic, the gas phase microfluidic devices have also attracted much attention [54-56]. For example, the compressed air has become one of the dominated methods to manipulate the liquid analyte for lab-on-a-chip applications, either by pushing the liquid directly or by actuating the membrane valve [20, 57]. However, quite few works have been reported on the optofluidic devices which combine optics with the gas phase microfluidics. Very recently a pneumatically tunable optofluidic dye laser has been reported in which a microchannel based tunable air-gap etalon can be adjusted by air pressure [58]. Since the air pressure has been extensively utilized to manipulate both the liquid and optical elements on a chip, measurement of the air pressure and flow becomes desirable especially for local measurement inside microfluidic chip.

In this work, we demonstrated an optical interferometric air pressure sensor and flow meter based on an air circulating optofluidic chip. Different from the MEMS (Microelectronic and Microelectromechanical Systems) based pressure or flow sensors which required sophisticate fabrication process with silicon [59-60], this optofluidic sensor was defined on a polymer chip with soft lithography and the measurement was done by imaging the interference pattern from the chip. This sensor can be simply fabricated with low cost.

The chip structure is illustrated in Fig.5.1, It consists of a structured Polydimethylsiloxane (PDMS) polymer layer bonded onto a rigid glass substrate. The structure inside the chip can be divided into two parts: the microfluidic channel and two separate optical cavities. The air flows in the main microfluidic channel. While in the channel middle part there exists a slit type Venturi tube for differential pressure based air flow measurement.

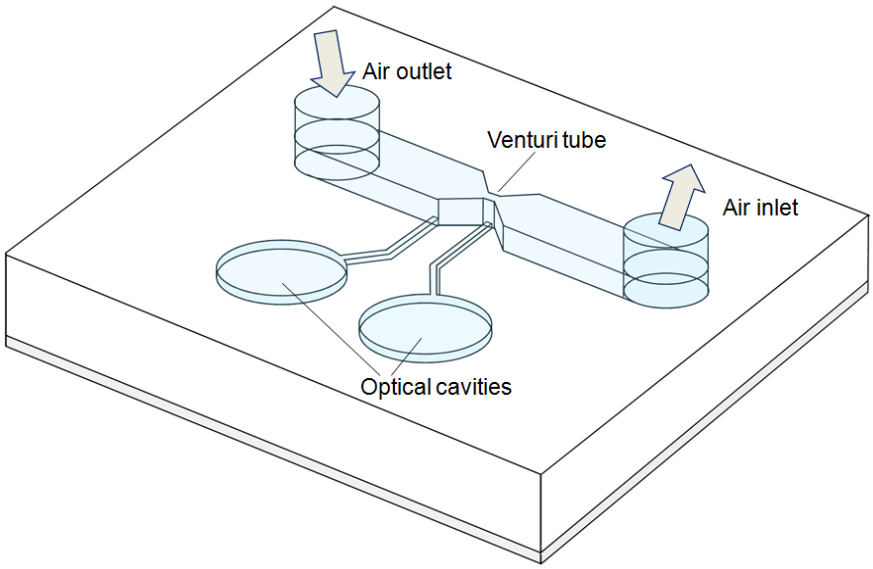

Figure 5.1: The structure of optical chip including the microfluidic channel and optical cavities.

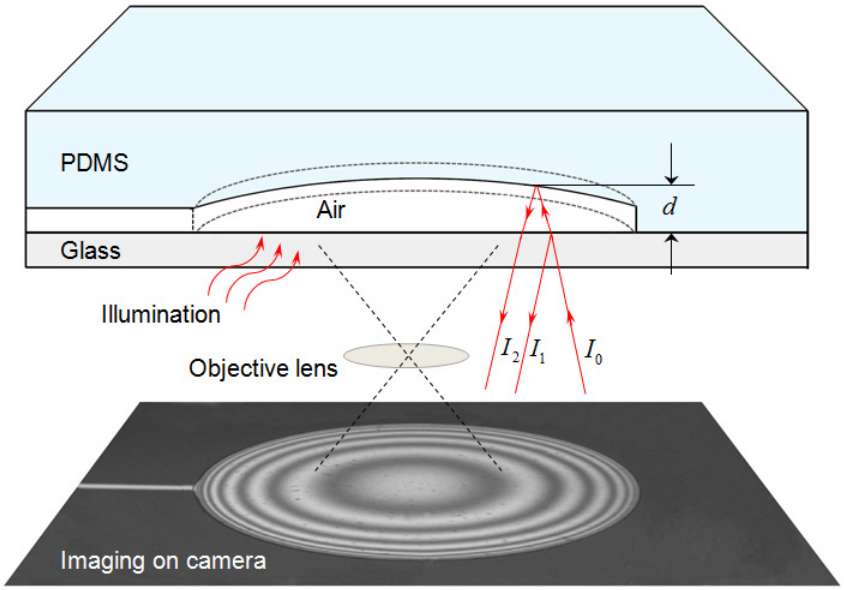

Figure 5.2: The cross-section view and working principle of the optical cavity. Bottom picture shows the corresponding interference image on microscope.

Due to the elasticity of the polymer, the polymer optical cavities can be deformed by the local air pressure. Upon illuminating by monochromatic light, a Newton's ring pattern was formed in the cavities. By imaging and analyzing this interference pattern we can calculate the air pressure and hence the flow rate.

The cross section of the optical cavity for pressure sensing is shown in Fig.5.2. The top PDMS layer has a round chamber structure with flat inner surface. A thin air gap is formed between the PDMS chamber and glass substrate. Thanks to the flexibility of PDMS, after filling the compressed air, the PDMS surface in the cavity was deflected into a curvature shape depending on the pressure value (all pressure here means the relative pressure to the atmosphere). When the cavity is illuminated by a coherent monochromatic light, the reflected light from the two inner surfaces of the cavity can interfere with each other constructively or destructively which depends on the phase delay or gap size. Thus the resulting total reflection intensity can be expressed as:

$$I = I_1 + I_2 + 2\sqrt{I_1 I_2}\cos\left(\frac{4d\pi}{\lambda} + \pi\right) \tag{10}$$

Where I_1 and I_2 are the reflection intensity from the PDMS-air interface and air-glass interface respectively; d is local air gap size; λ is the wavelength of the illumination light. Due to the low reflectivity (< 4%) on these two interfaces, I_1 and I_2 have very close value hence resulting results good contrast of the interference pattern, meanwhile the multiple reflections can be neglected in this model. As the PDMS/air interface will be deformed to a dome shape upon applying air pressure, the cavity generates multiple concentric rings interference fringes which is similar to the Newton's ring pattern.

Fig.5.3 shows the measuring principle of the air flow meter which is based on Venturi effect on a planar microfluidic Venturi tube. The Venturi tube is a section of the channels with a

tapered entrance and a straight throat. As the fluid passes through the throat, the velocity increases. According to the Bernoulli's equation, the pressure drop across the constriction is proportional to the square of the flow rate, thus the air flow rate Q can be expressed in a simplified form as [61]:

$$Q = k\sqrt{\Delta P \cdot \rho_1} \tag{11}$$

where Q means the mass flow rate; is the differential pressure $\Delta P = P_1 - P_2$; ρ_1 is the gas density before the entrance of the Venturi tube; k is a coefficient depending on the structure dimensions, environment temperature and other flow conditions. In this experiment, the temperature was assumed to be constant, so the air mass density ρ_1 before the taper entrance has $\rho_1 \propto P_1$ Thus the air mass flow rate can be also expressed as:

$$Q = k'\sqrt{\Delta P \cdot P_1} \tag{12}$$

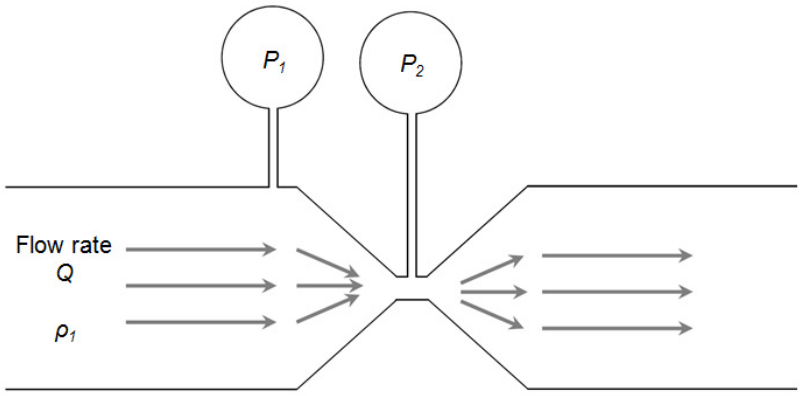

Figure 5.3: The schematic of the Venturi tube for measuring the flow rate.

The structured PDMS layer was fabricated by soft-lithography in one step. It was replicated from a master mold which has double layers of structured negative photoresist SU-8 on silicon wafer. The bottom layer of SU-8 has thickness of 15 um for defining the cavities

structure. The cavity has a 300 µm diameter. After developing the first layer, a second layer of SU-8 was spun on top of it with a thickness of 50 um for defining the microfluidic channel. The main channel has width of 300 µm, and the width of the throat part is 50 µm. The PDMS was prepared by mixing the prepolymer component in 10:1 ratio (base: curing agent, Dow Corning Sylgard 184) and then bake in oven at 80 degrees for 2 hours. Finally the PDMS layer was bonded on the glass substrate using oxygen plasma treatment.

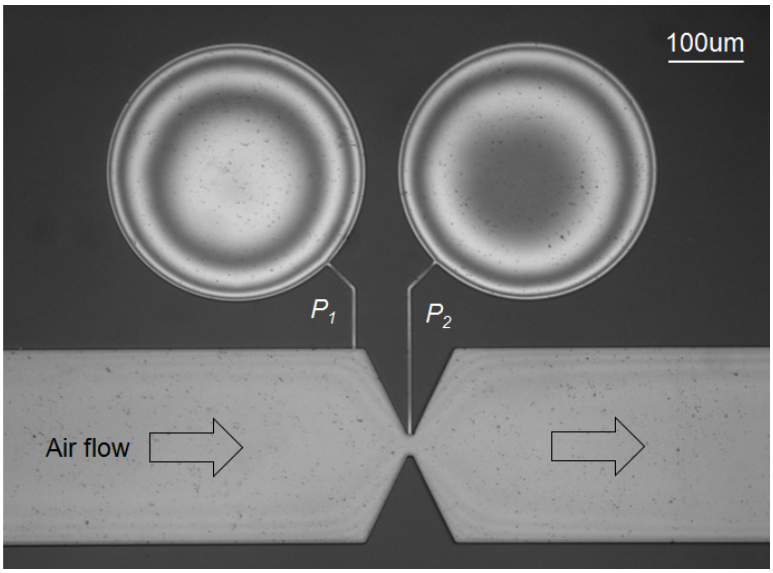

Figure 5.4: An example image of the chip recorded on microscope.

The chip was measured on normal bright field microscope (Infinity Microscope and Mitutoyo M Plan Apo 5x objective) with a built-in beam splitter for illumination. The light source was based on a wideband light source (Dolan-Jenner PL-800 Illuminator) plus a laser line filter (Thorlabs, FL632.8-1) with a transmission linewidth of 1 nm. Instead of using the laser, this monochromatic light source was found to provide sufficient coherence for generating interference pattern and meanwhile almost result none speckle noise. Thus it eliminates the apparatus for cancelling the speckle noise in case of using laser as light source. The image was recorded by a

monocolor CCD camera. The air pressure was generated from a mechanical air pressure regulator (100-AB, Air Control Inc.) and calibrated with a digital pressure gauge (Omega DPG4000). The air flow was controlled by a digital mass flow controlled (Brooks Inc.).

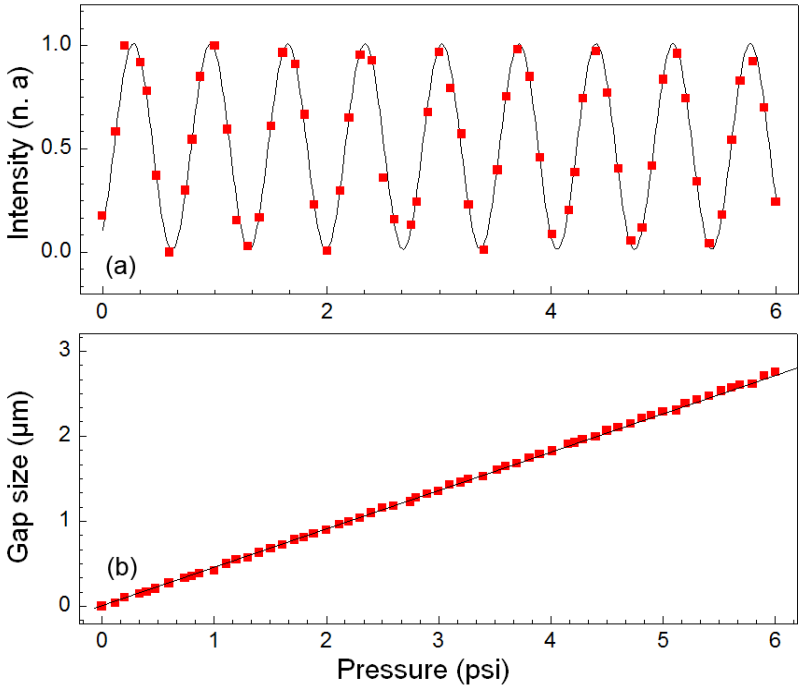

Figure 5.5: The calibration results of the cavity P1. (a) The normalized average intensity at the center of the cavity versus the pressure. (b) The corresponding air gap size at the center versus the pressure.

Fig.5.4 shows an example image of the chip captured on the microscope. The cavities on the left and right correspond to the pressure sensor P_1 and P_2. The interference patterns consist of dark and bright coincident rings which moved out from center to side as the pressure increased. Before the air flow measurement, these two pressure sensors were calibrated with the digital pressure gauge. The Fig.5 5(a) shows the plot of the average intensity of the center in the left cavity P_1 versus applied pressure, as denoted by the red solid squares. The scatter plot reveals a typical sinusoidal relationship which fits very well to a sine curve denoted by the black line.

Based the equation (10), the increment of the air gap in the center can be calculated. The reconstructed result reveals nice linearity in the pressure range 0 - 6 psi as plotted by the air gap increment (red square dots) versus the applied pressure in Fig.5.5(b). The sensitivity was calculated as 1.46 fringes per psi. As the left and right optical cavities are not exactly identical, thus two separate calibrations have been done for them.

The digital mass flow meter was connected to a compress air source providing arbitrary air flow with predefined value. For a same air flow rate, different air pressure at the inlet of the chip was also tested by adjusting the resistance at the chip outlet. The interference images of the two cavities were recorded and analyzed according calibration results shown above. The result is shown in the Fig.5.6 and 5.7. The plot shows the relation of the measured value of $\sqrt{P_1(P_1-P_2)}$ versus the flow rate (mg/second) which can fit the equation (12) very well. Thus the value of the coefficient k' was calculated to be $0.377_{mg \cdot s^{-1} \cdot psi^{-1}}$. At the same flow rate, the values of $\sqrt{P_1(P_1-P_2)}$ (shown as different shapes on graph) give a slight deviation corresponding to different pressure condition at the inlet. Such errors can be due to the inaccuracy of equation (12) or the deformation of the microfluidic channel or more complicated effect. However, this air flow meter still provides satisfied accuracy which is estimated to be below 3% within the range of 0-2 mg/s.

In conclusion, we have demonstrated an optofluidic chip for simultaneously measuring the microfluidic air pressure and the flow rate through imaging. Both of the microfluidic and optical structures were fabricated by soft-lithography on polymer chip in a single step. This optofluidic air flow sensing chip exhibits the advantages of low cost and high sensitivity. As being compatible with the normal microfluidic in terms of both fabrication and characterization [20], this device can be easily integrated into a lab-on-a-chip system for in situ measuring the pressure and flow rate.

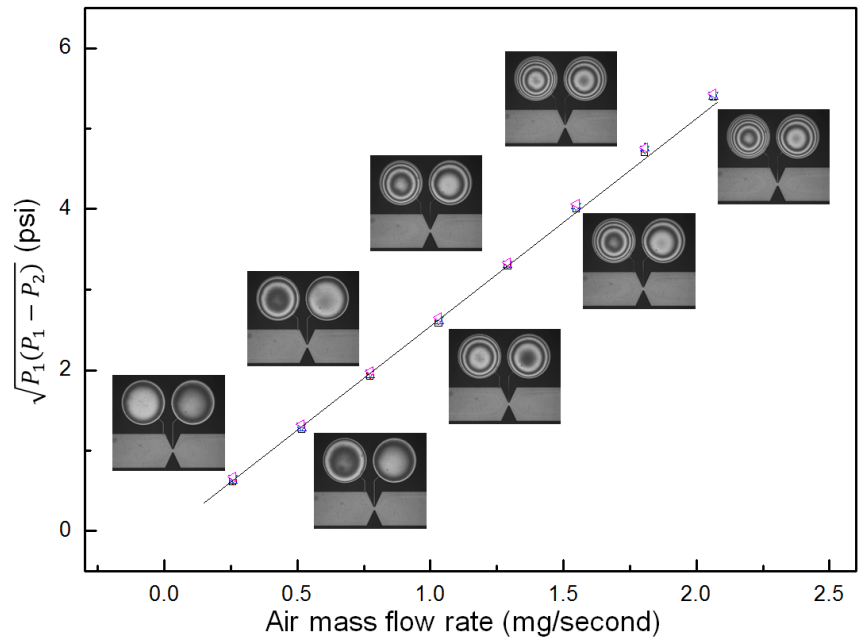

Figure 5.6: The plot of the measured value of $\sqrt{P_1(P_1-P_2)}$ versus air mass flow rate. The inset pictures are the representative images recorded at each flow rates.

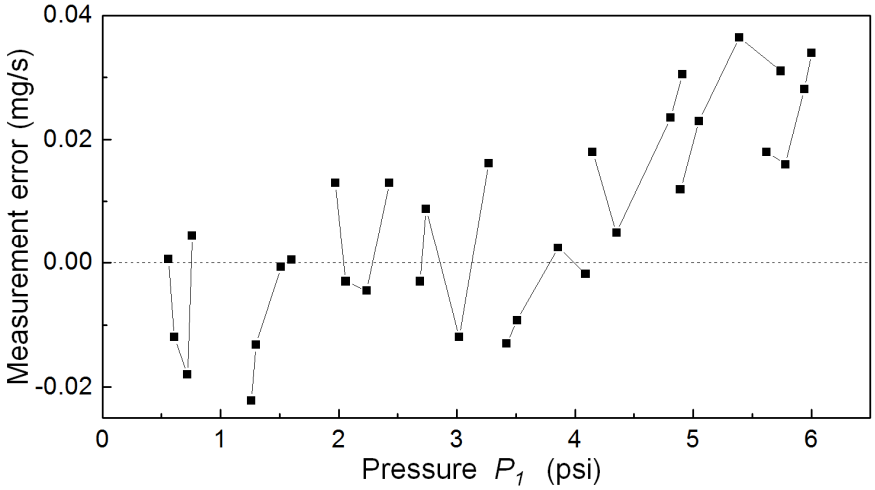

Figure 5.7: The plot of the measured value of $\sqrt{P_1(P_1-P_2)}$ versus air mass flow rate. The inset pictures are the representative images recorded at each flow rates.

Chapter 6

Optofluidic membrane interferometer

In this chapter, we present a chip-scale optofluidic interferometric sensor for measuring liquid pressure based on an imaging method. The chip was constructed with polymer by multilayer soft lithography. It consists of a flexible air-gap optical cavity which upon illumination by monochromatic light generates interference patterns that depend on pressure. The pressure was measured by imaging and analyzing the interference patterns. We also employed a pattern recognition algorithm which significantly simplified the calculation and enhanced the measurement reliability. This pressure sensor was demonstrated with a working range of 0-22 psi and an accuracy of ±1.4% of full scale when temperature stabilized.

Pressure sensors are widely used for controlling and monitoring in thousands of everyday applications, while miniature pressure sensors have made substantial progress since the development of micro-fabrication techniques. Different types of miniature pressure sensors have been developed, such as piezoresistive [62], capacitive [63] and optical [64]. Of particular relevance is the diaphragm-based Fabry-Perot (F-P) interferometric fiber pressure sensor in which a tiny F-P cavity is fabricated at the tip of the fiber, and the pressure can be monitored from the reflected beam intensity [65-66]. However, the sophisticated fabrication process results in high cost for such fiber pressure sensors. Thus a low cost and simply fabricated optical pressure sensor that can be directly integrated into microfluidic circuits would be desirable, especially as demand for single-use device of lab-on-a-chip increases. In recent years, the combination of microfluidics and optics has led to the emerging field of optofluidics [1]. A variety of reconfigurable optofluidic devices have been demonstrated. Optofluidic methods make it possible to build optical components on a chip in the same way as we fabricate microfluidics. In this chapter, we present a novel optofluidic pressure sensor chip which was fabricated by multilayer soft lithography. The fluid pressure is measured by taking an image of the interference pattern formed upon illumination by a monochromatic light source.

Fig.6.1 shows the schematic of the whole pressure sensing apparatus including the optofluidic pressure sensor chip and a camera. During measurement, the pressure force from the fluid causes deformation of the flexible membrane hence the variation of the air-gap thickness. Upon illumination by monochromatic light, the reflected light from the air-gap boundaries interferes with each other constructively or destructively, depending on the air-gap thickness. The resulting total reflection intensity can be expressed as

$$I = I_1 + I_2 + 2\sqrt{I_1 I_2}\cos(\frac{4d\pi}{\lambda} + \pi) \tag{13}$$

where I_1 and I_2 are the reflection intensity from the bottom and top PDMS-air boundaries respectively; d is the air gap distance. Assuming the incident intensity is I_0, due to the low reflectivity on these two boundaries, we have $I_1 \approx I_2 \approx I_0 \times 4\%$. Multiple reflections can be neglected in this case. The fact that $I_1 \approx I_2$ ensures good image contrast of the interference patterns. As the air-gap chamber has a round shape, the PDMS membrane is deformed to a dome shape upon applied pressure. The multiple concentric interference rings are similar to the Newton ring pattern. This interference pattern was captured by the CCD (Charge coupled device) camera through the objective lens.

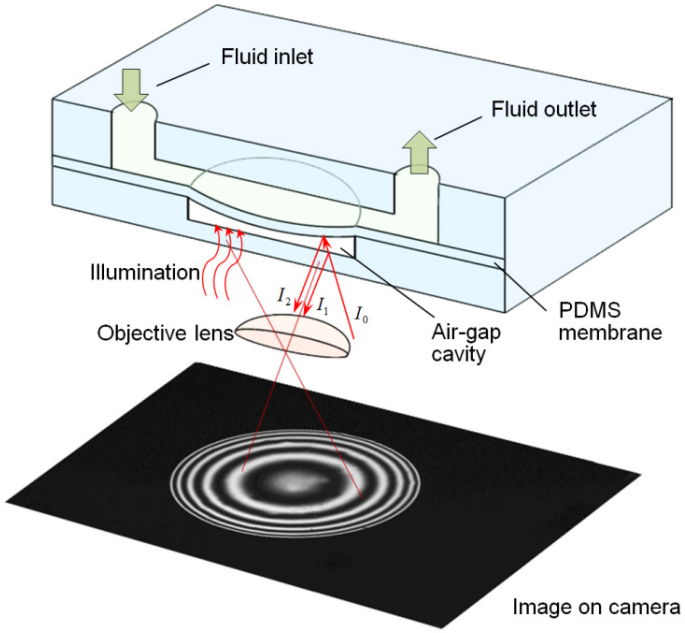

Figure 6.1: The schematic of the pressure sensing apparatus including the chip and an imaging device.

The top and bottom PDMS slab were replicated from two different master molds which are defined by the negative photoresist SU-8 on silicon wafers. The middle PDMS membrane was made by spinning multiple layers of PDMS on a flat silicon wafer. All the characterization in this

work is based on chips with membrane thickness of 537 µm unless otherwise stated. As shown in Fig.6.2(a), the three parts were finally aligned and bonded together using oxygen plasma treatment. Fig.6. 2(b) shows the top view of the chip structure.

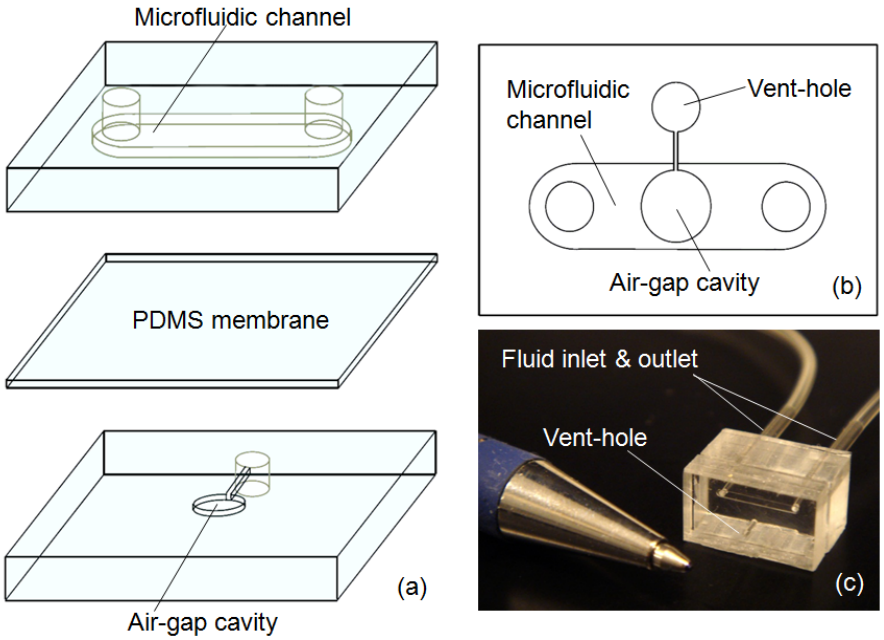

Figure 6.2: (a) The structure of the chip; (b) Top view of the chip structures; (c) Picture of optofluidic chip.

The dimensions of the air-gap cavity are 400 µm diameter and 15 µm thickness. The air-gap cavity connects to the atmosphere through the vent-hole for keeping constant pressure in the air-gap. The microfluidic channel has width of 600 µm and thickness of 50 µm. The picture of the fabricated device is shown in Fig. 6.2(c). The interference patterns from the chip were measured on a bright field microscope with a built-in beam splitter for illumination. We used a diffusive monocolor light source which includes a tungsten light source and a laser line filter (Thorlabs, FL632.8-1) with a transmission linewidth of 1 nm. We found this monochromatic light source has sufficient temporal coherence for generating high quality interference patterns without speckle noise. The pressure was calibrated with a digital pressure gauge. Fig.6.3(a) shows an example

image of the interference pattern captured at pressure of 3.80 psi. The background area outside the air-gap cavity is dark due to the low reflectivity at the PDMS-water interface where the refractive indexes contrast (1.41:1.33) is much lower than that of PDMS-air (1.41:1).

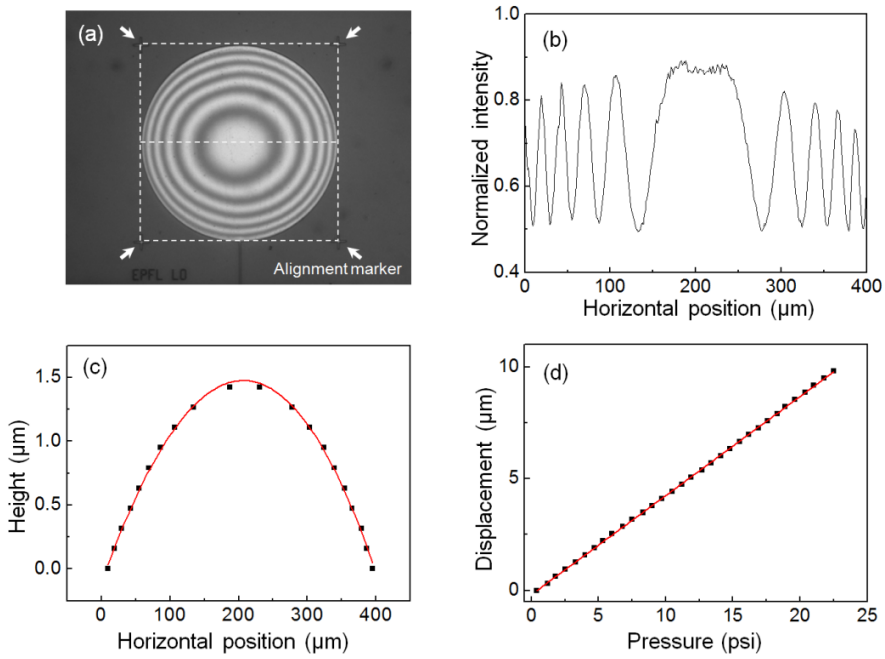

Figure 6.3: (a) An example image of the interference pattern at 3.80 psi. The square of dash-line indicates the correlation area. (b) The intensity profile of the area indicated by dash-line in middle of figure 6.3(a). (c) The corresponding surface profile of the membrane. (d) The plot of displacement of membrane in center versus the pressure.

To calculate the pressure value from the recorded interference patterns, we adopted an image correlation method to analyze the holographic fringes. We use Pearson's correlation coefficient to characterize the similarity between two (gray scale) images, as described by the following equation:

$$r = \frac{\sum_i (A_i - A_m)(B_i - B_m)}{\sqrt{\sum_i (A_i - A_m)^2}\sqrt{\sum_i (B_i - B_m)^2}} \tag{14}$$

A_i is the intensity of the i th pixel in image A, B_i is the intensity of the i th pixel in image B, A_m is the mean intensity of image A, and B_m is the mean intensity of image B. Before measurement, the pressure sensor was calibrated with the digital gauge from 0 to 22 psi at 0.1 psi intervals. As the intensity of each pixel on the image varies continuously in terms of pressure, it is possible to add many more reference images by interpolating from the nearby reference images. The interpolation significantly alleviates the calibration work while enhancing the measuring resolution. After interpolation, the total number of reference images was increased by 10 times from the original one.

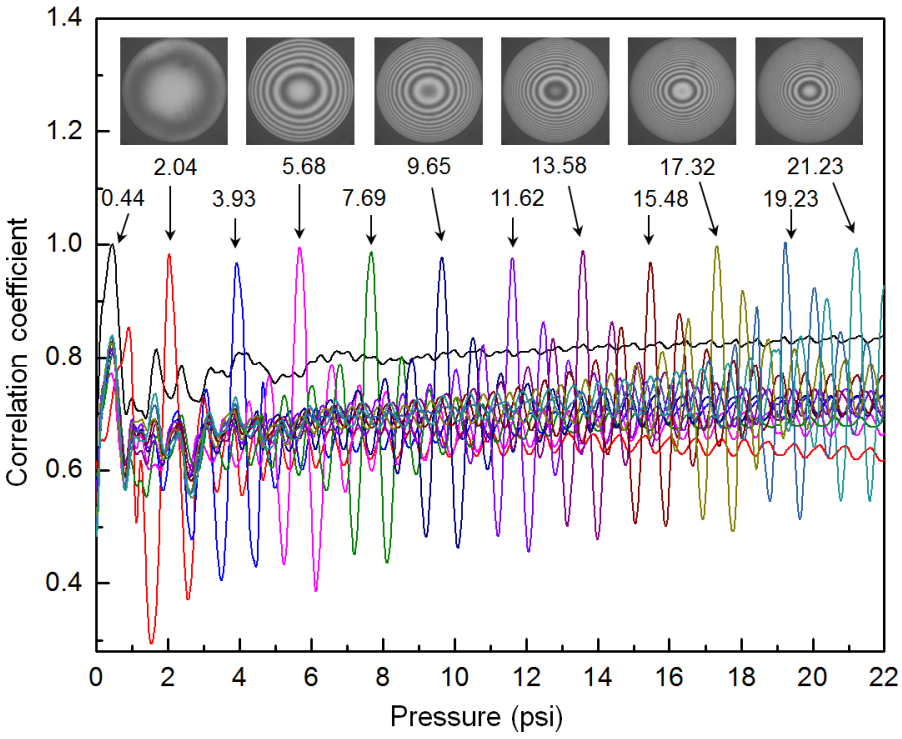

Figure 6.4: The plot of the correlation coefficient against the pressure of reference images. The different colors correspond to different measurement points. The insets show the recorded images at the corresponding pressures. The numbers are the measured pressure values obtained from the horizontal position of these maximum peaks.

In Fig.6.3(a), the square with dashed-line indicates the area over which the image correlation was calculated and the corresponding intensity profile is plotted in Fig.6.3(b). The relative heights of the each peak positions were calculated. The results are plotted in square dots in Fig.6.3(c). The red line in Fig.6.3(c) is the fitting curve that gives the profile of the membrane surface. Fig.6.3(d) is the plot of displacement of membrane in center area versus the pressure. It turns out to be very nicely linear relation. From the slope, the pressure sensitivity is calculated to be 0.444 μm/psi. The measurement results at twelve different pressure points in the range of 0-22 psi are shown in Fig.6.4 where the horizontal coordinate represents the pressure value of each reference images, and the vertical coordinate represents the correlation coefficient between the measuring image and the reference images. The area for imaging correlation is indicated by the square of dash line in Fig.6.3(a). Thus the measured pressure is determined by the x coordinate of the maximum peak on the plot of the correlation coefficient against the pressure of references.

The working range of this device is limited to be above 0 psi. We found even at very low pressure, the interference pattern becomes almost flat without fringes; the image correlation method is still effective and accurate. The upper limit of the working range can extend to 32 psi at which point the membrane begin to touch the other side of the cavity, as shown in in the left inset of Fig.6.5(a) at the pressure of 33 psi. Another possible factor that limits the working range is the image resolution of the correlation area. When the pressure is too high, the fringes become too dense and the camera can no longer distinguish them. We have stimulated different image sizes of the correlation area. Fig.6.5(a) shows the relation between the image length and upper limit of the working range. As the original image length of the correlation area is 542 pixels, we can find such image size is sufficient for the working range of 0-32 psi. For a given air-gap thickness, the working range can be changed by adjusting the thickness of the PDMS membrane. Fig.6.5(b) shows the dependence of pressure sensitivity on the membrane thickness. Although the working range of this pressure sensor can be extended to 32 psi, we only demonstrated the working range

of 0-22 psi. At each pressure condition, the measurements were repeated at least 5 times from based on different previous state. Fig.6.5(c) shows the error bar in the working range of 0-22 psi. The pressure accuracy is about ±1.4% of full scale. During the measurement we found the pressure error is related to the previous state. This was interpreted as the result of shape memory effect of the PDMS membrane. The temperature effect on the pressure accuracy is also significant as shown in Fig.6.5(d). All the measured values at different pressure condition have an increasing tendency with increasing temperature.

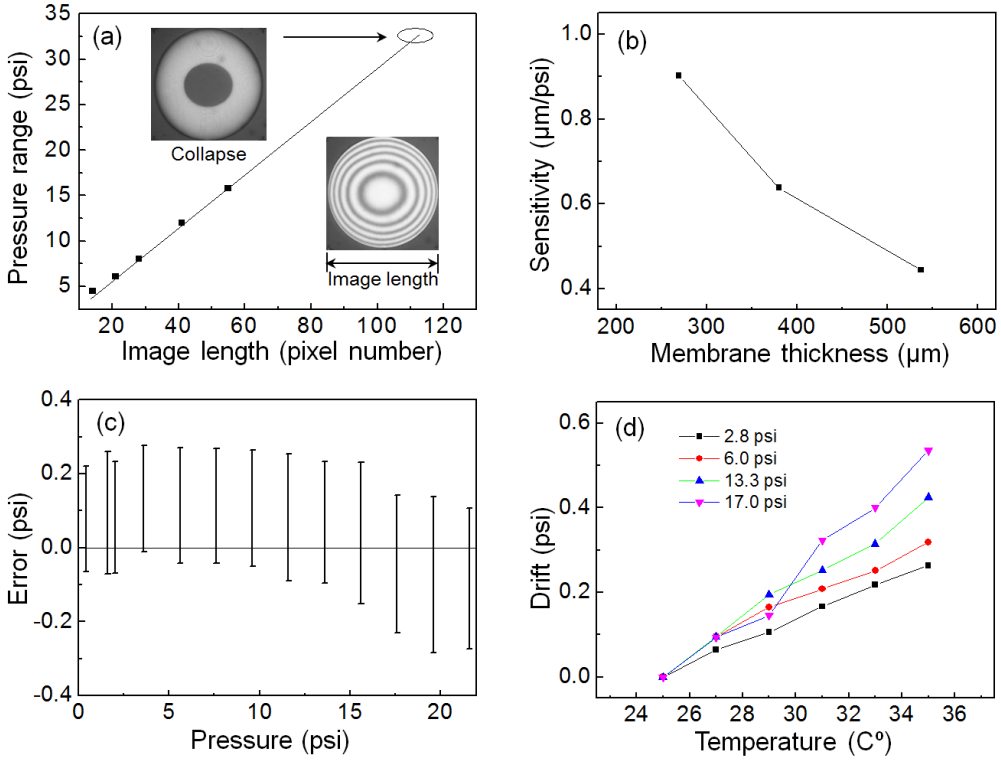

Figure 6.5: (a) The simulated result of the dependence of upper limit working range on the image length. (b) The relation between the pressure sensitivity and the membrane thickness. (c) The distribution of pressure error at different pressures. (d) The drift of measurement value with temperature at different pressure conditions.

In conclusion, we demonstrated a low cost, image based interferometric optofluidic pressure sensor on a polymer chip. Rather than using the research microscope and camera to measure the interference patterns as we did in this prototyping work, we believe a much cheaper external monitoring device can be constructed with plastic optics components, LED (light-emitting diode) light source and webcam type camera.

Chapter 7

Optofluidic membrane interferometer

In this chapter, we present a novel image-based method to measure the on-chip microfluidic pressure and flow rate simultaneously by using the integrated optofluidic membrane interferometers (OMIs). The device was constructed with two layers of structured polydimethylsiloxane (PDMS) on a glass substrate by multilayer soft lithography. The OMI consists of a flexible air-gap optical cavity which upon illumination by monochromatic light generates interference patterns that depends on the pressure. These interference patterns were captured with a microscope and analyzed by computer based on a pattern recognition algorithm. Compared to the previous techniques for pressure sensing, this method offers several advantages including low cost, simple fabrication, large dynamic range and high sensitivity. For pressure sensing, we demonstrate a dynamic range of 0-10 psi with an accuracy of ± 2% of full scale. Since multiple OMIs can be integrated into a single chip for detecting pressures at multiple locations simultaneously, we also demonstrated a microfluidic flow sensing by measuring the differential pressure along a channel. Thanks to the simple fabrication that is compatible with normal microfluidics, such OMIs can be easily integrated into other microfluidic systems for in-situ fluid monitoring.

As a fast-growing field, microfluidics and lab on chip systems have found numerous applications in the areas of biochemical detection, analysis, synthesis and separations [3, 67-69]. Accurate pressure monitoring is crucial for the precise control of as the pressure which is directly related to flow in microfluidic system. For an example, precisely regulated pressure was utilized to generate a continuous profusion of nutrient media for cell culture on chip [70]. Instead of delivering of chemical reagent, pressure driven flow can also hand the biological sample. For an example, pressure driven flow was utilized to scan the Caenorhabditis elegans in a chip-scale optofluidic microscopy (OFM) device [71]. In addition, pressure measurement has been also used for the characterization of the mechanical properties in microfluidic systems, such as liquid viscosity [72], red blood cell deformability [73] and hydrodynamic resistance of a single confined moving droplet in microfluidic channels [74].

Most current pressure measurements still rely on external pressure transducers [75-76]. However, due to the pressure dissipation and delay in transmission, it is difficult to accurately measure the local pressure in a microfluidic system using an external pressure sensor. Thus the integration of pressure sensors into microfluidic chip could be desirable for in-situ pressure measurement. To this end, several microfluidic pressure sensors have been demonstrated. Srivastava et al reported a pressure sensor based on monitoring the movement of a liquid-air interface where the trapped air is compressed in a sealed chamber [77]. But the material of devices is limited to non-gas-permeable material which is not compatible to the normal PDMS based microfluidic chip. Another method reported by Abkarian et al is based on monitoring the position of the interface between the test liquid and the reference liquid in the comparator channel [73]. This method requires a continuous flow of the test liquid and cannot measure the absolute pressure. Recently, Chung reported an image-based method to measure the pressure in microsystems by detecting the volume displacement of fluorescent particle suspensions [78]. This

method is simple to implement but the accuracy can be influenced by the variation of focus depth or the non-uniform distribution of the fluorescent particles.

Meanwhile, in-line microfluidic flow sensing is also desirable for precise flow control for lab-on-a-chip applications. Several types of microfluidic flow sensor were developed in the past. For an example, flow sensor that is based on sensing the temperature difference between two adjacent points in a micro-channel had been reported by Ernst et al [79]. Such flow sensors require complex fabrication to integrate heater and temperature sensors. Collins et al reported a microfluidic flow transducer based on measuring the electrical admittance of fluid [80]. However this method is not applicable to the conductive fluid. Lien et al reported a microfluidic flow sensor based on integrated optical fiber cantilever, but it also requires complicated fabrication and packaging process [81].

As an emerging field, optofluidics has enabled a number of novel optical functional devices built on microfluidic systems], Different from the normal on-chip interferometer that requires optical fibers and complicated package [14, 82]. Recently we induced the imaging based interferometer integrated on chip based on the mechanism of localized thin film interference [83-84]. In this work, we demonstrated a versatile imaging based method for simultaneously determining the microfluidic pressure and flow rate on a chip with the integrated optofluidic membrane interferometers (OMIs). In this device, the pressure is directly measured by the OMI which consists of a flexible air-gap optical cavity which generates interference patterns upon illumination by monochromatic light. Meanwhile, two identical OMIs combined with a simple microfluidic circuit compose a differential pressure flow meter. The whole sensing unit was integrated inside the chip with a small footprint. As the fabrication of the device is fully compatible with conventional PDMS based microfluidic chip; the sensing unit is ready to integrate into the other microfluidic chip for in-situ pressure and flow rate measurement. Thanks

to the interferometric method and the image processing algorithm, this method offers multiple advantages including high accuracy, large dynamic range and good reliability.

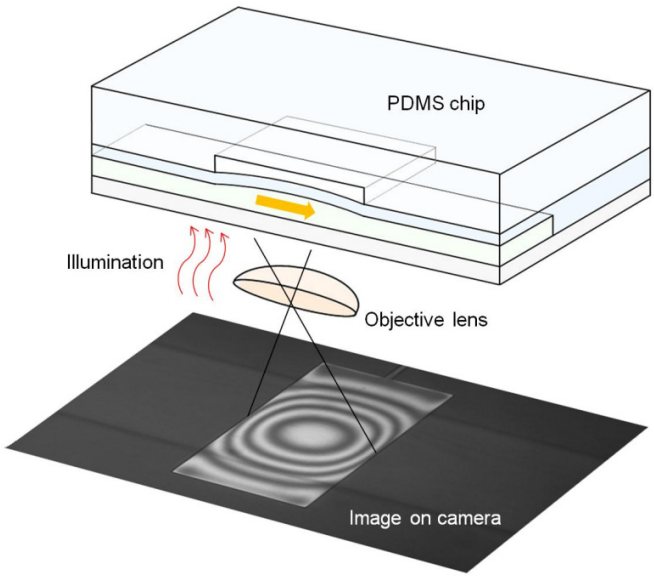

Figure 7.1: The schematic of whole apparatus for pressure measurement with OMI.

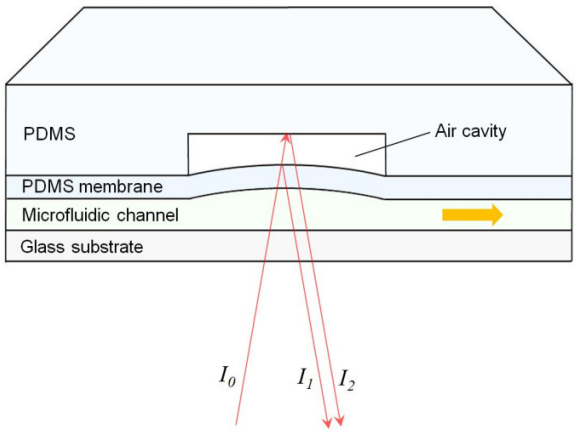

Figure 7.2: The structure of the OMI which contains a glass substrate, and two layers of PDMS.

The OMI was integrated in an optofluidic chip and monitored on a microscope. The schematic of the whole apparatus is shown in Fig.7.1. The chip was illuminated by a monochromatic diffuse light source. The image of the interference pattern from the OMI was projected onto a digital camera through an objective lens on the microscope. The pressure value was then obtained by analyzing these interference patterns. The chip was made of PDMS which was bonded onto a glass slide. As shown in Fig.7.2, the chip consists of two layers of structured PDMS layers on top of a glass substrate. The liquid flows inside a microfluidic channel formed between the glass substrate and the bottom layer of PDMS. Above the microfluidic channel, there is an air-gap chamber sandwiched between the two PDMS layers, where the bottom layer of PDMS functions as an elastic membrane for pressure transducing. The OMI mainly consists of microfluidic channel, PDMS membrane and an air-gap cavity. A temporal coherent light goes through the microfluidic channel and illuminates the air-gap cavity illuminates the chip. The reflected light from the two air-gap interferes inside the cavity interferes with each other constructively or destructively, depending on the air-gap thickness. The resulting total reflection intensity can be expressed as

$$I = I_1 + I_2 + 2\sqrt{I_1 I_2}\cos\phi \tag{15}$$

where I_1 and I_2 are the reflection intensities from the bottom and top PDMS-air boundaries respectively. Assuming the incident intensity at the bottom PDMS-air boundary is I_0, due to the low reflectivity on these two boundaries, we have $I_1 \approx I_2 \approx I_0 \times 4\%$, here the PDMS has a refractive index of 1.412. Thus multiple reflections can be neglected in this model. Meanwhile nice image contrast can be obtained due to $I_1 \approx I_2$. Note that there also exist reflections at the boundaries of PDMS-liquid and glass-liquid. However, the reflection there is much lower than

the one of the PDMS - air boundary. The phase difference ϕ between the two reflection beams depends on the air gap distance d .

$$\phi = \frac{4d\pi}{\lambda} + \pi \tag{16}$$

where λ is the wavelength of incidence light. When the fluids inside microfluidic channels is subjected to a pressure, the PDMS membrane is deformed to a convex shape towards the air-gap. Due to the thickness variation of the air-gap, the air gap cavity presents an interference pattern which reflects the pressure of the fluid. A digital camera on the microscope captures these interference patterns.

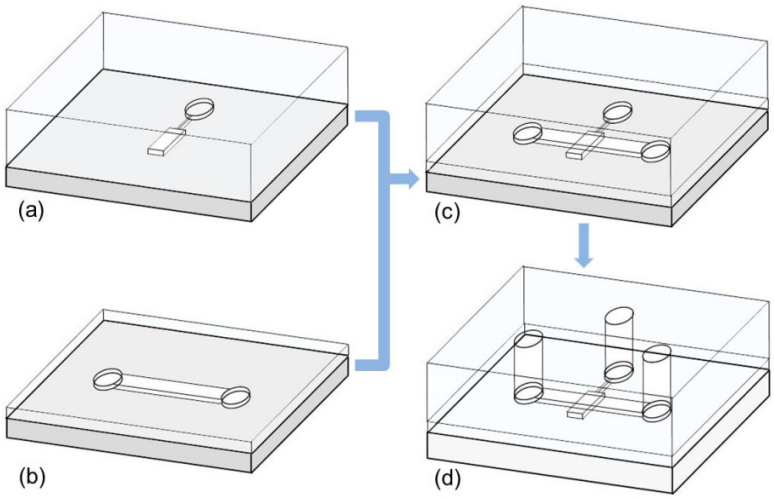

Figure 7.3: The fabrication process of the OMI.

The optofluidic chip was fabricated by multilayer soft lithography (MSL), which has been widely utilized to make the membrane valves and pumps on microfluidic devices [20]. The two PDMS layers were replicated from two different master molds that were patterned by standard UV lithography. The mold for the bottom layer of PDMS film was defined on a 50μm

thickness of SU-8 (Gersteltec, Switzerland). The width of the microfluidic channel underneath the bottom layer is 400 μm. The molds were treated with trimethylchlorosilane vapor (TMS, Sigma Aldrich). A monomer for PDMS membrane was prepared by mixing the prepolymer components in 10:1 ratio (base: curing agent, Dow Corning Sylgard 184). The bottom layer of PDMS should be thin enough since it works as a flexible membrane for pressure sensing. Meanwhile, the surface of the PDMS membrane should be flat to get the nice interference pattern. To fabricate such thin PDMS layer with smooth surface, we put several small pieces of silicon wafer around the edge of the wafer which contains the SU-8 mold. These small silicon pieces functioned as the spacer to fix the thickness of the PDMS membrane. After dispensing the PDMS prepolymer onto the SU-8 mold, the mold was covered by another blank wafer which was then slightly pressed by loading a weight. The wafer was coated with a layer of Chrome for anti-sticking between PDMS and wafer. After the PDMS prepolymer was cured in an oven, the PDMS membrane was carefully separated from the SU-8 mold and blank wafer. The PDMS membrane was then cut into the required size and transferred to another clean silicon substrate. The thickness of the PDMS membrane was measured on microscope by imaging its cross-section. The thickness of the PDMS membrane is 530μm in this chapter otherwise stated. The top PDMS layer of the chip was also prepared by replica molding from a SU8 mold which has a thickness of 20μm. This PDMS layer has a thickness of 4mm. Fig.7.3 shows the entire fabrication process; the two PDMS layers were treated by oxygen plasma (12W, 20s) and then bonded together on a homemade aligning setup. After drilling the holes, the bonded PDMS part was then bonded onto a glass substrate via oxygen plasma. The chip was finally baked in the oven at 100ºC for more than 24 hours to ensure the bonding strength. The Young's modulus of the PDMS was expected to be 4MPa according to literature [85].

The chip was measured with a bright field microscope (Infinity Microscope and Mitutoyo M Plan Apo 5×objective) with a built-in beam splitter for illumination. The light source was a

broadband light source (Dolan-Jenner, PL-800 Illuminator with tungsten lamp inside) added with a laser line filter (Thorlabs, FL632.8-1) that has a transmission line-width 1 nm. This monochromatic light source has sufficient temporal coherence to obtain high quality interference pattern without the speckle noise. Notice that the illumination onto the chip is a diffuse light source without spatial coherence. Due to the nature of thin film interference, we found the optical setup did not require very critical optical adjustment or alignment to get high quality of inference pattern, as long as the air-gap cavity was closed to the focal plane of the microscope. The image was recorded by a monocolor CCD camera (Scion, CFW-1312M). The pressure was generated from a precise mechanical air pressure regulator (100-AB, Air Control Inc.) And calibrated with a digital pressure gauge (Omega DPG4000). For the pressure measurement, the chip was connected with a tube and filled with pure water which was driven by the compressed air. In the microfluidic flow measurement, three types of liquids were used: water, 10% and 20% (by weight) glycerol in water solution (Sigma). The liquid flow was generated on a programmable syringe pump (New Era Pump Systems, Wantagh, NY). A disposable syringe containing the liquid was directly connected to the microfluidic chip through Tygon tubing. All the image analysis and calculation was done on commercial Matlab software.

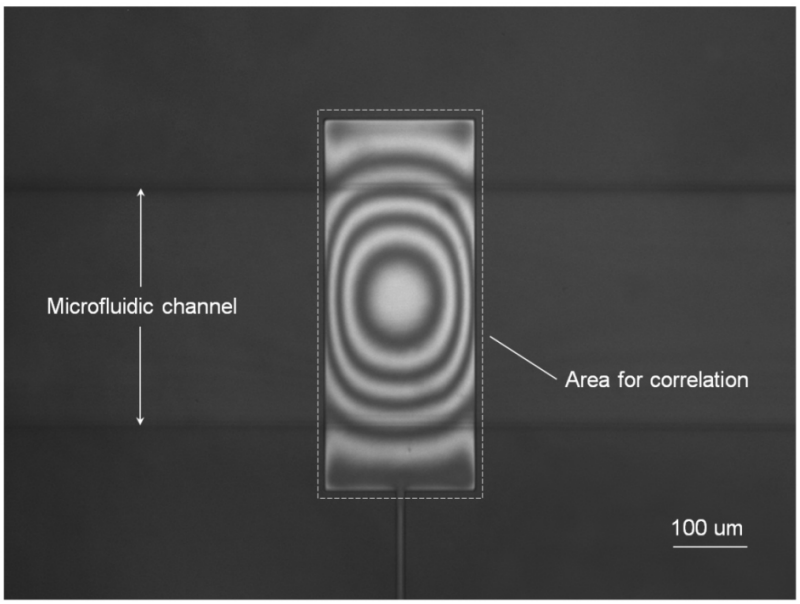

Figure 7.4: An example of the interference pattern at 6.5psi captured under microscope.

Fig.7.4 shows an example image of interference pattern at 5.5 psi of pressure taken on the microscope. The air-gap cavity has a rectangular shape with a size of 200 μm × 480 μm. A small channel at the bottom connects the air-gap cavity with a vent hole to keep the pressure inside the cavity be equal to the ambient air. Notice that all the pressure in this chapter represents the relative pressure to the ambient air. The interference patterns consist of several dark and bright concentric rings that move in or out upon the pressure decrease or increase. The microfluidic channel underneath the cavity is also visible. Compared to the cavity, the background area around the cavity is much darker due to the relative low reflectivity at the PDMS-liquid and glass-liquid interfaces. For an example here, the refractive indexes contrast of PDMS to water is 1.41/1.33; hence the reflection coefficient is calculated to be 0.09% that is much lower than the value of 3% at PDMS-air boundary.

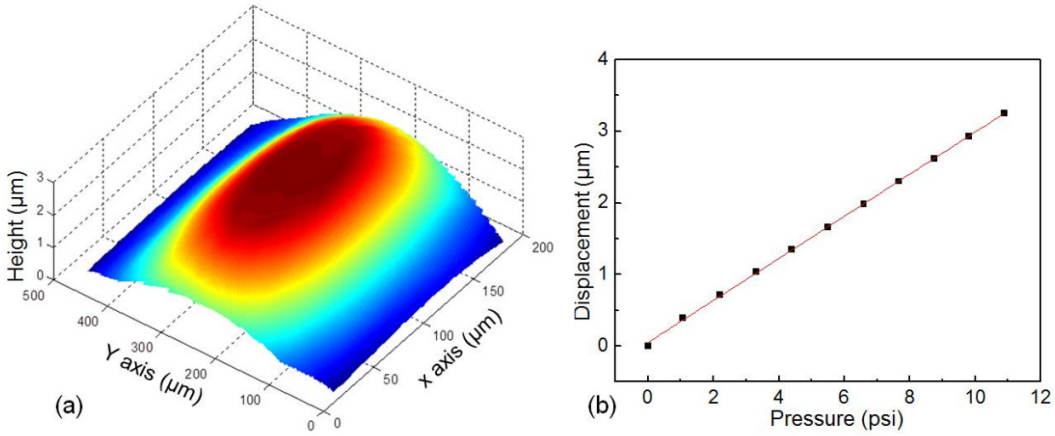

Figure 7.5. (a) The membrane shape deduced from the interference pattern at 6.5psi. (b) The displacement of the membrane in center area versus the pressure.

From the interference pattern in Fig.7.4, based on the equation (1) and (2), the shape of the membrane surface was calculated and is shown in Fig.7.5 (a). From the interference pattern, the displacement in the center area of the membrane was also calculated. Fig.7.5(b) shows the plot of displacement versus the pressure which gives a nicely linear relation. From the slope of the fitting line, the pressure sensitivity of this sensor is calculated to be 0.30μm/psi. As the air-gap cavity has a height of about 20 μm, thus we estimate that the membrane would touch the opposite side of the cavity at the pressure of larger than 66 psi which exceeds the upper limit of the pressure source we have.

To calculate the pressure value from the recorded interference patterns, we induced an image correlation method to analyze such holographic fringes. As each pressure level corresponds to a specific interference image, we compare the measured image to a database which contains a batch of the reference images with known pressure value that were obtained

during the calibrations. The measured pressure value is determined by which among the reference images gives the best fit to the measured image. To find the most matching images, we adopted the Pearson's correlation coefficient to quantitatively characterize the similarity between two (grayscale) images, as presented in the following equation [86]:

$$r = \frac{\sum_i (A_i - A_m)(B_i - B_m)}{\sqrt{\sum_i (A_i - A_m)^2} \sqrt{\sum_i (B_i - B_m)^2}} \tag{17}$$

A_i is the intensity of the i th pixel in image A, B_i is the intensity of the i th pixel in image B, A_m is the mean intensity of image A, and B_m is the mean intensity of image B. The correlation coefficient has the value $r = 1$ if the two images are absolutely identical, $r = 0$ if they are completely uncorrelated. In this work, firstly we calibrated the pressure sensor chip with the digital gauge from 0 to 10 psi at 0.1 psi intervals. At each pressure point during calibration, we took one picture as a reference image. As the intensity of each pixel on the image varies continuously within the calibration interval in terms of pressure, it is possible to add many more reference images by interpolating from the nearby reference images. The interpolation can significantly alleviate the calibration work; meanwhile it can enhance the measurement resolution. Fig.7.6 gives an example of such an interpolation between nearby reference images at pressure of 6.8 and 6.9 psi. After interpolation, the total number of reference images was increased to 10 times to the original one. In order to enhance the accuracy, a third order polynomial (cubic spline) interpolation was employed [87]. Thus each interval image is the computational result of nearby four images directly obtained from calibration.

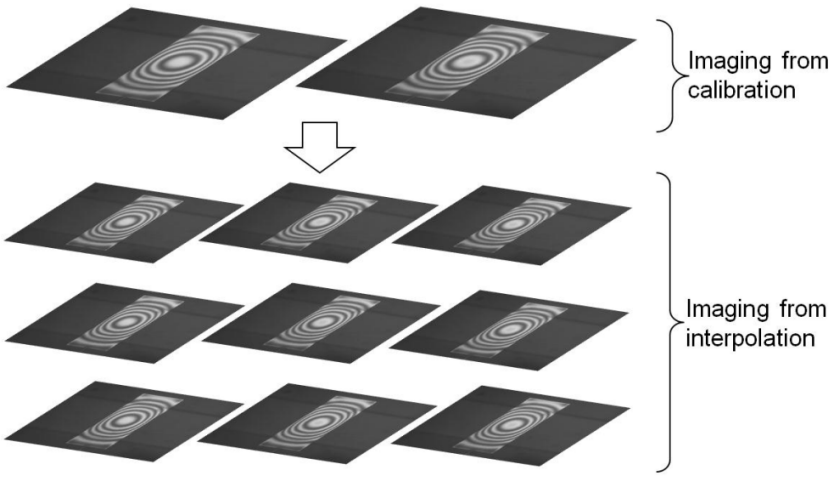

Figure 7.6: The Schematic of the image interpolation between the pressure of 6.8 and 6.9psi.

Fig.7.7 shows the measured results at five different points in the range of 0-10 psi. The insets are the interference patterns corresponding to each pressure labeled nearby. The horizontal coordinate represents the pressure value of each reference image, while the vertical coordinate represents the correlation coefficient between the measuring image and the reference images. To eliminate the influence from the area surrounding the cavity, we cropped all the images before calculating the correlation coefficient. The area is indicated by the square of dash-line in Fig.7.5. The correlation area for calculation has a size of 228 pixels by 516 pixels. This image correlation recognition method was proved to work well as we can see that the maximum peak on each curve can be easily discriminated and their values at these peaks almost reach 1. Thus the measured pressure is determined by the x coordinate of the maximum peak on this plot. Note that as the image correlation is based on the evaluation of an entire image, the pressure measurement is still realizable even there exist the tiny defects or dusts inside the OMI cavity.

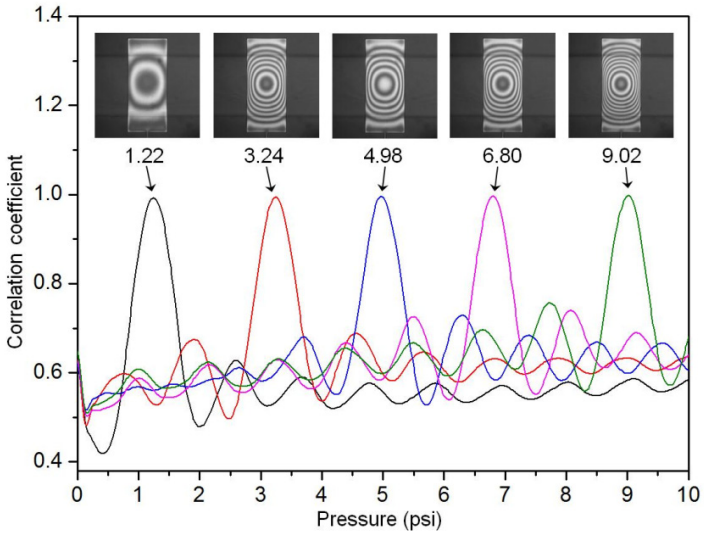

Figure 7.7: The plot of the correlation coefficient against the pressure of reference images. The insets show the images at the corresponding pressures. The numbers are the measured pressure values obtained from the horizontal position of these maximum peaks.

When the pressure sensor is subjected to negative pressure, the membrane surface in the air-gap cavity side will deform into a concave instead of convex shape at positive pressure. Due to the symmetry, the interference pattern may look similar in both conditions. Thus the working range of this device is only allowed to be above 0 psi. We also found the image correlation method is still effective and accurate even at very low pressure when the interference pattern becomes almost flat without fringes. The upper limit of the working range can extend to the point when the air-gap cavity begins to collapse. The working range of this pressure sensor can extend to more than 40psi which already exceeds the upper limit range of the air pressure regulator in this experiment. In this work we did the calibration and measurement in the range of 0-10 psi which was considered as the working range. Another possible factor that limits the working range is the image resolution of the correlation area. When the pressure is too high, the fringes become too dense and the camera may no longer be able to distinguish them if the image resolution is too

low. We stimulated different image sizes of the correlation area by numerically scaling the image. The original image size of the correlation area is 228 pixels by 516 pixels. We find even image size is reduced by a factor of 5, it is still sufficient to determine the pressure in the whole working range of 0-10 psi. During the experiment, we found too large thickness of the air-gap cavity can significantly degrade the image quality of the interference pattern.

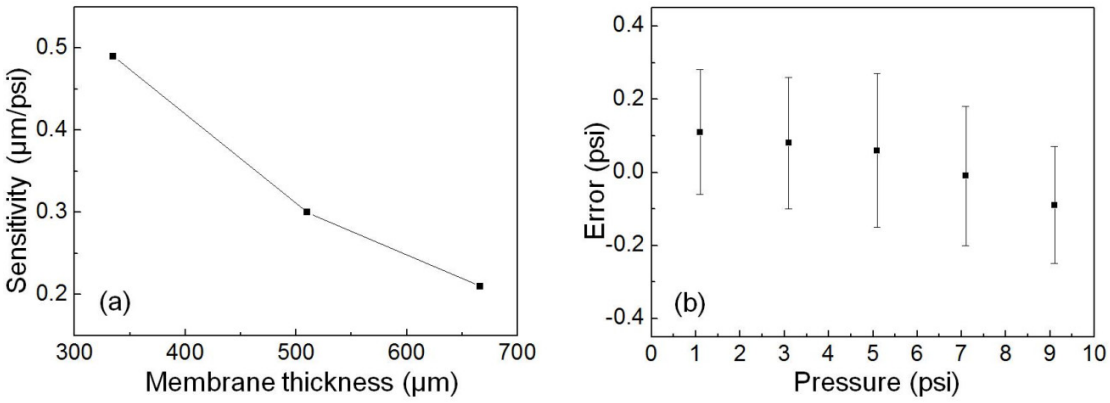

Figure 7.8: (a) The sensitivity of the pressure sensor versus the membrane thickness. (2) The distribution of measurement error at different pressure range,

In theory, to get clear interference pattern, the air-gap thickness should be within the coherence length of the light source and the depth of focus of the microscope. To get clear interference pattern, the wavefronts of two reflections that are projected onto the image plane from the cavity should be temporal coherent each other and without being blurred. From the testing we have done, the maximum of cavity thickness is about 50μm that still allows getting a decent interference pattern. For a fixed air-gap thickness, the working range can be chosen by adjusting the thickness of the PDMS membrane or the size of the cavity. The thinner PDMS membrane means high sensitivity and less working range, and vice-versa. Fig.7.8(a) shows the dependence of pressure sensitivity on the membrane thickness from experiment.

We investigated the accuracy of the device by comparing the measured value to the digital gauge. For each pressure condition, the measurements were repeated at least 6 times from different previous state. Fig.7.8(b) shows accuracy distribution in the working range of 0-10 psi. Here the error bars are the standard deviations of the measurements obtained from five sampling. From the graph, pressure accuracy is estimated to be about ±2% of full scale. During the measurement we also noticed that the pressure errors were related to the previous states, especially many different pressures were applied for a long time at previous states. This was interpreted as the result of shape memory effect of the PDMS membrane.

During the characterization, we also found that no critical alignment was required to obtain a nice interference pattern as long as the microscope focused well. The interference pattern of OMI was insensitive to the vibration or illumination condition. We also tested this device on a normal inverted research microscope (Olympus IX71, Japan) by modifying one of filter cubes. We replaced the original excitation filter with a laser line filter (Thorlabs, FL632.8-1), replacing the dichroic mirror with a piece of glass slide as a simple beam splitter and removing the emission filter. The chip was monitored under a low magnification objective (5×) in the epifluorescent configuration. We found that the interference pattern from the OMI cavity in this case had very similar quality to the ones shown in the Fig.7.7.

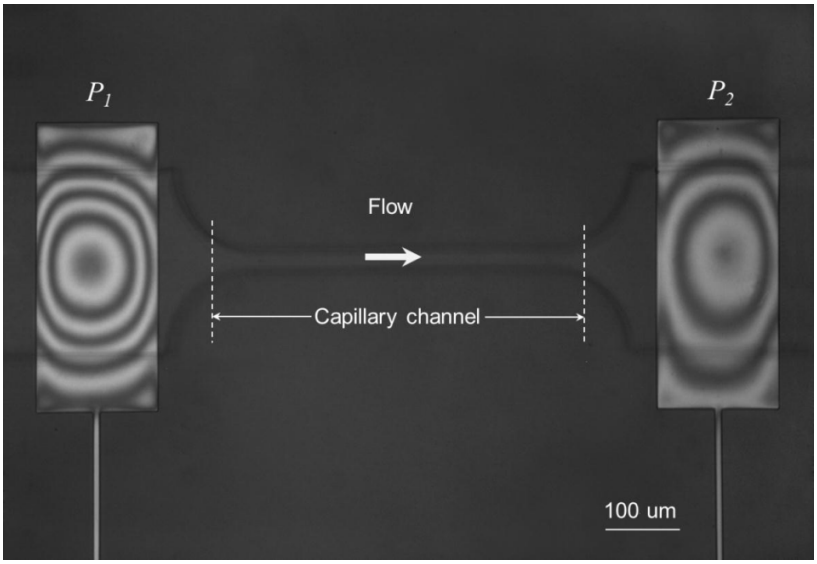

Figure 7.9: An example image of the flow meter which contains two OMIs for pressure sensing at up (P_1) and downstream (P_2).

In addition to the pressure sensing, a differential pressure based microfluidic flow-meter was also demonstrated by integrating such two OMIs with a microfluidic circuit on a single chip. The flow rate is calculated from the pressure drop induced by the flow along a narrow microfluidic channel. Fig.7.9 shows an example picture of the device captured on the microscope. Two OMIs are located at the two ends of the middle microfluidic channel for measuring the pressures of up and down stream respectively. The two OMIs have the same dimensions as presented in the above section. The narrow microfluidic channel in the center has a length of about 530μm and a rectangular cross-sectional shape with the size of 30μm × 20μm (width × height). For a steady laminar flow in a rectangular channel with constant cross-sectional areas, the pressure gradient is linearly proportional to the flow rate Q [88],

$$-\frac{\partial p(z)}{\partial z} = \frac{12\mu}{h^3 W} Q \tag{18}$$

where $p(z)$ is the pressure along the position z, μ is the fluid viscosity, W is the channel width, and h is the channel height. As the flow rate along the whole microfluidic channel is constant,

the total pressure drop ΔP between these two pressure sensors can be obtained shown equation (18) as show below,

$$\Delta P = -\int \frac{12\,\mu}{h^3 W}\partial z \cdot Q \tag{19}$$

From the fact that the differential pressure ΔP across the microfluidic channel is linearly proportional to the flow rate Q, experimentally we can calculate the flow rate Q from the following equation,

$$Q = k\Delta P = k(P_1 - P_2) \tag{20}$$

where k is a constant coefficient which can be obtained from calibration; P_1 and P_2 are the upstream and downstream pressure respectfully.

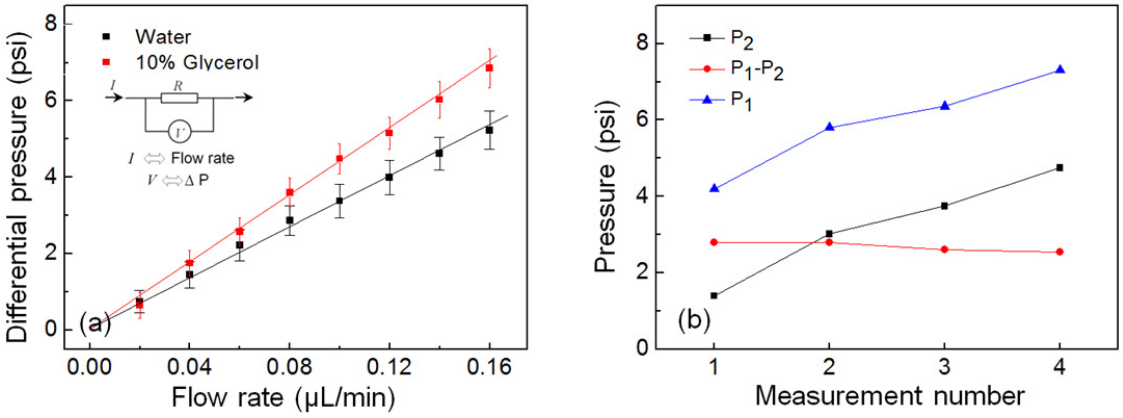

Figure 7.10: (a) The plot of the differential pressure (P2-P1) versus the flow rate for water and 10% glycerol solution. (b) The measurement results (P_1, P_2 and P_1-P_2) for a constant flow of 0.08μL/.min at the condition of different outlet pressure.

Fig.7.10(a) shows the measured differential pressures ΔP in response to various flow rates Q of the two different liquids. The inset figure shows a resistant electrical circuit as an equivalent model for this flow meter. Here the electrical current equivalents to the flow rate; the

voltage equivalents to the differential pressure. The two differential liquids include the water and glycerol-water solutions (10% in weight percent) with varying viscosity. The error bars are the standard deviations of ΔP obtained from five measurements with time intervals of three minutes. For each liquid, we can see a nice linear relationship between the flow rates and the differential pressures. The lines can fit the data points very well and each liquid corresponds to the lines with different slope rate. For a constant flow rate, if the fluid resistances at the outlet of the flow meter are different, we will get different sets of pressure values that may result different differential pressure. To investigate such effect on the flow rate measurement, we chose the water as the sample liquid, set a constant flow rate of 0.08μL/min. The outlet fluid resistance was adjusted by squeezing the tubing connected to the flow meter chip. When the outlet resistance increases, both the upstream and downstream pressure will increase. The experimental results are shown in Fig. 10 (b). The horizontal coordinate represents different measurements with increasing outlet resistance. The square and triangular dots indicate the upstream and downstream pressure respectfully; the circle dots are the calculated differential pressures. From the figure, we can see that the differential pressure slightly decreases with the overall pressure increment. This may be explained that the cross-section of microfluidic channel expands when the overall pressure increases due to the elastic property of the PDMS [89].

From above flow measurement, we can determine the coefficient value of k for each liquid. Thus for the practical flow rate measurement of the same liquid, the flow rate can be simply calculated by multiplying the differential pressure ΔP with k . For this device, we calculated the k values are 0.0297 and 0.0227 $\mu Lmin^{-1}psi^{-1}$ for water and 10% glycerol-water solution respectively. From the calibration results shown in Fig.7.10(a), we estimate the flow rate measurement on water has an accuracy of ±5% of full scale in the working range of 0-0.16μL/min. We also noticed that the k values are associated to the viscosities of each liquid with a linear relationship. The viscosities μ (obtained from literature) for water and 10% glycerol

solution are 1.005 and 1.310 respectively at temperature of 20ºC. The fact of that the coefficient of k/μ are almost same is in agreement with equation (19). Hence, this device can be also utilized to measure the liquid viscosity if the flow rate is known.

We develop an optical interferometric method for measuring both the microfluidic pressure and flow rate simultaneously on a chip based on the integrated OMIs. The measurement was realized by imaging the interference pattern from the cavity of OMI under a microscope upon monochromatic illumination. The device was fabricated with multilayer soft-lithograph which is low cost and can be easily migrated into other microfluidic system. Due to the nature of localized interference, the interference pattern can be insensitive to vibration or illumination condition. As long as the microscope focuses well, the nice interference pattern can be obtained without additional alignment. To analyze the interference pattern, we also presented an imaging correlation method which was proved to be highly reliable. Thanks to such optical interferometry method, the OMI shows high accuracy for pressure measurement. The sensitivity and working range for the pressure sensing can be chosen by adjusting the membrane thickness or the size of OMI cavity. The working range of the flow rate measurement can be also varied by properly designing the microfluidic resistance channel in between the two pressure sensors. Since each of the OMIs has small size, multiplex pressure and flow measurement in spatial on a single chip can be easily achieved by integrating multiple of such OMIs. In addition, with the integration of such OMIs into the other microfluidic system, the imaging method could allow simultaneous monitoring of the pressure and flow rate in channels, as well as the dynamic of the fluid or biochemical reactions that could be desirable for microfluidics and biology community.

Chapter 8

Tunable optofluidic 2×2 switch for reconfigurable waveguide

In this chapter, we present a pneumatically tunable 2×2 optofluidic switch for on-chip light routing that was controlled by compressed air. The device was fabricated with an optically clear elastomer-polydimethylsiloxane (PDMS) by soft-lithography. The optical switching is realized with a tunable air-gap mirror by which the light is deflected due to total internal reflection in the bypass state. When the device is subjected to high pressure, the air gap collapses and hence the light will be switched to the crossover state. The device had a switching speed of more than 5 Hz and an extinction ratio of 8 dB. This switch can be readily integrated with other microfluidic circuits. We demonstrated a simple reconfigurable optical waveguide circuit for dual-channel microfluidic spectroscopy measurement on a chip.

The convergence of microfluidic and optics led to the emergence of optofluidics where a number of optical devices have been realized. Optical and microfluidic components have been built on the same chip through optofluidic integration. Optical components such as lenses, mirrors, optical traps, liquid waveguides and light sources have been demonstrated [90-91]. Reconfigurability is another major advantage of optofluidics by which one can change the optical properties of the device by simply manipulating the fluids. Compared with rigid optical systems made of glasses, metals and semiconductors, optofluidic devices exhibit unique tunability due to the nature of fluids which offer a wide choice of compositions and shapes [4, 14]. For example, tunable photonics crystal and microfluidic dye lasers have been reported by changing the refractive index of liquids [36, 92]; tunable liquid lenses and electronic paper were realized utilizing the electrowetting effect [11, 93]; liquid-liquid waveguides were demonstrated based on flowing liquids with different indices of refraction [94-95]. Optical waveguides have been integrated in microfluidic chips for manipulation and detection of bio-chemical samples [96-98]. The optical switch plays a crucial role towards reconfigurable optofluidic circuits in which multiple components are integrated on a single optofluidic chip. Unlike the traditional optical switches designed for communications that are high cost and high speed, the primary requirement for optofluidic switches is simple fabrication that is compatible with integration with other components on the chip. Recently a 2×2 optical switch was demonstrated based on tuning of refractive index of liquid in a PDMS microchannel [99]. This switch relied on complex design for flow control. Several 1×2 optofluidic switches had been also demonstrated based on the liquid-core/liquid cladding waveguiding system formed by laminar flow [100-101]. These methods rely on accurate flow control and hence increase the control complexity. In addition, continual flow of fluids was required during operation. Thus a simple design of optofluidic switch with easy operation is desirable. We have recently introduced a pneumatically tuning mechanism for optofluidic dye laser in which the lasing wavelength can be tuned by air pressure [102]. Pneumatic tuning of optofluidic devices has the benefit of easy control since it employs a tuning

mechanism that is readily available in the microfluidic platform [103]. In this work, we present a pneumatically tunable 2×2 optical switch in which an air-gap mirror was switchable for light routing. The switch was fabricated on a polydimethylsiloxane (PDMS) chip and controlled by air pressure. Based on this switch, we also used demonstrate a simple reconfigurable optical circuit for dual-channel absorption spectroscopy on a chip.

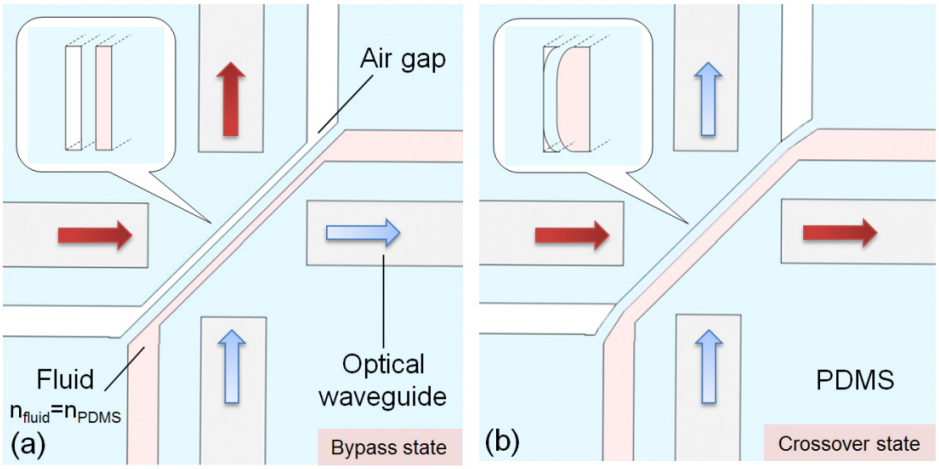

Figure 8.1: Top view of the device at the switching mode of crossover (a) and bypass (b); the insets show the cross-sectional view of air-gap channel.

Fig.8. 1 shows schematically the top view of the device. The chip was made with a clear elastomer (PDMS). The device contains the input and output waveguides in a four port configuration and an air filled micro-channel in the center which serves as the switchable air-gap mirror. The working principle is similar to the optical switch reported by Agilent Inc. where they used an air-bubble for beam deflection [20]. Fig.8.1 (a) and (b) correspond to the optical switch in bypass and crossover modes respectively. The microfluidic channel adjacent to the air-gap is filled with liquid that has the same refractive index as PDMS. In between these two channels, the thin PDMS membrane can be deformed when pressure is applied to the liquid. In the crossover

mode no pressure is applied to the liquid. The refractive index of PDMS is 1.412 which is much higher than the air; the critical angle for total internal reflection is 45.1º.

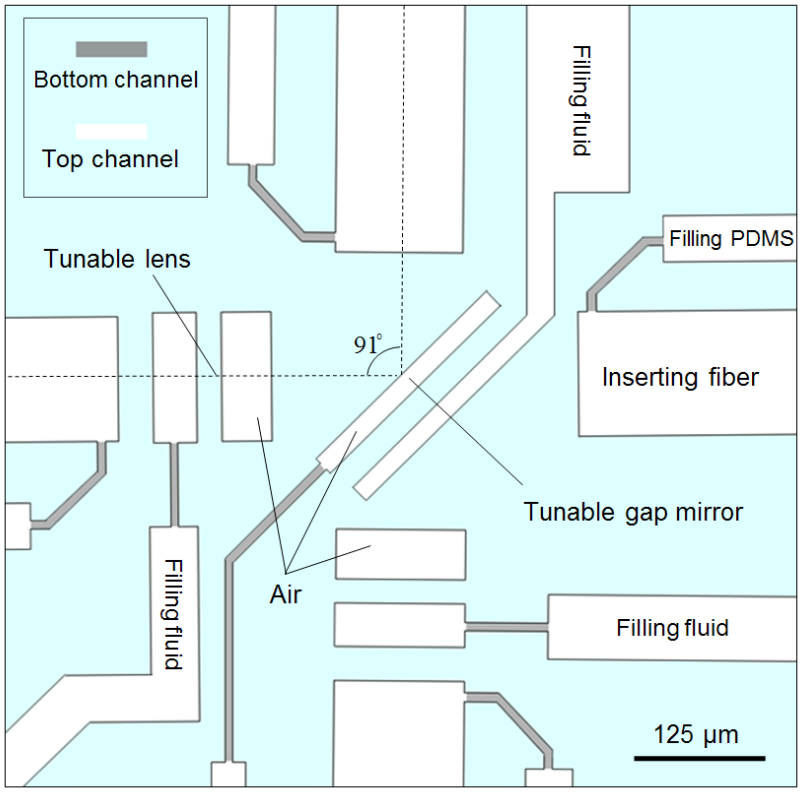

Figure 8.2: Top view of the dual layer structure of the optofluidic switch where the gray color represents the channels with 20µm thickness; the white color represents the channels with 125µm thickness.

In this design, as shown in Fig.8.2, we carefully chose 45.5 º of the incident angle which is slightly larger than the critical angle. Thus, in theory, the two incident beams can be totally deflected at the PDMS-air interfaces of the air-gap mirror. When pressure is applied to liquid, the PDMS membrane is deformed until the air-gap collapses. The schematic of cross-section view of the air-gap mirror and microfluidic channel is shown in the inset of Fig.8.1(a) and (b). As the PDMS is a soft material, when the two surfaces of PDMS make contact the air-gap will be

vanished and hence the light can go through it without any reflection or refraction. As a result, the light beams get switched from bypass mode to crossover states. When the pressure applied on liquid is released, the PDMS membrane will bounce back due to the elasticity of PDMS. In this experiment, the liquid was pressurized by compressed air; hence in fact the switch was pneumatically controlled.

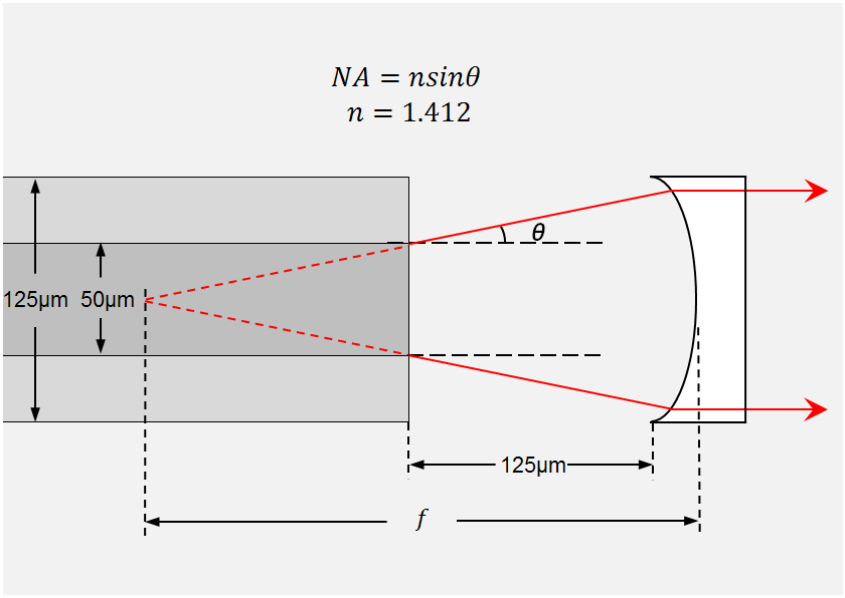

Figure 8.3: The schematic of an integrated lens for compensating the divergence of the beam from the fiber end.

In addition, as the output beam from the end of the fiber has a small divergence angle, as shown in Fig.8.3, we added an integrated tunable micro-lens to focus the beam and hence compensate the divergence. As the multimode fiber has a numerical aperture (NA) of 0.22; the half divergence angle is to be 10 º. Based on our calculation, we estimated that the optimal focal length of the micro-lens should be around 300μm to get parallel output beam.

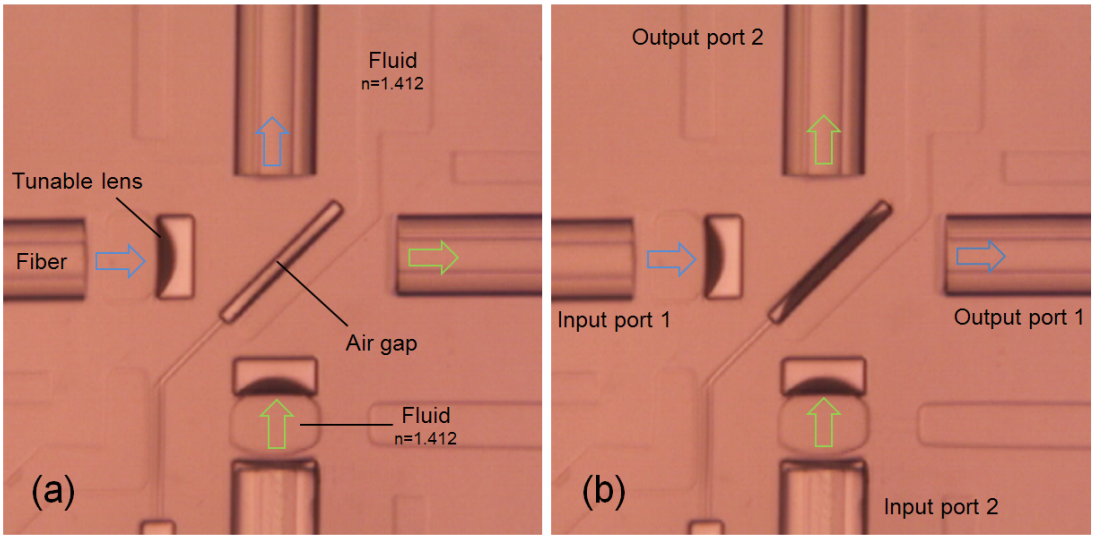

Figure 8.4: Microscopy images of the device at the switching mode of exchange (a) and bypass (b).

Two different chips were fabricated in this experiment. The first is a simple 2×2 optofluidic switch, and the second is a reconfigurable circuit by integrating the optofuidic switches with other components. Both devices have similar design and the same fabrication process. The chip was assembled with a structured PDMS layer with a flat PDMS layer. The structured PDMS layer was cast from an SU-8 mold patterned on a silicon wafer. The mold had a two layer structure fabricated by UV photolithography. Fig.8.2 shows the layout of the chip. The channels filled with gray color were cast from the bottom layer of the mold (thickness 15 µm). The parts filled with white color were cast from the upper layer of the mold and they have a higher thickness (125 µm). Each fiber port has the same width (125µm) that equals the width of the fiber. The purpose of the bottom layer of the mold was to define the microfluidic channel for liquid delivery; meanwhile, it can reduce the asymmetric deformation during mold fabrication and device operation when then the liquids pressurize channels. The upper layer of the mold defines the air-gap mirror and the fiber ports.

The silicon wafer was first spin-coated with 15μm thickness of layer of negative photoresist (SU-8 1060, Gersteltec), then it was exposed to UV-light through a mask and developed. After hard-baking on a hotplate at 120 ºC for half hour, the wafer was spin-coated with a second layer of 125 μm thickness of photoresist (SU8 1075 Gersteltec). Then the wafer was aligned and exposed on a mask aligner where the mask was aligned to the markers defined by the first layer of photoresist. Finally the mold was subjected to a hard baking at 160 ºC in the oven for 2 hours to improve the sidewall smoothness and the adhesion to substrate. Then the mold was treated with trimethylchlorosilane vapor (TMS, Sigma Aldrich) to prevent adhesion during PDMS casting. A 5 mm thickness of PDMS prepolymer (10:1 mixture of based and curing agent, Sylgard 184, Dow Corning) was poured onto the master mold and cured in an oven for 1 hour at 100 ºC. The PDMS cast was then carefully peeled off from the mold. After oxygen plasma treatment for 20 seconds, the structured PDMS was brought into contact with another flat PDMS piece to get permanent bonding. The chip was then packaged with optical fibers. Before the fiber (step index multimode fiber with core diameter of 50 μm, out diameter of 125 μm, 0.22 NA, Thorlabs) was inserted into each of the four ports, the channels were filled with PDMS prepolymer through the bottom channels. This procedure was critical as the PDMS prepolymer functioned as an excellent lubricant for fiber insertion. In addition, after being cured, the filled PDMS acted as an index matching material for reducing light scattering. The fibers were fixed to the chip by UV glue.

Fig.8.4 shows microscopy pictures of the chip. Parts of microfluidic channels (refer to Fig.8.2) were filled with index-matching liquid (refractive index 1.412) which was prepared by mixing of Dimethyl sulfoxide (DMSO) and water. The measured width of the air-gap is 20 μm. The micro-lenses structures have a width 125 μm and height 125 μm, in which the fluid chambers were also filled with index-matching liquid. Both the flexible membranes in the tunable air-gap mirror and lens have the thickness of 20 μm.

During characterization, a helium laser (632 nm, 15mw) was coupled into a fiber that worked as the light source. The signal was detected by a photodiode (FDS010, Thorlabs) which directly connected to an oscilloscope (Tektronix). The air pressure was controlled by the air regulator (100-AB, Air Control Inc.) and measured by a digital pressure gauge (Omega DPG4000). The pressure switching was controlled by a miniature electromagnetic 3-way valve (Lee Company) which was driven by a homemade amplifier circuit and an electrical function generator and homemade amplifier circuit. The tube for controlling the switch was first filled with a short section of index-matching liquid and then connected to the chip. The other end of the tube connected to the valve. The valve was able to set the pressure to ambient to a high pressure. Such pneumatically control has been widely utilized in microfluidic chips for fluid control based on the membrane valves and pumps [20].

Fig.8.4(a) and (b) show the microscopy pictures of the switch in bypass and crossover states respectively. In the bypass state, the air-gap channel was switched to the ambient pressure. In the crossover state, it was switched to the high pressure provided by the air regulator. As shown in Fig.8.2(b), the light was launched into input 1, the output 1 and 2 were connected to the photodiodes. Fig.8.5 shows the typical waveforms of different signals in a same timeline. Fig.8.3(a) is the driving voltage of the electromagnetic valve. Fig.8.5(b) and (c) are the normalized intensity from the output port 1 and 2. Here we used a square wave to drive the valve with a switching frequency of about 2.3 Hz. The air pressure was switched between 0 and 1.1bar.

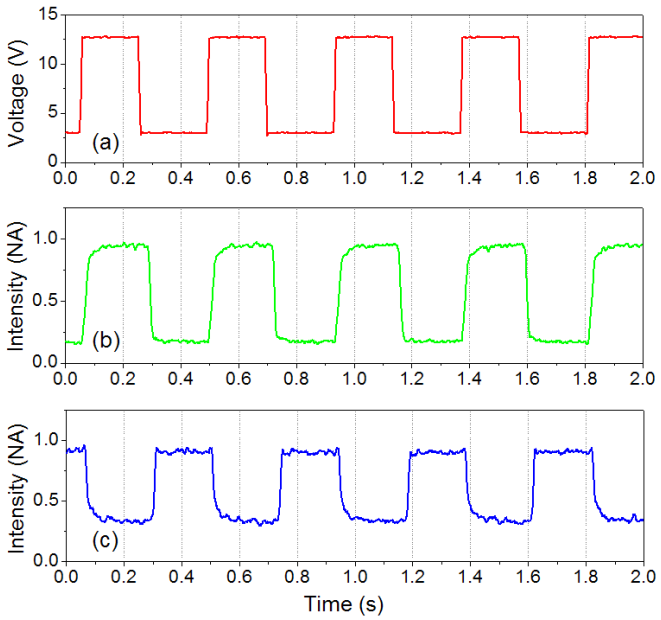

Figure 8.5: Wavegraph of the valve voltage (a) and the signal from output port 1(b) and 2(c).

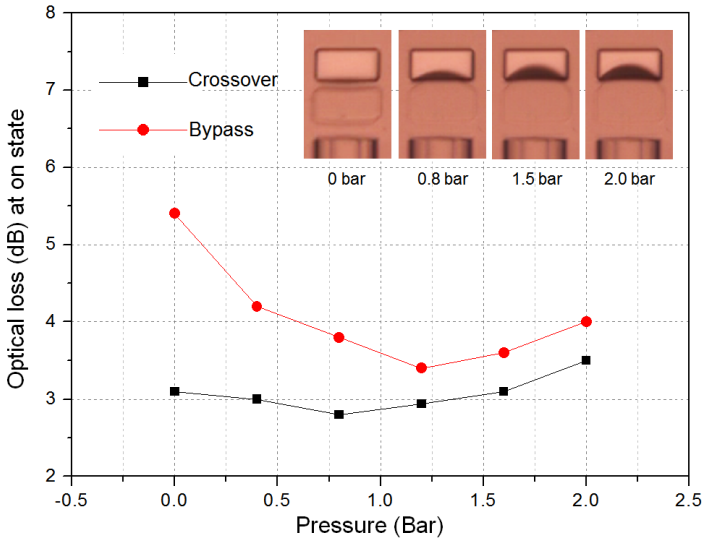

Figure 8.6: The dependence of the extinction ratio with pressure applied onto the liquid lens. The plots with square and circle shape dots represent the crossover and bypass mode respectively. The insets are the microscopy pictures of the lens at different pressure.

The micro-lenses included in the PDMS chip are also pneumatically tunable allowing us to optimize the coupling efficiency of the fiber into the microfluidic circuit. To find the optimal focal length of the micro-lens, we tuned the lens by applying different pressures and measured the optical loss at each output when the light is "on". The results are shown in Fig.8.6. We found that the optimal pressure was around 1 bar to get the minimal loss. The insets in Fig.8.6 are the microscopy pictures of the micro-lens at different pressures.

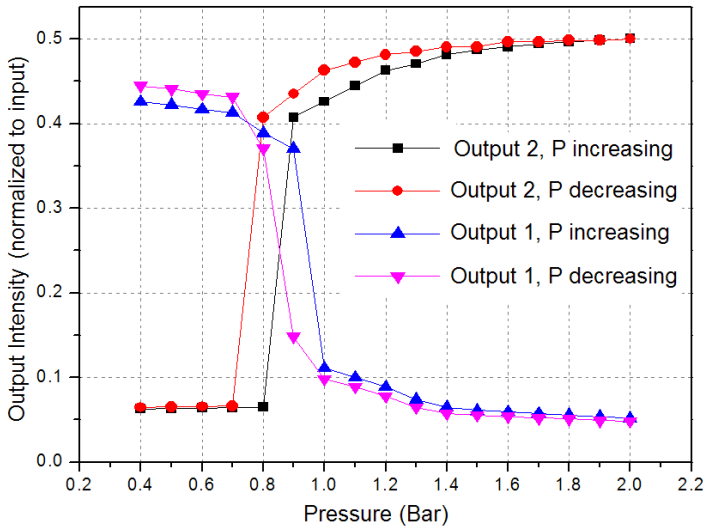

Figure 8.7: The plot of the output signal from port 1 and 2 with different pressure.

We also characterized the optofluidic switch in the static mode by continually adjusting the pressure applied onto the switch. Fig.8.7 shows the light intensity of output 1 and 2 (normalized to the intensity of the input) at different pressures. In this measurement, the laser was connected to input port 1; the pressure applied to the micro-lens was fixed to 1 bar. The measurement was done twice: from low to high pressure and then from high to low pressure. The dots with triangular (square) and diamond (circle) shape represent the signal of output port 1 (port 2) when the pressure was increasing or decreasing respectively. An extinction ratio of 8dB was achieved when the applied pressure reached 1.2bar. We also found that the extinction ratio can be

different at a given pressure. This hysteresis effect is attributed to the shape memory effect of PDMS and the adhesion when the PDMS membrane touched the other side of the air-gap channel. We repeated such measurements of the extinction ratio when input 2 was connected to the laser source; very similar results were obtained, which was inconsistent to with the symmetric design of the switch.

To further understand the dynamics of the switch, we plotted the normalized signals of the valve driving voltage versus the output, as shown in Fig.8.8(a). The pressure was switched between 0 and 1.1 psi with a frequency of 2.3 Hz. From the graph, we can see that the signals at ports 1and 2 complement each other. When the pressure was turned on, the switch responds rapidly as the membrane is pushed with the high pressure. When the pressure was turned off, the membrane took longer to recover, driven by the elasticity of PDMS. We measured the signal from output port 1 to characterize the dynamic response of the switch, as shown in Fig.8.8(b) of the dependence of rise and fall times on the switching pressure. As the pressure increases, the rise time decreases but at the same time the fall time increases. There are two main factors accounting for the increase of the fall time. First, when the pressure was removed, the membrane of the air-gap mirror bounced back, driven by its own elastic force. As the higher pressure induces larger displacement the membrane take longer to restore to its original state. Meanwhile the adhesion between two inner PDMS surfaces within the air-gap is also pressure-dependent. The second factor restricting the rise of the fall time was the degradation of the speed of the electromagnetic valve. The working range of the switch was found to be between 0.9 and 1.2 bar. Below 0.9 bar, the switch failed to work as the air-gap mirror took much longer to collapse. From the plot, we found the sum of rising and falling time reached the minimum of about 17 ms when the pressure was 1.08 bar. Thus the maximum switching frequency of this device was estimated to be about 5.7 Hz which was in agreement to our experiment observation.

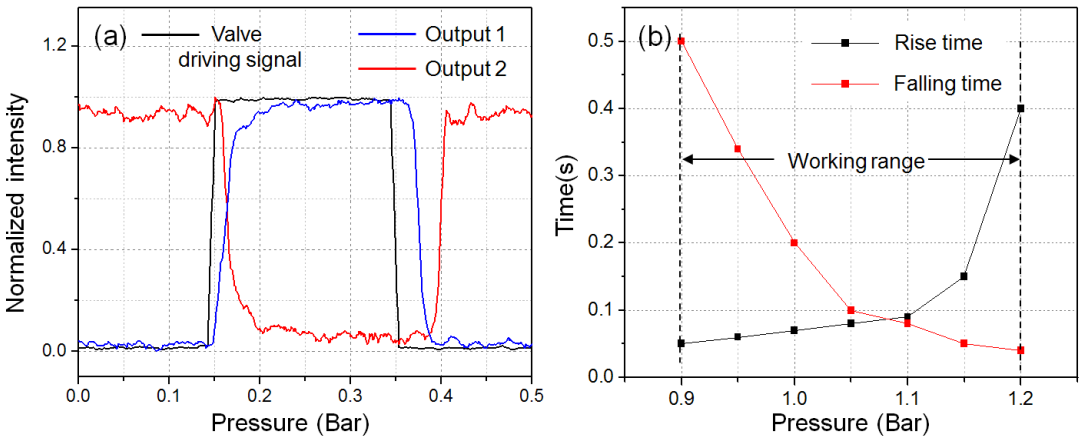

Figure 8.8: (a) Wavegraph of the normalized signals of valve driving voltage and outputs of the switch. (b) The dependence of rising and falling time on the switching pressure for the signal from output port 1.

As an example of the application, we demonstrated a simple reconfigurable light circuit by integrating two optofluidic switches on a single microfluidic chip. A dual-channel microfluidic absorption measurement was presented, in which the beam propagation route was selective by the switches, Fig.8.9(a) and (b) show the pictures of the chip at two different configurations. The chip is mainly composed of two identical microfluidic absorption cell, a pair of air-gap mirror and a pair of optofluidic switch. By controlling the switch 1 and 2, the input beam could go through either one of the two absorption cells. In the Fig.8.9(a), switch 2 had high pressure (1.2bar). So the beam passed through the bottom microfluidic channel which contained a methylene blue water solution. When switch 1 had high pressure (1.2bar), the beam went through the top microfluidic channel which contained a Rhodamine 6G water solution.

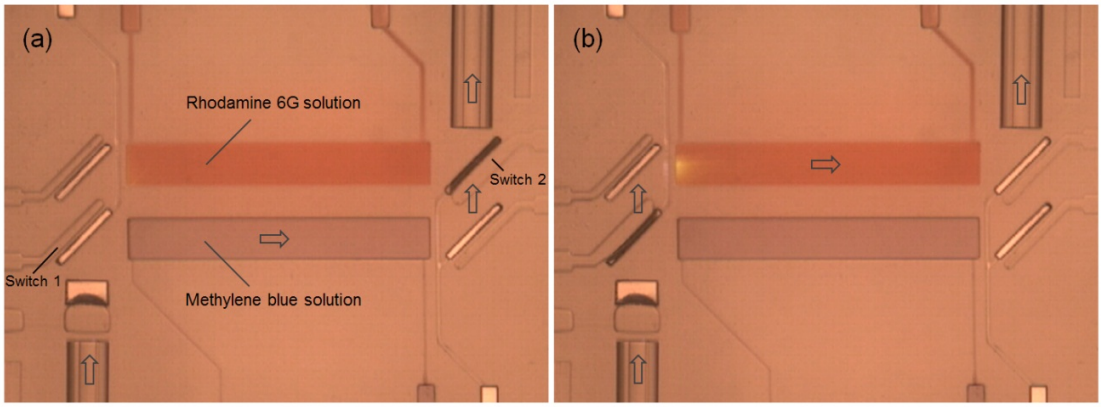

Figure 8.9: Microscopy images of the chip for dual channel spectroscopy. In (a) and (b) the beam passed through the microfluidic absorption cell filled with Methylene blue and Rhodamine 6G solution respectively.

During the experiment, the input fiber was connected to a wideband light source (Dolan-Jenner, PL-800 Illuminator); the output fiber was connected to a spectrometer (Shamrock 500 Imaging Spectrometer). Before filling the analyte, both the microfluidic absorption cells were filled with pure water to get the reference spectrums. The optical extinction at each configuration was also measured; the results are shown in table 1. After this, the microfluidic cells were filled with the dye solutions respectively. The methylene blue solution had a concentration of 9×10^{-5} mol/L; the Rhodamine 6G solution had a concentration of 1×10^{-4} mol/L. Fig.8.10 shows a normalized spectrum graph from the output fiber when the bottom cell (refer to Fig.8.9) was filled with pure water (black line, reference signal) and methylene blue water solution (red line). Although the total optical loss was large in this optical circuit, by make subtraction to the reference spectrum, we got the absorption spectrum of methylene blue solution (blue line). Fig.8.11 shows the measured absorption spectrum of Methylene blue (Black line) and Rhodamine (red line) solution respectively. These results were confirmed by an additional experiment obtained using the normal cuvette.

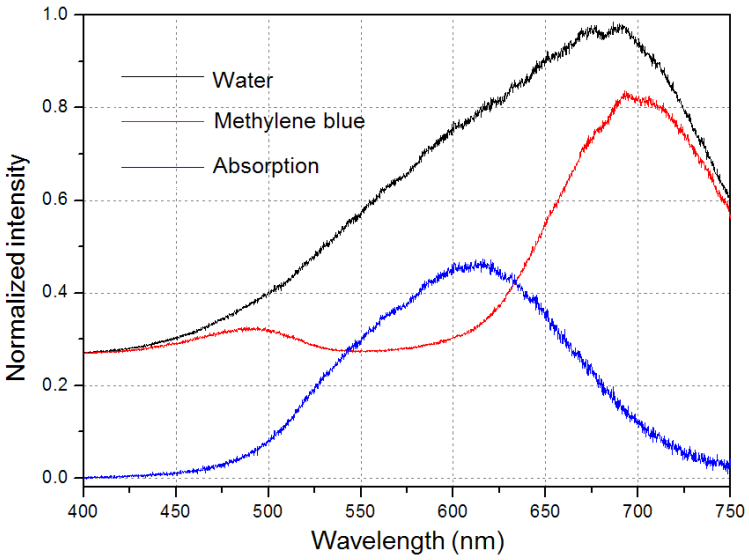

Figure 8.10: The directly measured spectrum from the output fiber when the microfluidic channel was filled with water (black line) and methylene blue in water solution (red line). The plot in blue is the calculated absorption spectrum of methylene.

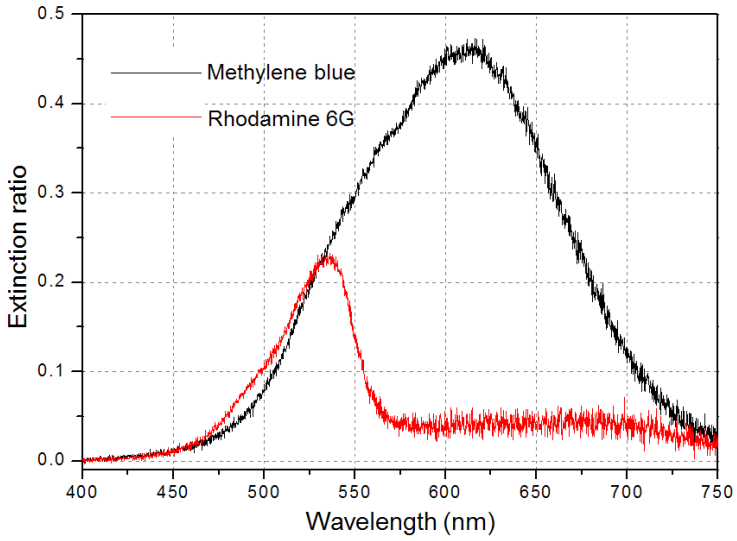

Figure 8.11: The measured absorption spectrum of Methylene blue (Black line) and Rhodamine (red line) on water solution.

In conclusion, we presented a pneumatically tunable 2×2 optofluidic switch which was incorporated into a PDMS based microfluidic chip. Light switching was realized with a tunable air-gap mirror that was actuated by the compressed air. The device takes the advantages of simplicity in both fabrication and operation, and it is readily to be integrated with other microfluidic structures. We also demonstrated a reconfigurable light circuit for dual- channel absorption spectroscopy measurement. We believe that the integration of such tunable optofluidic switches with state-of-the-art optofluidic components can pave the way for more complicated reconfigurable optical circuits on a chip.

Table 1. The optical extinction at each configuration

Pressure at switch 1 (bar)	0	1.2	0	1.2
Pressure at Switch 2 (bar)	0	0	1.2	1.2
Extinction ratio (dB)	23.8	11.2	10.6	21.5

Chapter 9

Optofluidic differential spectroscopy for absorbance detection

In this chapter, we present a novel optofluidic differential method for taking absorbance spectroscopy of sub-nanoliter liquid sample on a microfluidic chip. Due to the reduction of liquid volume, the absorbance detection in microfluidics is often hindered by either the low sensitivity or the complex fabrication. To address the issue, we introduced an optofluidic modulator which can be easily integrated into a PDMS (Polydimethylsiloxane) based microfluidic chip. The modulator was controlled by the fluid pressure; and the absorbance spectrum of analyte was obtained by making differential measurements between the analyte and reference medium. As the advantages, this method doesn't need complicated fabrication or package. It is compatible with conventional microfluidic chips, and the measurement can be done on a normal transmission microscope. The performance of the device was tested by measuring solutions containing methylene blue, with concentration as low as 13 μM.

Microfluidics refers to the science and technology of systems that manipulate small amounts of fluids, generally on the nanoliter scale and below. Microfluidic devices offer the ability to work with smaller reagent volumes, shorter reaction times, and the possibility of parallel operation. They also hold the promise of integrating an entire laboratory onto a single chip which is so called "Lab-on-a-chip" [3, 104-105]. In such integrated microfluidic systems, optical techniques have been extensively used and play important roles for chemical and biological analysis. For examples, fluorescence detection is a common way to track or analyze biological molecules in life science. [106-107]; Raman spectroscopy can be a sensitive method to detect trace amount of molecules without labeling [108]. Optical absorbance measurement is also a very common way to determine protein's concentration in water solution [109-110]; Integration of optical functions with microfluidic has been becoming an important approach in developing "Lab-on-a-chip" devices [111-113].

However, accompanying reduction of liquid volume, the optical signal from analyte also tends to decrease, which in particular gives the challenge for optical absorbance measurement. Deferent from a traditional optical absorbance spectroscopy where the sample's volume is tens of microliters, in microfluidic chip the available liquid volume is usually within the scale of nanoliter. As a result, the sensitivity of absorbance spectroscopy in microfluidics is normally restricted by the short absorbance length and other optical disturbance from chip structures. Hence the absorbance signal from the analyte can be easily covered by the environmental noise. To address such problems, many efforts have been made for microfluidic absorbance detection in the past. Among them, the integration of waveguides was a common way to reduce the surrounding noise. For example, Kutter's group reported an electrophoresis microchip with integrated waveguide for absorbance detection [114]. Two planar silicon oxide waveguides which connect to a microfluidic absorbance cell were utilized to launch the input beam and collect the transmitted light. Prabhakar reported a microfabricated polymer chip with integrated U-bend

waveguides for evanescent field absorption based detection [115]. The waveguide was fabricated with SU-8 photoresist, and part of the waveguide cladding directly contacts with the liquid sample. Nevertheless, the fabrication of such integrated waveguide is complicated and not compatible with conventional PDMS microfluidic chip; another difficulty is the light coupling between the waveguides and external optical components. Another method to improve the sensitivity of absorbance spectroscopy is by using multi-reflection absorbance cell. For example, Llobera reported a multiple internal reflection system which contains lenses, microfluidic channels and air mirrors on a planar PDMS chip [116]. The optical path was virtually enlarged compared to the flow cell due to the folded light propagation path. However, in this method, sophisticated packaging was required during inserting the optical fibers into the PDMS chip.

To address the above limitations, in this work we present an optofluidic differential method for absorbance spectroscopy on a microfluidic chip. It takes the advantage of the reconfigurability of optofluidics [58, 117-122], and can significantly improve the sensitivity of the absorbance spectroscopy on a microfluidic chip. This method is not only simple in implementation, but also compatible with conventional PDMS based microfluidic chip. No special fabrication or chip packaging is required. Normally, the absorbance signal in microfluidic chip is very weak, and the disturbance from the light source, construction material of microfluidic chip, and environment interference can easily cover the desired signal. To extract the signal from background, optofluidic differential method is based on making differential measurements among the analyte and reference. The key component of the device is an optofluidic modulator which is actuated by pressure modulation of liquid, and the measurement is done on a bright-field transmission microscopy.

The schematic of the optofluidic modulator is shown in Fig.9.1. It contains a micro-scale chamber which is divided into two symmetric sections by a thin membrane. The upper section is filled with the reference liquid; and the bottom section is filled with the analyte liquid. The

membrane is flexible and transparent. The incident light goes through the modulator in vertical direction for absorbance detection. The operation of the modulator is controlled by the pressure of the fluids in each section. When the fluidic pressure of the upper section is higher than bottom one, the membrane is pushed down, as shown in Fig.9.1(a). In such mode, the reference liquid occupies most of the chamber. Hence only the reference liquid contributes to the signal for absorbance spectroscopy. Conversely, when the fluidic pressure of bottom section is higher than upper one, as shown in Fig.9.1(b), only the analyte liquid contributes to the absorbance. With aid of the modulator, we measure the spectrums in each mode and then make subtraction on the spectrums corresponding to the opposite modes. As the absorbance from reference liquid is already known, the differential signal directly reflects the true absorbance spectrum of the analyte.

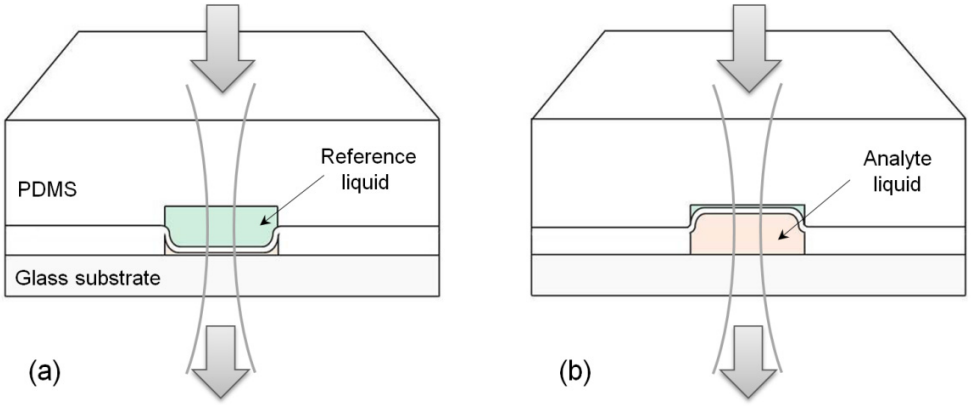

Figure 9.1: The schematic and working principle of the optofluidic modulator. The transparent thin film membrane in the chamber can be pushed down (a) and up (b) by the fluid pressure.

The measurement can be done on a normal bright field microscope in transmission mode. For single absorbance measurement, the liquid pressure can be controlled by manual valve. The measurement can be also continuous by Labview control, as shown in Fig.9.2 which is the schematic of the measurement setup in this experiment. A Labview board is utilized to control the electromagnetic valve and trigger the CCD on the spectrometer. During the measurement, the

modulator is kept switching at a fixed frequency, and the spectrometer captures the spectrums synchronously.

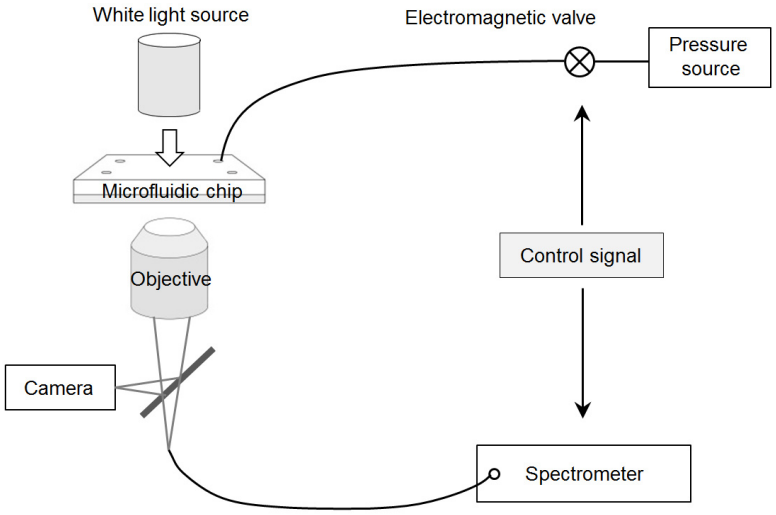

Figure 9.2: The schematic of the overall measurement setup for optofluidic differential absorbance spectroscopy.

The chip is made of a clear elastomer-PDMS. Multilayer soft lithography was utilized for chip fabrication [20, 123]. The chip is composed of two layers of PDMS which bond to a glass substrate. The detail fabrication process is shown in Fig.9.3. Two layers of PDMS were casted from two separated micro-fabricated molds. The molds were made of negative photoresist-SU8 on a silicon wafer which was defined by UV photolithography. Both of the SU8 photoresist have a thickness of about 15μm. The molds were treated with trimethylchlorosilane vapor (TMS, Sigma Aldrich) to prevent adhesion during PDMS casting. The bottom layer of PDMS in the chip was prepared by spinning PDMS prepolymer (10 : 1 mixture of the base and curing agent, Sylgard 184, Dow Corning), yielding an average thickness of about 16μm. The top layer of PDMS in the chip was casted from the mold and has a thickness of about 5mm. Each of the PDMS layer was baked in an oven for 1 hour at 80°C. Then the thick layer of PDMS was aligned and sealed with the thin PDMS layer after oxygen plasma treatment. Then the sealed PDMS slab

was peeled off from the mold and bonded onto a glass substrate. As the fabrication method is compatible with the conventional microfluidic chips which contain integrated micro-fabricated membrane valves and pumps, such optofluidic modulator can be easily integrated with other microfluidic functions on a single chip platform. The chip size is about 1cm×1cm×0.8cm (length×width×height).The both channels, on top and underneath the PDMS membrane, have the same dimension, the width is 100um.

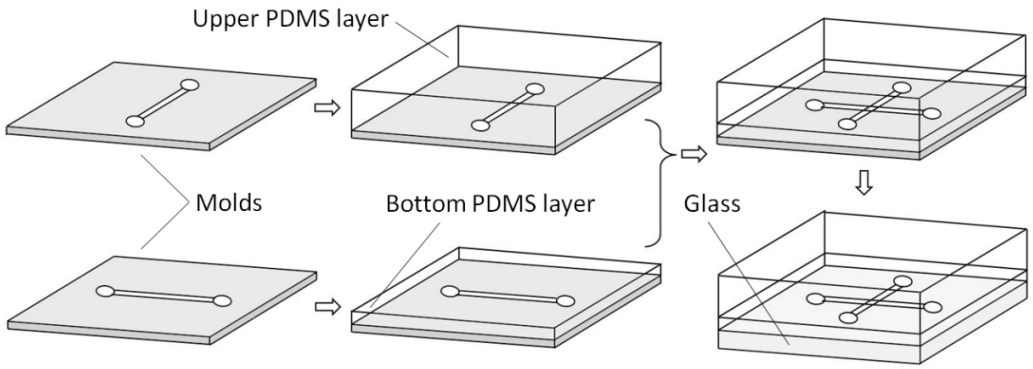

Figure 9.3: The fabrication process of a PDMS containing the optofluidic modulator.

Before the characterization, the upper and bottom microfluidic channel were filled with pure water and methylene blue (MB) water solution respectively. Here the pure water was the reference medium which was supposed to have zero absorbance; and the MB solution is the analyte which was supposed to be the measuring target. The channel filled with MB solution was connected to a compress air source with constant pressure at 0.5 bar (relative to the atmosphere pressure). The channel filled with water was connected to an electromagnetic valve (Lee Company) and another compress air source. The pressure applying on the water was switched to be either 0 or 1.5 bar. The valve was controlled by a Labview board with a current amplify circuit. Meanwhile, the Labview board also generated a square wave signal to trigger the CCD (charged-coupled device) camera (Newton DU940) on the spectrometer. The wave graphs of different signals in a same time line, including the valve control, CCD trigger and CCD shutter

(namely the exposure time), are shown in Fig.9.4. Since the optofluidic modulator had a response time and delay compared to the valve control signal, to synchronize the CCD camera and the optofluidic modulator, the CCD trigger signal had a slight delay with the valve control. During experiment, we chose the frame rate of camera at 4 Hz. The square wave for valve control had a frequency of 2 Hz. The camera exposure time for each frame was 1.2 ms.

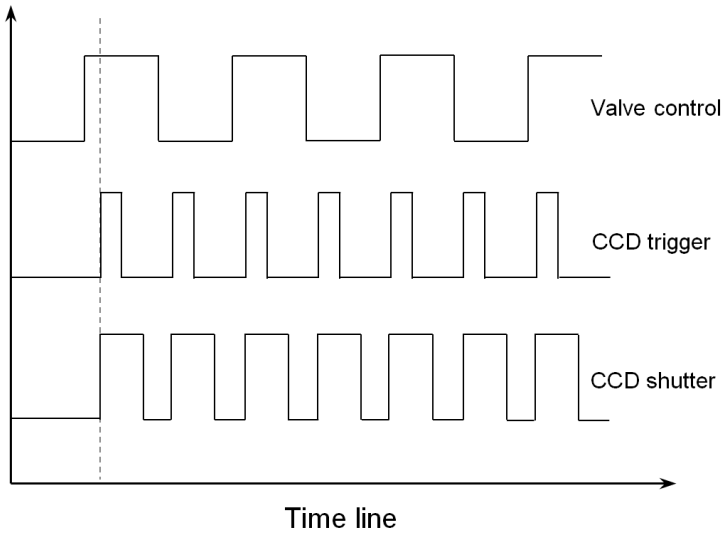

Figure 9.4: The comparison picture of different wave graphs which correspond to the valve control, spectrometer CCD trigger and CCD shutter.

During the characterization, the chip was mounted on a conventional bright field microscope (Infinity Microscope and Mitutoyo M Plan Apo 20× objective) in transmission mode. The illumination was based on a fiber based white light source.

Fig.9 5 shows the microscopy pictures of the chip in top view. The width of both channels is 100 μm. The square area indicates the optofluidic modulator where the two channels are cross overlapping. The channel in horizontal was filled with pure water, and the channel in vertical was filled with MB water solution (105 μM). The volume of the analyte inside the modulator is about 0.15 nano-litters. The circle in the center indicates the sampling area for

spectroscopy. Fig.9.5 shows the comparison pictures of modulator in different states. In Fig.9.5(a), the pure water was in high pressure, so the membrane of the modulator was pushed down. So the modulator was occupied by the water. In contrast, the water was in low pressure in Fig.9.5(b) when water was in low relative low pressure.

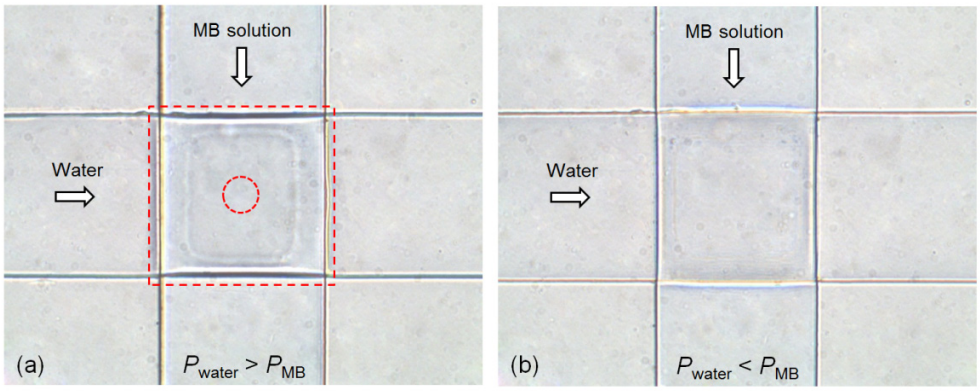

Figure 9.5: The comparison of microscopy pictures of the optofluidic modulator in two different states. The water was in high pressure in (a), and the MB solution was in high pressure in (b).The circle in the center indicates the spectroscopy sampling area.

From the microscopy pictures, we couldn't see a significant difference between these two states as the absorbance is very weak from the analyte. The modulator was kept switching continuously, the camera on the spectrometer captured a series of the spectrographs.

We chose two adjacent spectrographs when the analyte was MB water solution with a given concentration of 105 μM, as shown in Fig.9.6. The red line corresponds to the state when the reference fluid (water) has high pressure; and the black line corresponds to the state when the reference fluid (water) has low pressure. The difference of these two spectrums is shown in blue line by making substation from red line to black line. These two spectrums look very similar, and their differential spectrum is plotted by blue line. To increase the visibility of the differential spectrum, the magnified differential spectrum (blue line) is shown in the inset graph of Fig.9. 6.

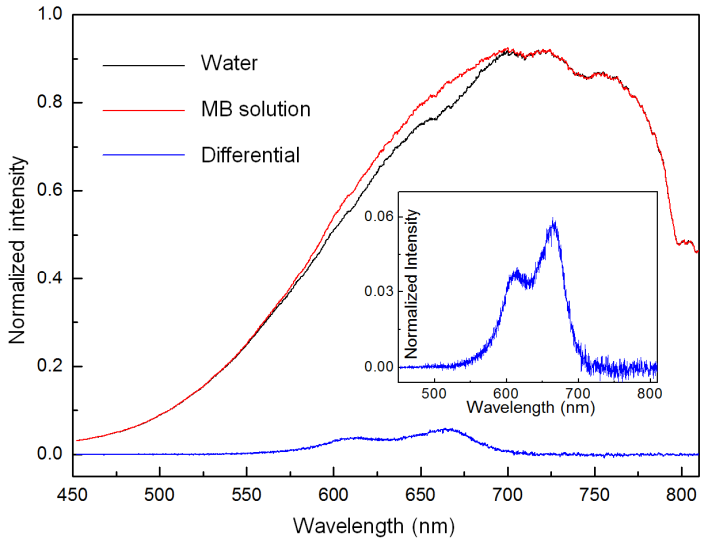

Figure 9.6: Two adjacent directly measured spectrographs. The red line corresponds to the reference fluid (water) being in high pressure; and the black line corresponds to the reference fluid (water) being in low pressure. The inset shows the magnified differential spectrum (blue line) from above two directly measured spectrums.

As the reference fluid is pure water which has almost zero absorbance in visible wavelength range, the differential spectrum can directly reflect the absorbance of the analyte. We tested the MB water solution with different concentrations on the same chip. The results are shown in Fig.9.7 which contains each of their differential spectrums.

According to Beer's law, as shown below, the intensity of the transmitted light I has the following relation with the incident light I_0.

$$I = I_0 \times 10^{-\varepsilon(\lambda)cl} \tag{21}$$

where $\varepsilon(\lambda)$ is the extinction coefficient of MB in water . c is the molecule concentration, and l is the optical path length of the absorbance cell. We define the normalized apparent absorbance by the following equation.

$$\frac{I_0 - I}{I_0} = 1 - 10^{\varepsilon(\lambda)cl} \tag{22}$$

As the absorbance is very weak, we can approximate the equation (2) to be a linear formula.

$$\frac{I_0 - I}{I_0} = \ln 10 \times \varepsilon(\lambda) cl \tag{23}$$

From Fig.9.7 we can see the MB solution has a maximum absorbance peak at 668 nm wavelength. In the following analysis, we choose the intensity data I_0 and I at wavelength of 668 nm. The dependence of normalized apparent absorbance with the MB concentration is plotted in Fig.9.8. The square dots are the measured data, and the blue line is the fitting line according to equation (23). The MB concentration was already known. $\varepsilon(\lambda)$ at 668 nm was measured by another experiment which used a standard cuvette, we measured $\varepsilon(668nm) = 7.8 \times 10^6 m^{-1} / M$. From the slope efficiency of the fitting line, we get the optical path length l to be 28 μm which is close to the sum of the heights of the upper and bottom channels. From the plot we estimated that this optofluidic differential method can be still accuracy enough when the MB concentration is as low as 13 μM. In addition, we found the normal environment light in the lab has negligible disturbance on the differential spectrum.

Without this differential method, it is very difficult to directly measure the absorbance of the fluid in the microfluidic channel with a transmission microscope. To get a reference signal, we shifted the chip a little by moving the stage; hence the channel was outside the detection area. Then the illumination light could directly go through the PDMS chip, and we got the reference signal. In such a case, we found the accuracy and reliability was much worse compared to optofluidic differential method. By using optofluidic differential method, the minimum absorbance detection limit is about 7×10^{-3}. Without such a differential method, a repeatable

result could be only obtained when the absorbance was as high as 2×10^{-2}. So there is a significant improvement in sensitivity by using such an optofluidic differential method. We also compared the absorbance sensitivity achieved by this method with the prior works. In the ref. 12, 13 and 14, in terms of absorbance, their sensitivities are 2.5×10^{-3}, 5×10^{-3} and 1.3×10^{-2} respectively. Although the sensitivities achieved by ref. 12 and 13 are comparable to our method, however, both of them need special fabrications rather than the conventional PDMS process. Also in ref. 14, much more volume of liquid was required in the folded absorbance cell.

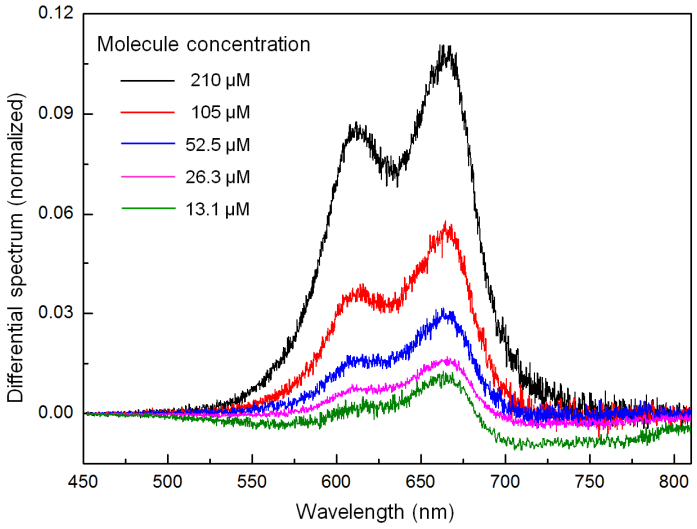

Figure 9.7: The measured absorbance spectrum of the MB water solution with different concentration by the optofluidic differential method.

We introduced an optofluidic differential method for taking absorbance spectroscopy on a microfluidic chip. Sub-nanoliter volume of liquid sample was required during the measurement. As the key component, the optofluidic modulator was fabricated by multi-layer soft-lithography on a PDMS chip. Hence it can be easily integrated in a conventional PDMS based microfluidic chip. Except the simplicity in fabrication, this method also takes the advantage of easy-to-use.

Firstly, the optofluidic modulator was driven by an external air pressure source which had been widely utilized in microfluidic control, thus it is readily available in many microfluidic experiments. Secondly, the absorbance measurement can be implemented on a conventional normal microscope without special optical components or chip packaging. Thus it is compatible with other functions on a single microfluidic chip. In addition, thanks to the differential method, the measurement is almost immune to the environment light. The measurement can be also in real time if the optofluidic modulator operated continuously. In future, we expect such optofluidic modulator can be integrated into other complex microfluidic system for lab-on-a-chip applications, for example, measuring the concentration of protein or DNA [124-125].

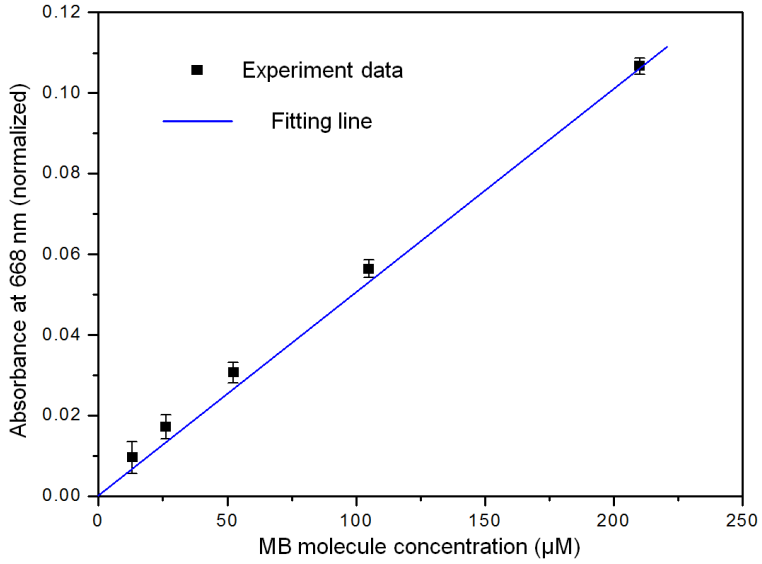

Figure 9.8: The plot of the absorbance of MB water solution with different concentration at 668 nm wavelength. The square dots are the experiment results and the blue line is the fitting line.

Chapter 10

Conclusion and outlook

Even though the optofluidic dye lasers have shown several impressive performances to this end, including single mode lasing and large wavelength tunability, we anticipate further improvements that will be crucial for its practical applications. Currently there are several main challenges regarding the optofluidic dye laser that remain unresolved. For example, the low pumping efficiency, short lifetime and instability are still the obstacles for commercial product. In the past few years, many groups have paid attentions to solve these problems. The bleaching of the fluorescence dye is another main factor that limit the lifetime of current optofluidic dye lasers. Very recently we are evaluating an alternative optofluidic laser instead of using PDMS chip. We designed and characterized an optofluidic fiber laser which contains the quantum dot colloidal solution as gain medium. Compared to the fluorescence dye, quantum dot are expected to give better life time and less bleaching [126]. Similar to the scheme of high power fiber laser, this fluidic fiber has double cladding structure for longitudinal lasing and pumping. The inner fluidic core of the fiber has small diameter and supports single waveguide mode. The exterior solid core supports multimode waveguide mode and large numeric aperture for efficiently coupling and guiding of the pumping light. The double cladding scheme ensure the pumping light to be absorbed thoroughly and uniformly [127]. From the primary experiment results, it has revealed significant improvement on the lasing stability and overall lifetime without refreshing the liquid laser medium.

As passive tunable elastomeric optofluidic device, optofluidic membrane interferometer provides a highly practical method for in-situ monitoring the liquid pressure and flow rate on conventional PDMS microfluidic chip. This method features the high sensitivity due to the nature

of optical interferometry. However, the accuracy is also limited by the memory effect on the elastic deformation of PDMS. In addition, the PDMS itself shows slight swelling effect once contacting some organic solvent. To improve the reliability and accuracy of the optofluidic pressure sensor, we are also seeking other materials to replace the PDMS to fabricate transducing the membrane, which is critical issue for practical clinic or industrial devices. The optofluidic pressure sensor has the most promising application in blood dialysis as disposable pressure sensor. Currently, the disposable pressure sensors use the MEMS technology, and the cost of single MEMS pressure sensor cost around 1 USD excluding the additional packaging cost. The optofluidic disposable pressure sensors are expected to have much lower production cost. And it also features more environment friendly compared to the electronic devices which always rely on the metals electrodes. At present, we are exploring the mass production of such imaging based optofluidic pressure/flow sensors in corporation with our industrial partner-FESTO in Germany.

The pneumatically tunable dye laser, optofluidic 2×2 switch and optofluidic modulator for differential spectroscopy are all considered as actively tunable elastomeric optofluidic devices. The integrated optofluidic switch provides the possibility to create a reconfigurable optical circuit in a planar microfluidic chip, based on which we have demonstrated a dual channel absorbance spectroscopy as an example of lab-on-a-chip application. The optofluidic differential spectroscopy was found to be a very effective way to measure the low concentration sample from tiny volume of the liquid inside microfluidic chip. No special external optical setup was required during the measurement. It can be realized on most of commercial microscopes in a transmission lighting mode. This feature could be favored by biologists as it can be easily implemented in normal microfluidic chip in their own lab. For example, biologists can integrated it with cell-culture on microfluidic chip for in-situ measuring the concentration of protein of DNA [128].

It is an important strategy to combine those different optofluidic elements into a complete system for practical lab-on-a-chip applications. Many more novel devise can be realized by

proper integrations of optofluidic elements into other microfluidic chips. For example, thanks to the high sensitivity, the optofluidic pressure sensor could be used to study the mechanical properties of cell membrane at single cell level [129]. Due to the nonlinearity of lasing process, optofluidic dye laser could be also used as high sensitive sensor for DNA detection [130].

In parallel, elastomeric tunable optofluidic devices can be also extended into the nano-optics or nanofluidic fields. Several tunable plasmonic nano-devices fabricated on stretchable PDMS substrates have been demonstrated very recently [131-132]. The combining of the elastomer based micro/nano devices with nanoplasmonic elements can be an interesting way for single molecule level imaging and spectroscopy [133]. Tunable elastic nanofluidic channel was also demonstrated recently on a PDMS chip for nanoparticles separation and molecule trapping [134]. One of the challenges of PDMS based tunable nano-device is how to achieve the high accuracy of control. We believe that it could be addressed by very fine pneumatic actuating or directly connecting to a precision piezo-actuator [135].

In addition to the work on elastomeric optofluidic devices, we are also working on several other optofluidic projects, such as the electrically tunable optical switch for optofluidic solar lighting, optofluidic photovoltaic/catalysis for water purification, and optofluidic pre-concentration for SERS spectroscopy. In the following text, I will make a simple introduction.

In a broad sense, solar lighting in the form of windows and skylights has been used for centuries. However, all these lighting methods lack the valuable features that are available from electric lighting. For example, some of these desirable features are: (1) minimal space occupation, (2) illumination well into the interior of the building, (3) constant illumination level, and (4) illumination control (on/off, intensity). To address the limitations that exist in prior art, we propose a reconfigurable optofluidic solar lighting system for indoor illumination and energy conservation [136]. Figure 10.1 shows a proposed optofluidic solar lighting system which

comprises the optofluidic solar concentrator, optical fibers (polymer core or liquid core), optofluidic switch and optical lighting terminals. They constitute a reconfigurable optofluidic illumination network, where the optofluidic light switch plays a key role.

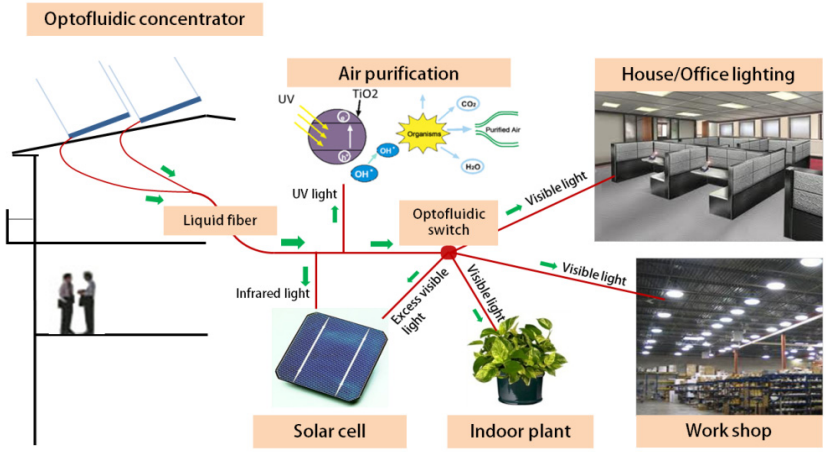

Figure 10.1: The overall diagram of the reconfigurable optofluidic solar lighting system in which the optofluidic light switch is a key component.

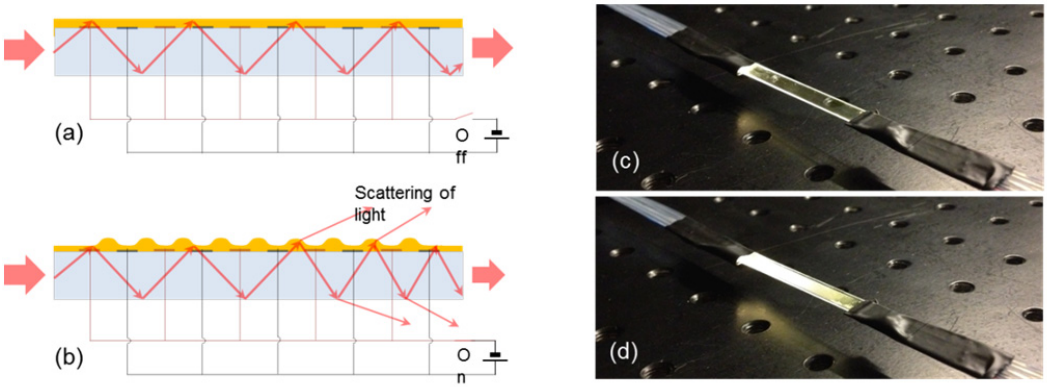

Figure 10.2: (a, b) Working principle of the tunable optofluidic switch by dielectrophoresis. Red line is the ray of the light path. The applied voltage is off (a) and on (b). (c, d) The picture of the optofluidic switch in work. (c)At the normal state (0V), the light goes through the slab waveguide. (d) When applying voltage (800V), light is partially escaped from the waveguide.

Simple design, low cost, compact size, and low power consumption are the primary desirable feature for the optofluidic switch in solar lighting. As shown in figure 10.2(a), the working principle of the switch is based on dielectrophoresis. The electrical field I able to manipulate the surface topography of a thin layer of transparent liquid (oil) on the glass slab waveguide [137]. When the sunlight intensity is affected by the clouds or other reasons, optical switches can make response in real-time hence keeping the constant illumination level at each lighting terminal. If the sunlight is strong and more than sufficient for illumination purposes, the reconfigurable optical network can direct the excess light for photovoltaic electricity generation. Figure 10.2(b) shows such a switch in working. We believe that switch can be produced in large size with very low cost due to the simple structure.

Another project we are working is an surface engineered superhydrophobic substrate for high sensitive Raman spectroscopy. It pre-concentrates the solute from a water droplet into a tiny area of nanostructured gold substrate for SERS measurement. Figure 10.3 shows the drying process of a water droplet on the photo-lithographic patterned superhydrophobic substrate with a metallic SERS substrate in the center.

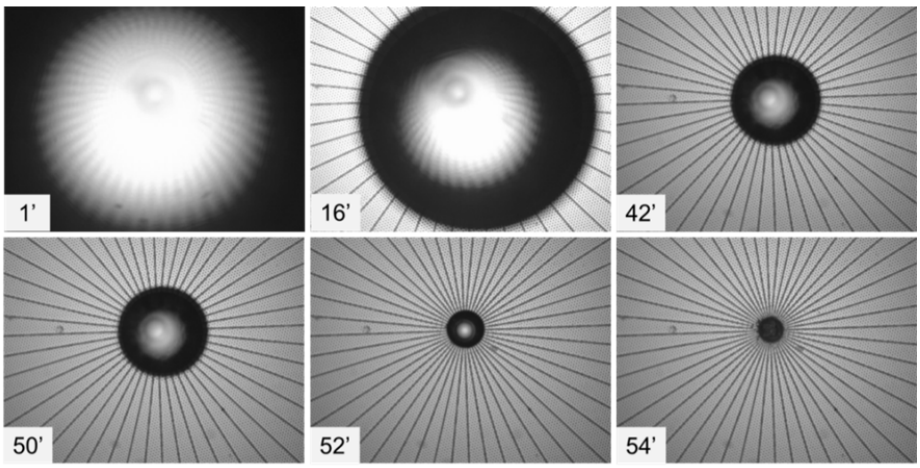

Figure 10.3: Sample pre-concentration on a patterned superhydrophobic substrate for SERS spectroscopy. The numbers in the pictures' corner represent the time elapsed in minutes.

The water droplet had an initial diameter of about 1mm. The water droplet can be automatically pinned in the center due to the centric gradient of superhydrophobicity. During the drying, all the solute in the water was forced to adhere to the tiny area of SERS substrate in center which has a diameter of 30 μM. The experiment result has revealed a dramatic enhancement of Raman signal compared to a normal SERS substrate where the liquid sample normally spreads into a large area.

In our perspective, extension from micro- to nano-scale will be the next strong trend in developing optofluidics. Different from traditionally optics where the light can be only controlled on the length scale down to a little below of optical diffraction limit, a new paradigm called plasmonics is emerging [138]. By using the localized surface plasmon resonances on certain metallic structures, we are able to control the light below the diffraction limit, down to tens of nanometers. For example, figure 10.4 (a) shows a nanoscale optical tweezers for optical trapping of a single nanoparticle with sub-wavelength mode volume [139]. The strong optical field confinement in the nano-optical antenna results in significantly enhanced optical field strength and large gradient of electromagnetic field, hence greatly enhancing the optical trapping force [140]. The strong optical field confinement on nanostructured metallic surface can also induce significant enhancement of Raman signal which named SERS [141]. On the other hand, nanofluidics is another rapidly developing research area which studies the behavior and manipulation of fluids and molecules that are confined to structures with nanometer (typically 1-100 nm) characteristic dimension [142]. When a fluidic channel is scaled down to dimension comparable to the Debye length, electrostatic interactions govern the ionic environment in such a nanofluidic channel. By utilizing the surface charge in nanofluidic environment, as shown in figure 10.4 (b), recently the researchers demonstrated a geometry-induced electrostatic trapping of nano-objects inside a nano-cavity [143]. The trap is based on the strong repulsion between particles and the walls of the compartments, which originates from the negative charge that both

carry. As another typical application, nanofluidics device can be extensively utilized to control the positioning and conformation of single DNA molecule [144].

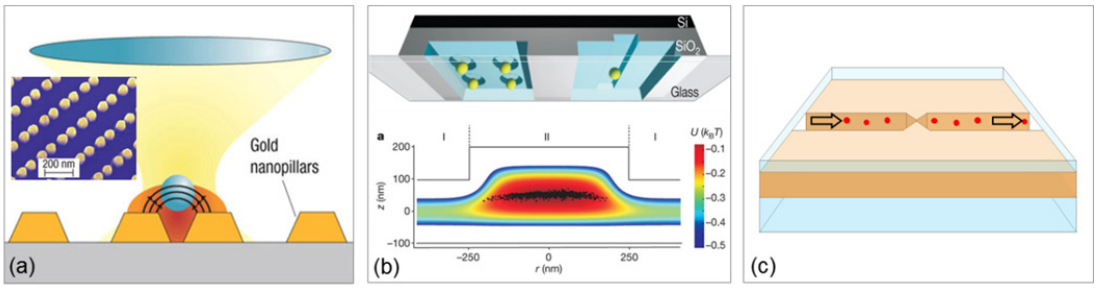

Figure 10.4: (a) Nanometric optical tweezers based on coupled pairs of gold nanodots. (b) Geometry-induced electrostatic trapping of nanoparticles in nano-channels. (c) An example of nano-optofluidics device we proposed, which is capable for fast screening the molecules that go through the nano-gap.

We anticipate the combination of nanoplasmonics with nanofluidics would create a novel nano-toolbox, in terms of "nano-optofluidics", which could lead the next latitude of method in studying and controlling the biomolecules/nanoparticles in a nano-environment. Figure 10.4 (c) shows one example of nano-optofluidic device that we proposed, which is capable for fast screening the molecules that go through the nano-gap. It comprises a hybrid plasmonic nanofluidic channel. The nano-gap formed by metallic layer that confines the optical field into a tiny spot. The event of a single molecule passing through the nano-gap will be optically recorded. This nano-optofluidic device can be considered as a tiny molecule flow cytometer for single molecule level counting or spectroscopy.

In summary, as a cutting edge research area, optofluidics is still a young and prosperous field to be further explored. By extending the optofluidics from micro- to nano-scale, we are pursuing and expecting many more exciting and innovative works that could come out in near future by synergic coupling between optics and fluidics.

"There's plenty of room at the bottom"

-----Richard Feynman

References

[1] D. Psaltis,S. R. Quake and C. H. Yang, "Developing optofluidic technology through the fusion of microfluidics and optics". *Nature*, 2006. **442** (7101), 381-386.

[2] C. Monat,P. Domachuk and B. J. Eggleton, "Integrated optofluidics: A new river of light". *Nat Photonics*, 2007. **1** (2), 106-114.

[3] G. M. Whitesides, "The origins and the future of microfluidics". *Nature*, 2006. **442** (7101), 368-373.

[4] U. Levy and R. Shamai, "Tunable optofluidic devices". *Microfluid Nanofluid*, 2008. **4** (1-2), 97-105.

[5] W. Z. Song,A. E. Vasdekis,Z. Y. Li and D. Psaltis, "Low-order distributed feedback optofluidic dye laser with reduced threshold". *Appl Phys Lett*, 2009. **94** (5).

[6] J. R. Adleman,H. A. Eggert,K. Buse and D. Psaltis, "Holographic grating formation in a colloidal suspension of silver nanoparticles". *Opt Lett*, 2006. **31** (4), 447-449.

[7] D. B. Wolfe,R. S. Conroy,P. Garstecki,B. T. Mayers,M. A. Fischbach,K. E. Paul,M. Prentiss and G. M. Whitesides, "Dynamic control of liquid-core/liquid-cladding optical waveguides". *P Natl Acad Sci USA*, 2004. **101** (34), 12434-12438.

[8] A. Q. L. W. Z. Song, C. S. Lim, P. H. Yap, "A Micro-Optic-Fluidic Spectrometer with Integrated 3D Liquid-Liquid Waveguide". *OMENS2007(IEEE/LEOS International Conference on Optical MEMS and Nanophotonics)*, 2007.

[9] B. Berge and J. Peseux, "Variable focal lens controlled by an external voltage: An application of electrowetting". *Eur Phys J E*, 2000. **3** (2), 159-163.

[10] T. Krupenkin,S. Yang and P. Mach, "Tunable liquid microlens". *Appl Phys Lett*, 2003. **82** (3), 316-318.

[11] S. Kuiper and B. H. W. Hendriks, "Variable-focus liquid lens for miniature cameras". *Appl Phys Lett*, 2004. **85** (7), 1128-1130.

[12] R. A. Hayes and B. J. Feenstra, "Video-speed electronic paper based on electrowetting". *Nature*, 2003. **425** (6956), 383-385.

[13] Z. Y. Li,Z. Y. Zhang,A. Scherer and D. Psaltis, "Mechanically tunable optofluidic distributed feedback dye laser". *Opt Express*, 2006. **14** (22), 10494-10499.

[14] W. Z. Song,X. M. Zhang,A. Q. Liu,C. S. Lim,P. H. Yap and H. M. M. Hosseini, "Refractive index measurement of single living cells using on-chip Fabry-Perot cavity". *Appl Phys Lett*, 2006. **89** (20).

[15] W. Z. Song,A. Q. Liu,S. Swaminathan,C. S. Lim,P. H. Yap and T. C. Ayi, "Determination of single living cell's dry/water mass using optofluidic chip". *Appl Phys Lett*, 2007. **91** (22).

[16] M. C. Belanger and Y. Marois, "Hemocompatibility, biocompatibility, inflammatory and in vivo studies of primary reference materials low-density polyethylene and polydimethylsiloxane: A review". *J Biomed Mater Res*, 2001. **58** (5), 467-477.

[17] A. Piruska,I. Nikcevic,S. H. Lee,C. Ahn,W. R. Heineman,P. A. Limbach and C. J. Seliskar, "The autofluorescence of plastic materials and chips measured under laser irradiation". *Lab Chip*, 2005. **5** (12), 1348-1354.

[18] F. Hua,Y. G. Sun,A. Gaur,M. A. Meitl,L. Bilhaut,L. Rotkina,J. F. Wang,P. Geil,M. Shim,J. A. Rogers and A. Shim, "Polymer imprint lithography with molecular-scale resolution". *Nano Lett*, 2004. **4** (12), 2467-2471.

[19] C. Markos,K. Vlachos and G. Kakarantzas, "Thermo-optic effect of an index guiding photonic crystal fiber with elastomer inclusions". *21st International Conference on Optical Fiber Sensors*, 2011. **7753**.

[20] M. A. Unger,H. P. Chou,T. Thorsen,A. Scherer and S. R. Quake, "Monolithic microfabricated valves and pumps by multilayer soft lithography". *Science*, 2000. **288** (5463), 113-116.

[21] D. V. Vezenov,B. T. Mayers,D. B. Wolfe and G. M. Whitesides, "Integrated fluorescent light source for optofluidic applications". *Appl Phys Lett*, 2005. **86** (4).

[22] X. Heng,D. Erickson,L. R. Baugh,Z. Yaqoob,P. W. Sternberg,D. Psaltis and C. H. Yang, "Optofluidic microscopy - a method for implementing a high resolution optical microscope on a chip". *Lab Chip*, 2006. **6** (10), 1274-1276.

[23] S. K. Y. Tang,B. T. Mayers,D. V. Vezenov and G. M. Whitesides, "Optical waveguiding using thermal gradients across homogeneous liquids in microfluidic channels". *Appl Phys Lett*, 2006. **88** (6).

[24] B. Helbo,A. Kristensen and A. Menon, "A micro-cavity fluidic dye laser". *J Micromech Microeng*, 2003. **13** (2), 307-311.

[25] S. X. Qian,J. B. Snow,H. M. Tzeng and R. K. Chang, "Lasing Droplets - Highlighting the Liquid-Air Interface by Laser-Emission". *Science*, 1986. **231** (4737), 486-488.

[26] S. I. Shopova,H. Y. Zhou,X. D. Fan and P. Zhang, "Optofluidic ring resonator based dye laser". *Appl Phys Lett*, 2007. **90** (22).

[27] A. E. Vasdekis,S. A. Moore,A. Ruseckas,T. F. Krauss,I. D. W. Samuel and G. A. Turnbull, "Silicon based organic semiconductor laser". *Appl Phys Lett*, 2007. **91** (5).

[28] S. Balslev and A. Kristensen, "Microfluidic single-mode laser using high-order Bragg grating and antiguiding segments". *Opt Express*, 2005. **13** (1), 344-351.

[29] Z. Y. Li,Z. Y. Zhang,T. Emery,A. Scherer and D. Psaltis, "Single mode optofluidic distributed feedback dye laser". *Opt Express*, 2006. **14** (2), 696-701.

[30] I. D. W. Samuel and G. A. Turnbull, "Organic semiconductor lasers". *Chem Rev*, 2007. **107** (4), 1272-1295.

[31] J. Ohtsubo, *Semiconductor lasers*. 2nd ed.; Springer Berlin: 2008.

[32] Z. Y. Li and D. Psaltis, "Optofluidic dye lasers". *Microfluid Nanofluid*, 2008. **4** (1-2), 145-158.

[33] H. Schmid and B. Michel, "Siloxane polymers for high-resolution, high-accuracy soft lithography". *Macromolecules*, 2000. **33** (8), 3042-3049.

[34] T. W. Odom,J. C. Love,D. B. Wolfe,K. E. Paul and G. M. Whitesides, "Improved pattern transfer in soft lithography using composite stamps". *Langmuir*, 2002. **18** (13), 5314-5320.

[35] C. Peroz,J. C. Galas,L. Le Gratiet,Y. Chen and J. Shi, "Compact dye laser on a chip fabricated by ultraviolet nanoimprint lithography". *Appl Phys Lett*, 2006. **89** (24).

[36] F. B. Arango,M. B. Christiansen,M. Gersborg-Hansen and A. Kristensen, "Optofluidic tuning of photonic crystal band edge lasers". *Appl Phys Lett*, 2007. **91** (22).

[37] E. P. Ippen and C. V. Shank, "Evanescent Field-Pumped Dye Laser". *Appl Phys Lett*, 1972. **21** (7), 301-&.

[38] G. Pendock,H. S. Mackenzie and F. P. Payne, "Tapered Optical Fiber Dye-Laser". *Electron Lett*, 1992. **28** (2), 149-150.

[39] H. J. Moon,Y. T. Chough and K. An, "Cylindrical microcavity laser based on the evanescent-wave-coupled gain". *Phys Rev Lett*, 2000. **85** (15), 3161-3164.

[40] X. S. Jiang,Q. H. Song,L. Xu,J. Fu and L. M. Tong, "Microfiber knot dye laser based on the evanescent-wave-coupled gain". *Appl Phys Lett*, 2007. **90** (23).

[41] B. R. Koch,A. W. Fang,O. Cohen and J. E. Bowers, "Mode-locked silicon evanescent lasers". *Opt Express*, 2007. **15** (18), 11225-11233.

[42] M. Gersborg-Hansen and A. Kristensen, "Optofluidic third order distributed feedback dye laser". *Appl Phys Lett*, 2006. **89** (10).

[43] S. Lacey,I. M. White,Y. Sun,S. I. Shopova,J. M. Cupps,P. Zhang and X. D. Fan, "Versatile opto-fluidic ring resonator lasers with ultra-low threshold". *Opt Express*, 2007. **15** (23), 15523-15530.

[44] K. Igarashi,M. Maeda,T. Takao,M. Uchiumi,Y. Oki and K. Shimamoto, "Operation of Rhodamine-6g Dye-Laser in Water Solution". *Jpn J Appl Phys 1*, 1995. **34** (6A), 3093-3096.

[45] E. B. Namdas,M. Tong,P. Ledochowitsch,S. R. Mednick,J. D. Yuen,D. Moses and A. J. Heeger, "Low Thresholds in Polymer Lasers on Conductive Substrates by Distributed Feedback Nanoimprinting: Progress Toward Electrically Pumped Plastic Lasers". *Adv Mater*, 2009. **21** (7), 799-+.

[46] Z. Y. Li and D. Psaltis, "Optofluidic distributed feedback dye lasers". *Ieee J Sel Top Quant*, 2007. **13** (2), 185-193.

[47] W. Z. Song,A. E. Vasdekis,J. W. Choi and D. Psaltis, "Micro-Air-Bag Actuated Tunable Optofluidic Elements". *2009 Conference on Lasers and Electro-Optics and Quantum Electronics and Laser Science Conference (Cleo/Qels 2009), Vols 1-5*, 2009. 1307-1308.

[48] Y. Sidorin and D. Howe, "Laser-diode wavelength tuning based on butt coupling into an optical fiber". *Opt Lett*, 1997. **22** (11), 802-804.

[49] X. M. Zhang,A. Q. Liu,D. Y. Tang and C. Lu, "Discrete wavelength tunable laser using microelectromechanical systems technology". *Appl Phys Lett*, 2004. **84** (3), 329-331.

[50] X. Wu,Y. Z. Sun,J. D. Suter and X. D. Fan, "Single mode coupled optofluidic ring resonator dye lasers". *Appl Phys Lett*, 2009. **94** (24).

[51] C. Karnutsch,C. L. C. Smith,A. Graham,S. Tomljenovic-Hanic,R. McPhedran,B. J. Eggleton,L. O'Faolain,T. F. Krauss,S. S. Xiao and N. A. Mortensen, "Temperature stabilization of optofluidic photonic crystal cavities". *Appl Phys Lett*, 2009. **94** (23).

[52] A. Groisman,S. Zamek,K. Campbell,L. Pang,U. Levy and Y. Fainman, "Optofluidic 1x4 switch". *Opt Express*, 2008. **16** (18), 13499-13508.

[53] X. L. Mao,J. R. Waldeisen,B. K. Juluri and T. J. Huang, "Hydrodynamically tunable optofluidic cylindrical microlens". *Lab Chip*, 2007. **7** (10), 1303-1308.

[54] C. Hilty,E. E. McDonnell,J. Granwehr,K. L. Pierce,S. I. Han and A. Pines, "Microfluidic gas-flow profiling using remote-detection NMR". *P Natl Acad Sci USA*, 2005. **102** (42), 14960-14963.

[55] D. S. Chang,S. M. Langelier and M. A. Burns, "An electronic Venturi-based pressure microregulator". *Lab Chip*, 2007. **7** (12), 1791-1799.

[56] S. Li,J. C. Day,J. J. Park,C. P. Cadou and R. Ghodssi, "A fast-response microfluidic gas concentrating device for environmental sensing". *Sensor Actuat a-Phys*, 2007. **136** (1), 69-79.

[57] M. Yamada and M. Seki, "Nanoliter-sized liquid dispenser array for multiple biochemical analysis in microfluidic devices". *Anal Chem*, 2004. **76** (4), 895-899.

[58] W. Z. Song and D. Psaltis, "Pneumatically tunable optofluidic dye laser". *Appl Phys Lett*, 2010. **96** (8).

[59] Y. Xu,C. W. Chiu,F. K. Jiang,Q. Lin and Y. C. Tai, "A MEMS multi-sensor chip for gas flow sensing". *Sensor Actuat a-Phys*, 2005. **121** (1), 253-261.

[60] P. Enoksson,G. Stemme and E. Stemme, "A silicon resonant sensor structure for Coriolis mass-flow measurements". *J Microelectromech S*, 1997. **6** (2), 119-125.

[61] R. W. Miller, *Flow Measurement Engineering handbook*. 3rd ed.; McGraw-Hill: 2006.

[62] B. Bae,B. R. Flachsbart,K. Park and M. A. Shannon, "Design optimization of a piezoresistive pressure sensor considering the output signal-to-noise ratio". *J Micromech Microeng*, 2004. **14** (12), 1597-1607.

[63] J. N. Palasagaram and R. Ramadoss, "MEMS-capacitive pressure sensor fabricated using printed-circuit-processing techniques". *Ieee Sens J*, 2006. **6** (6), 1374-1375.

[64] S. Calixto,F. J. Sanchez-Marin and M. Rosete-Aguilar, "Pressure sensor with optofluidic configuration". *Appl Optics*, 2008. **47** (35), 6580-6585.

[65] X. W. Wang,J. C. Xu,Y. Z. Zhu,K. L. Cooper and A. B. Wang, "All-fused-silica miniature optical fiber tip pressure sensor". *Opt Lett*, 2006. **31** (7), 885-887.

[66] Y. Kim and D. P. Neikirk, "Micromachined Fabry-Perot cavity pressure transducer". *Ieee Photonic Tech L*, 1995. **7** (12), 1471-1473.

[67] S. Mandal,J. M. Goddard and D. Erickson, "A multiplexed optofluidic biomolecular sensor for low mass detection". *Lab Chip*, 2009. **9** (20), 2924-2932.

[68] D. Dendukuri,S. S. Gu,D. C. Pregibon,T. A. Hatton and P. S. Doyle, "Stop-flow lithography in a microfluidic device". *Lab Chip*, 2007. **7** (7), 818-828.

[69] Z. G. Wu,B. Willing,J. Bjerketorp,J. K. Jansson and K. Hjort, "Soft inertial microfluidics for high throughput separation of bacteria from human blood cells". *Lab Chip*, 2009. **9** (9), 1193-1199.

[70] H. Hufnagel,A. Huebner,C. Gulch,K. Guse,C. Abell and F. Hollfelder, "An integrated cell culture lab on a chip: modular microdevices for cultivation of mammalian cells and delivery into microfluidic microdroplets". *Lab Chip*, 2009. **9** (11), 1576-1582.

[71] X. Q. Cui,L. M. Lee,X. Heng,W. W. Zhong,P. W. Sternberg,D. Psaltis and C. H. Yang, "Lensless high-resolution on-chip optofluidic microscopes for Caenorhabditis elegans and cell imaging". *P Natl Acad Sci USA*, 2008. **105** (31), 10670-10675.

[72] S. Choi and J. K. Park, "Microfluidic Rheometer for Characterization of Protein Unfolding and Aggregation in Microflows". *Small*, 2010. **6** (12), 1306-1310.

[73] M. Abkarian,M. Faivre and H. A. Stone, "High-speed microfluidic differential manometer for cellular-scale hydrodynamics". *P Natl Acad Sci USA*, 2006. **103** (3), 538-542.

[74] M. J. Fuerstman,A. Lai,M. E. Thurlow,S. S. Shevkoplyas,H. A. Stone and G. M. Whitesides, "The pressure drop along rectangular microchannels containing bubbles". *Lab Chip*, 2007. **7** (11), 1479-1489.

[75] B. Kuczenski,P. R. LeDuc and W. C. Messner, "Pressure-driven spatiotemporal control of the laminar flow interface in a microfluidic network". *Lab Chip*, 2007. **7** (5), 647-649.

[76] G. F. Chen,F. Svec and D. R. Knapp, "Light-actuated high pressure-resisting microvalve for on-chip flow control based on thermo-responsive nanostructured polymer". *Lab Chip*, 2008. **8** (7), 1198-1204.

[77] N. Srivastava and M. A. Burns, "Microfluidic pressure sensing using trapped air compression". *Lab Chip*, 2007. **7** (5), 633-637.

[78] K. Chung,H. Lee and H. Lu, "Multiplex pressure measurement in microsystems using volume displacement of particle suspensions". *Lab Chip*, 2009. **9** (23), 3345-3353.

[79] H. Ernst,A. Jachimowicz and G. A. Urban, "High resolution flow characterization in bio-MEMS". *Sensor Actuat a-Phys*, 2002. **100** (1), 54-62.

[80] J. Collins and A. P. Lee, "Microfluidic flow transducer based on the measurement of electrical admittance". *Lab Chip*, 2004. **4** (1), 7-10.

[81] V. Lien and F. Vollmer, "Microfluidic flow rate detection based on integrated optical fiber cantilever". *Lab Chip*, 2007. **7** (10), 1352-1356.

[82] P. Domachuk,I. C. M. Littler,M. Cronin-Golomb and B. J. Eggleton, "Compact resonant integrated microfluidic refractometer". *Appl Phys Lett*, 2006. **88** (9).

[83] W. Z. Song and D. Psaltis, "Optofluidic pressure sensor based on interferometric imaging". *Opt Lett*, 2010. **35** (21), 3604-3606.

[84] W. Z. Song and D. Psaltis, "Imaging based optofluidic air flow meter with polymer interferometers defined by soft lithography". *Opt Express*, 2010. **18** (16), 16561-16566.

[85] D. Fuard,T. Tzvetkova-Chevolleau,S. Decossas,P. Tracqui and P. Schiavone, "Optimization of poly-di-methyl-siloxane (PDMS) substrates for studying cellular adhesion and motility". *Microelectron Eng*, 2008. **85** (5-6), 1289-1293.

[86] J. L. Rodgers and W. A. Nicewander, "13 Ways to Look at the Correlation-Coefficient". *Am Stat*, 1988. **42** (1), 59-66.

[87] C. Boor, *A Practical Guide to Splines* Springer-Verlag, New Yokr: 2001.

[88] J. H. a. H. Brenner, *Low Reynolds Number Hydrodynamics*. Prentice-Hall, New York: 1965.

[89] B. S. Hardy,K. Uechi,J. Zhen and H. P. Kavehpour, "The deformation of flexible PDMS microchannels under a pressure driven flow". *Lab Chip*, 2009. **9** (7), 935-938.

[90] D. V. Vezenov,B. T. Mayers,R. S. Conroy,G. M. Whitesides,P. T. Snee,Y. Chan,D. G. Nocera and M. G. Bawendi, "A low-threshold, high-efficiency microfluidic waveguide laser". *J Am Chem Soc***,** 2005. **127** (25), 8952-8953.

[91] S. K. Y. Tang,R. Derda,Q. M. Quan,M. Loncar and G. M. Whitesides, "Continuously tunable microdroplet-laser in a microfluidic channel". *Opt Express***,** 2011. **19** (3), 2204-2215.

[92] D. Erickson,T. Rockwood,T. Emery,A. Scherer and D. Psaltis, "Nanofluidic tuning of photonic crystal circuits". *Opt Lett***,** 2006. **31** (1), 59-61.

[93] J. Heikenfeld,K. Zhou,E. Kreit,B. Raj,S. Yang,B. Sun,A. Milarcik,L. Clapp and R. Schwartz, "Electrofluidic displays using Young-Laplace transposition of brilliant pigment dispersions". *Nat Photonics***,** 2009. **3** (5), 292-296.

[94] H. You and A. J. Steckl, "Three-color electrowetting display device for electronic paper". *Appl Phys Lett***,** 2010. **97** (2).

[95] K. S. Lee,S. B. Kim,K. H. Lee,H. J. Sung and S. S. Kim, "Three-dimensional microfluidic liquid-core/liquid-cladding waveguide". *Appl Phys Lett***,** 2010. **97** (2).

[96] A. R. Hawkins and H. Schmidt, "Optofluidic waveguides: II. Fabrication and structures". *Microfluid Nanofluid***,** 2008. **4** (1-2), 17-32.

[97] A. H. J. Yang,S. D. Moore,B. S. Schmidt,M. Klug,M. Lipson and D. Erickson, "Optical manipulation of nanoparticles and biomolecules in sub-wavelength slot waveguides". *Nature***,** 2009. **457** (7225), 71-75.

[98] A. Llobera,V. J. Cadarso,M. Darder,C. Dominguez and C. Fernandez-Sanchez, "Full-field photonic biosensors based on tunable bio-doped sol-gel glasses". *Lab Chip***,** 2008. **8** (7), 1185-1190.

[99] K. Campbell,A. Groisman,U. Levy,L. Pang,S. Mookherjea,D. Psaltis and Y. Fainman, "A microfluidic 2x2 optical switch". *Appl Phys Lett***,** 2004. **85** (25), 6119-6121.

[100] Y. C. Seow,S. P. Lim and H. P. Lee, "Tunable optofluidic switch via hydrodynamic control of laminar flow rate". *Appl Phys Lett***,** 2009. **95** (11).

[101] N. T. Nguyen,T. F. Kong,J. H. Goh and C. L. N. Low, "A micro optofluidic splitter and switch based on hydrodynamic spreading". *J Micromech Microeng*, 2007. **17** (11), 2169-2174.

[102] J. J. Shi,Z. Stratton,S. C. S. Lin,H. Huang and T. J. Huang, "Tunable optofluidic microlens through active pressure control of an air-liquid interface". *Microfluid Nanofluid*, 2010. **9** (2-3), 313-318.

[103] J. E. Fouquet, "Progress in optical cross-connects for circuit-switched applications". *Osa Trends Opt Photo*, 2000. **32**, 14-16.

[104] P. Yager,T. Edwards,E. Fu,K. Helton,K. Nelson,M. R. Tam and B. H. Weigl, "Microfluidic diagnostic technologies for global public health". *Nature*, 2006. **442** (7101), 412-418.

[105] S. Haeberle and R. Zengerle, "Microfluidic platforms for lab-on-a-chip applications". *Lab Chip*, 2007. **7** (9), 1094-1110.

[106] H. Y. Zhu,O. Yaglidere,T. W. Su,D. Tseng and A. Ozcan, "Cost-effective and compact wide-field fluorescent imaging on a cell-phone (vol 11, pg 315, 2011)". *Lab Chip*, 2011. **11** (24), 4279-4279.

[107] C. Dongre,J. van Weerd,G. A. J. Besselink,R. M. Vazquez,R. Osellame,G. Cerullo,R. van Weeghel,H. H. van den Vlekkert,H. J. W. M. Hoekstra and M. Pollnau, "Modulation-frequency encoded multi-color fluorescent DNA analysis in an optofluidic chip". *Lab Chip*, 2011. **11** (4), 679-683.

[108] I. Choi,Y. S. Huh and D. Erickson, "Size-selective concentration and label-free characterization of protein aggregates using a Raman active nanofluidic device". *Lab Chip*, 2011. **11** (4), 632-638.

[109] J. J. Ou,T. Glawdel,C. L. Ren and J. Pawliszyn, "Fabrication of a hybrid PDMS/SU-8/quartz microfluidic chip for enhancing UV absorption whole-channel imaging detection sensitivity and application for isoelectric focusing of proteins". *Lab Chip*, 2009. **9** (13), 1926-1932.

[110] J. Steigert,M. Grumann,T. Brenner,L. Riegger,J. Harter,R. Zengerle and J. Ducree, "Fully integrated whole blood testing by real-time absorption measurement on a centrifugal platform". *Lab Chip*, 2006. **6** (8), 1040-1044.

[111] J. M. Lim,S. H. Kim,J. H. Choi and S. M. Yang, "Fluorescent liquid-core/air-cladding waveguides towards integrated optofluidic light sources". *Lab Chip*, 2008. **8** (9), 1580-1585.

[112] A. Llobera,S. Demming,H. N. Joensson,J. Vila-Planas,H. Andersson-Svahn and S. Buttgenbach, "Monolithic PDMS passband filters for fluorescence detection". *Lab Chip*, 2010. **10** (15), 1987-1992.

[113] K. S. Lee,H. L. T. Lee and R. J. Ram, "Polymer waveguide backplanes for optical sensor interfaces in microfluidics". *Lab Chip*, 2007. **7** (11), 1539-1545.

[114] P. D. Ohlsson,O. Ordeig,K. B. Mogensen and J. P. Kutter, "Electrophoresis microchip with integrated waveguides for simultaneous native UV fluorescence and absorbance detection". *Electrophoresis*, 2009. **30** (24), 4172-4178.

[115] A. Prabhakar and S. Mukherji, "Microfabricated polymer chip with integrated U-bend waveguides for evanescent field absorption based detection". *Lab Chip*, 2010. **10** (6), 748-754.

[116] A. Llobera,S. Demming,R. Wilke and S. Buttgenbach, "Multiple internal reflection poly(dimethylsiloxane) systems for optical sensing". *Lab Chip*, 2007. **7** (11), 1560-1566.

[117] P. Fei,Z. He,C. H. Zheng,T. Chen,Y. F. Men and Y. Y. Huang, "Discretely tunable optofluidic compound microlenses". *Lab Chip*, 2011. **11** (17), 2835-2841.

[118] S. Xiong,A. Q. Liu,L. K. Chin and Y. Yang, "An optofluidic prism tuned by two laminar flows". *Lab Chip*, 2011. **11** (11), 1864-1869.

[119] H. Huang,X. L. Mao,S. C. S. Lin,B. Kiraly,Y. P. Huang and T. J. Huang, "Tunable two-dimensional liquid gradient refractive index (L-GRIN) lens for variable light focusing". *Lab Chip*, 2010. **10** (18), 2387-2393.

[120] C. Song,N. T. Nguyen,S. H. Tan and A. K. Asundi, "Modelling and optimization of micro optofluidic lenses". *Lab Chip*, 2009. **9** (9), 1178-1184.

[121] M. Rosenauer and M. J. Vellekoop, "3D fluidic lens shaping-A multiconvex hydrodynamically adjustable optofluidic microlens". *Lab Chip*, 2009. **9** (8), 1040-1042.

[122] Y. Yang,A. Q. Liu,L. Lei,L. K. Chin,C. D. Ohl,Q. J. Wang and H. S. Yoon, "A tunable 3D optofluidic waveguide dye laser via two centrifugal Dean flow streams". *Lab Chip*, 2011. **11** (18), 3182-3187.

[123] E. Roy,J. C. Galas and T. Veres, "Thermoplastic elastomers for microfluidics: Towards a high-throughput fabrication method of multilayered microfluidic devices". *Lab Chip*, 2011. **11** (18), 3193-3196.

[124] C. H. J. Schmitz,A. C. Rowat,S. Koster and D. A. Weitz, "Dropspots: a picoliter array in a microfluidic device". *Lab Chip*, 2009. **9** (1), 44-49.

[125] K. Mawatari,T. Ohashi,T. Ebata,M. Tokeshi and T. Kitamori, "Thermal lens detection device". *Lab Chip*, 2011. **11** (17), 2990-2993.

[126] J. Schafer,J. P. Mondia,R. Sharma,Z. H. Lu,A. S. Susha,A. L. Rogach and L. J. Wang, "Quantum dot microdrop laser". *Nano Lett*, 2008. **8** (6), 1709-1712.

[127] S. Bedo,W. Luthy and H. P. Weber, "The Effective Absorption-Coefficient in Double-Clad Fibers". *Opt Commun*, 1993. **99** (5-6), 331-335.

[128] S. R. Gallagher and P. R. Desjardins, Quantitation of DNA and RNA with Absorption and Fluorescence Spectroscopy. In *Current Protocols in Protein Science*, John Wiley & Sons, Inc.: 2001.

[129] J. P. Shelby,J. White,K. Ganesan,P. K. Rathod and D. T. Chiu, "A microfluidic model for single-cell capillary obstruction by Plasmodium falciparum infected erythrocytes". *P Natl Acad Sci USA*, 2003. **100** (25), 14618-14622.

[130] Y. Z. Sun,C. S. Wu and X. D. Fan, "Optofluidic FRET dye laser controlled by DNA scaffolds". *Integrated Optics: Devices, Materials, and Technologies Xiv*, 2010. **7604**.

[131] F. M. Huang and J. J. Baumberg, "Actively Tuned Plasmons on Elastomerically Driven Au Nanoparticle Dimers". *Nano Lett*, 2010. **10** (5), 1787-1792.

[132] I. M. Pryce,K. Aydin,Y. A. Kelaita,R. M. Briggs and H. A. Atwater, "Highly Strained Compliant Optical Metamaterials with Large Frequency Tunability". *Nano Lett*, 2010. **10** (10), 4222-4227.

[133] G. Lu,H. Li and H. Zhang, "Nanoparticle-coated PDMS elastomers for enhancement of Raman scattering". *Chem Commun*, 2011. **47** (30), 8560-8562.

[134] D. Huh,K. L. Mills,X. Y. Zhu,M. A. Burns,M. D. Thouless and S. Takayama, "Tuneable elastomeric nanochannels for nanofluidic manipulation". *Nat Mater*, 2007. **6** (6), 424-428.

[135] W. Z. Song and D. Psaltis, "Pressure mediated tunable elastomeric optofluidic devices". *Microfluidics, Biomems, and Medical Microsystems Viii*, 2010. **7593**.

[136] J. Sansregret,J. M. Drake,W. R. L. Thomas and M. L. Lesiecki, "Light Transport in Planar Luminescent Solar Concentrators - the Role of Dcm Self-Absorption". *Appl Optics*, 1983. **22** (4), 573-577.

[137] S. Grilli,L. Miccio,V. Vespini,A. Finizio,S. De Nicola and P. Ferraro, "Liquid micro-lens array activated by selective electrowetting on lithium niobate substrates". *Opt Express*, 2008. **16** (11), 8084-8093.

[138] E. Ozbay, "Plasmonics: Merging photonics and electronics at nanoscale dimensions". *Science*, 2006. **311** (5758), 189-193.

[139] A. N. Grigorenko,N. W. Roberts,M. R. Dickinson and Y. Zhang, "Nanometric optical tweezers based on nanostructured substrates". *Nat Photonics*, 2008. **2** (6), 365-370.

[140] M. L. Juan,M. Righini and R. Quidant, "Plasmon nano-optical tweezers". *Nat Photonics*, 2011. **5** (6), 349-356.

[141] J. Kneipp,H. Kneipp and K. Kneipp, "SERS - a single-molecule and nanoscale tool for bioanalytics". *Chem Soc Rev*, 2008. **37** (5), 1052-1060.

[142] J. C. T. Eijkel and A. van den Berg, "Nanofluidics: what is it and what can we expect from it?". *Microfluid Nanofluid*, 2005. **1** (3), 249-267.

[143] M. Krishnan,N. Mojarad,P. Kukura and V. Sandoghdar, "Geometry-induced electrostatic trapping of nanometric objects in a fluid". *Nature*, 2010. **467** (7316), 692-U75.

[144] W. Reisner,N. B. Larsen,H. Flyvbjerg,J. O. Tegenfeldt and A. Kristensen, "Directed self-organization of single DNA molecules in a nanoslit via embedded nanopit arrays". *P Natl Acad Sci USA*, 2009. **106** (1), 79-84.

Appendix

With the financial support from FESTO Germany, we have developed a demo for the optofluidic pressure/flow meter. As shown in Fig.1, the device was assembled by commercial standard opto-mechanic components from Thorlabs. It was powered by a USB cable. The images were captured and transmitted to stand-alone software on computer for calculating pressure in real-time.

We have tested the device with different liquids, obtaining accuracy of about ±1% in the full scale of 0–1.5 bars. The core component of disposable pressure sensor is a flexible polymer membrane which has the size of 1 mm. Thanks to the remote imaging method; the sensing membrane has no physical contact with the monitor. This scheme is different from the traditional disposable diaphragm domes hence it avoids potential error and improves the accuracy. It also has fast dynamic response that mainly depends on the frame rate of CMOS camera (30 FPS).

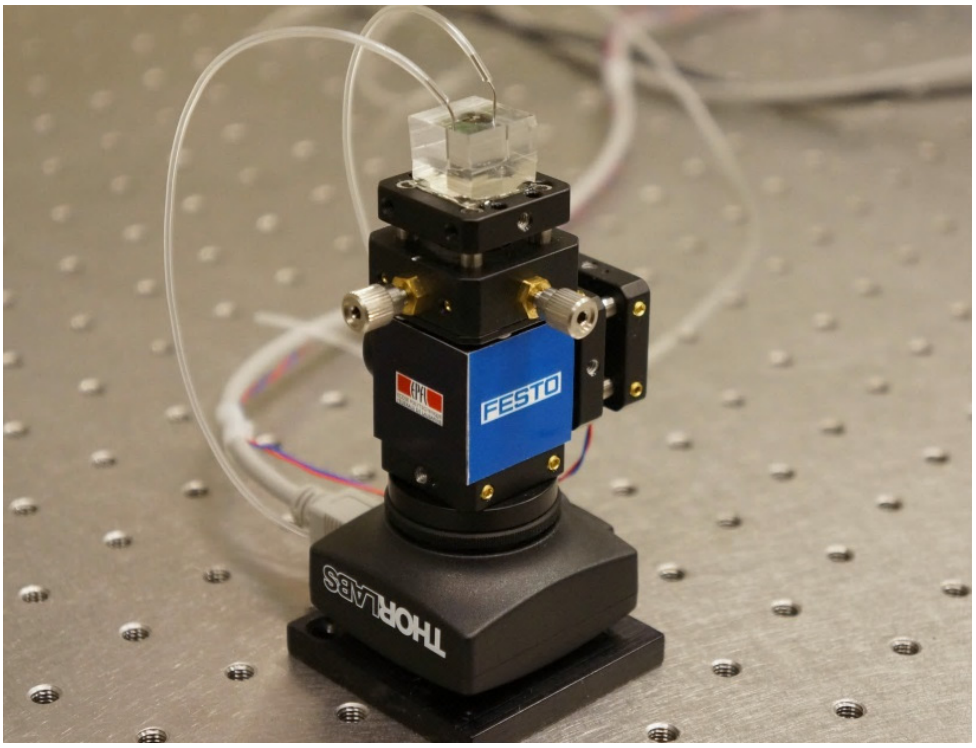

Figure 1: The demo contains a monitor and a microfluidic chip.

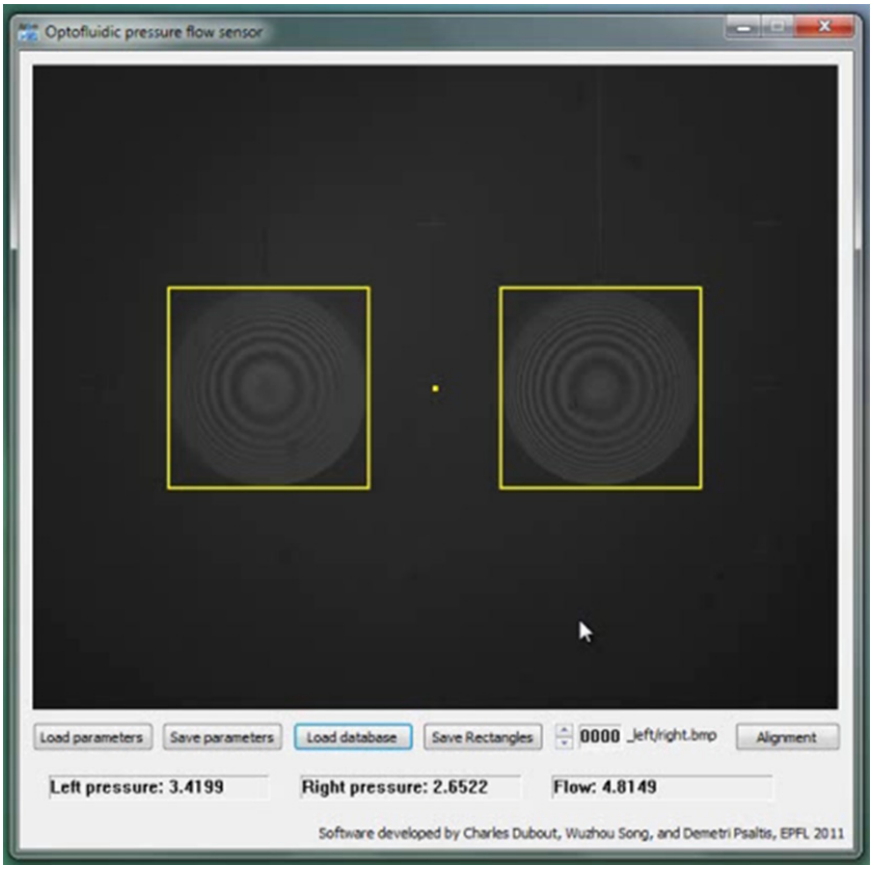

Figure 2: The graphic interface of the software for the demo.

User manual for imaging based optofluidic pressure/flow sensor

1. Installation

1.1 Install the camera diver provided by Thorlabs. Then move the software “Optofluidic” to any folder in the user’s harddisk.

1.2 Mount the sensor chip. Pay attention to mount the chip according to the markers on the chip and monitor.

2. Calibration

2.1 Connect the camera to computer. Run the software.

2.2 Click the button “Alignment” to center the capture area (indicated by two yellow squares). The alignment is based on the cross marker in the center of the chip.

2.3 Save parameter file by click “Save parameter”. As each of such file will corresponds to a different chip, so it is recommended to name the file with a number corresponding to the chip.

2.4 Adjust the applying pressure, choose the value of the pressure (**or an equivalent value depending on the pressure with a linear relationship**), then click “Save rectangular”. For first time to start the software, it will ask for the folder path to store such image files as reference library. Each library will correspond to different single chip.

2.5 Repeat above step to add more images in the library folder. The more then better, and two nearby images should be close, otherwise the interpolation won’t work well and the measuring value can be fault.

2.6 Edit the parameter file, the detail will be shown in remark.

3. Make measurement

Start the software, load the parameter file, click “Alignment”, and then load the reference images library by click “Load database”. The measuring values will display in real-time on the bottom of the software window.

4. Remark

Open the parameter file, modify the value and save. Then load the parameter in the software.

$$p_1 = k_1 p_1 + m_1$$
$$p_2 = k_2 p_2 + m_2$$

Where p1 is the file number of the images in the library (left rectangle), such 0003, 0008…. P1 is the real pressure which is displayed on the software interface. p2 and P2 corresponds to the right

rectangle. Before the measurement of the pressures, p1, P1, p2, P2 should be modified according to the calibration results.

The flow rate is calculated according to the following formula. For gas/air flow rate, n2 should be zero. For liquid flow rate, n1 and n4 should be zero. These values can be obtained from the calibration.

$$Flow = n_1\sqrt{P_1\left|P_1 - P_2\right|} + n_2\left(P_1 - P_2\right) + n_3 + n_4\sqrt{P_2\left|P_2 - P_1\right|}$$

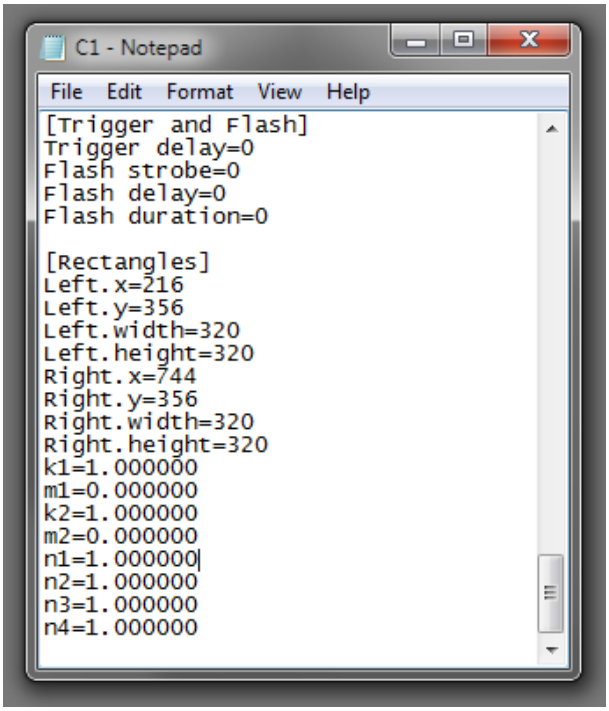

Figure 3: The graphic interface for parameter setting.

Curriculum Vitae

Name: Wuzhou Song
Nationality: Chinese
Email: songwuzhou@gmail.com

Education

- Sept 2001- June 2005: *Bachelor of Physics*, School of Physics and Technology, Wuhan University, Wuhan, China.
- July 2005-June 2007: *Master of Science in Photonics*, Microelectronic Division, School of Electrical & Electronic Engineering, Nanyang Technological University (NTU), Singapore
- Oct 2007 – Aug 2012: *Research assistant & PhD candidate of Photonics program*, Optics Laboratory (LO), Swiss Federal Institute of Technology Lausanne (EPFL), Switzerland.

Research experience

- August 2005-April 2006: Working on optical MEMS and integrated optics in Photonics research center, Nanyang Technological University.
- April 2006-Sep 2007: Hold the position of Project officer. Working on optofluidics.
- Oct 2007-Present: Working on optofluidics, microfluidic and nano-fluidic, micro and nano fabrication, integrated optics, lasers, optical MEMS, lab on a chip, nano-particles, single molecule, Raman (SERS) spectroscopy, microscopy and optofluidic solar lighting.

Awards

- SNSF (Swiss National Science Foundation) *Respective Researcher Fellowship* 2012-2014
- 2010 *Chinese Government Award for Outstanding Self-financed Chinese Students Study Abroad* (500 Chinese PhD students obtained this award each year in world)
- IES (Institution of Engineers, Singapore) *Prestigious Engineering Achievement Awards* 2006 for "Photonics MEMS Chips & Application". (Less than 10 group winners each year in Singapore)

- Top two prize of *National Physics Competition of senior high school of China* in 1999 and 2000.

Publications

---

1. Ning Wang , Xuming Zhang, Bolei Chen, **Wuzhou Song**, Ngai Yui Chan and Helen L. W. Chan "Microfluidic photoelectrocatalytic reactors for water purification with integrated visible-light source" Lab on a chip (Advance paper, DOI: 10.1039/C2LC40428A)
2. **Wuzhou Song**, Andreas E. Vasdekis and Demetri Psaltis "Elastomer based optofluidic devices" ***Lab on a chip*** (Advance paper, DOI: 10.1039/C2LC40481H)
3. **Wuzhou Song** and Jianhang Yang. "Optofluidic differential spectroscopy for absorbance detection of sub-nanoliter liquid sample" ***Lab on a chip*** 12, 1251-1254 (2012)
4. **Wuzhou Song,** Demetri Psaltis. "Optofluidic membrane interferometer: An imaging method for measuring microfluidic pressure and flow rate simultaneously on a chip" ***Biomicrofluidics*** 5, 044110 (2011)
5. **Wuzhou Song**, Demetri Psaltis. "Pneumatically tunable optofluidic 2×2 switch for reconfigurable optical circuit" ***Lab on a Chip*** 11, 2397-2402 (2011)
6. **Wuzhou Song**, Demetri Psaltis. "Optofluidic pressure sensor based on interferometric imaging" ***Optics Letters***,Vol.35,Issue 21, pp.3604 (2010)
7. **Wuzhou Song**, Demetri Psaltis. "Imaging based optofluidic air flow meter with polymer interferometers defined by soft lithography" ***Optics Express***, Vol. 18, Issue 16, pp. 16561-16566 (2010)) (Highlighted by "*Nature Photonics"* : Research Highlight)
8. **Wuzhou Song**, Demetri Psaltis. "Pneumatically tunable optofluidic dye laser " ***Appl. Phys. Letts***, Vol.96, 081101 (2010) (Cover letter) (Highlighted by "Nature Photonics": News and Views)
9. **Wuzhou Song**, Andreas E. Vasdekis, Zhenyu Li, Demetri Psaltis. "Optofluidic evanescent dye laser based on a distributed feedback circular grating" ***Appl. Phys. Letts***, Vol.94,161110 (2009)

10. **Wuzhou Song**, Andreas E. Vasdekis, Zhenyu Li, Demetri Psaltis. “Low-order distributed feedback optofluidic dye laser with reduced threshold”. ***Appl. Phys. Letts***, Vol. 94, 051117 (2009)
11. **W. Z. Song**, A. Q. Liu, S. Swaminathan C. S. Lim, P. H. Yap and T. C. Ayi “Determination of cell’s dry/water mass using optofluidic chip” ***Appl. Phys. Letts***, Vol.91, 223902(2007) (Reviewed by “*BioPhotonics International” 2008, Feb, Page 50-51*)
12. **W. Z. Song** , X. M. Zhang, A. Q. Liu , Peng Huat Yap , Habib Hosseini, “Refractive index measurement of single living cells using on-chip Fabry-Perot cavity”, ***Appl. Phys. Letts***, Vol. 89, 203901(2006)
13. L. Liao, J. C. Li, D. H. Liu, C. Liu, D. F. Wang, **W. Z. Song** and Q. Fu, “Self-assembly of aligned ZnO nanoscrew: Synthesis, configuration, growth mechanism and field emission property”, ***Appl. Phys. Letts***, Vol.86,083106 (2009)

Patent

---

1. **Wuzhou Song**, Demetri Psaltis. “Imaging based interferometric pressure sensor” ***International patent***, PCT/IB2010/054890 and WO2011051903. (US and European patent, We have sold a prototype of this device to FESTO Germany at a price of 30K CHF last year for the purpose of evaluation)

Conferences

---

1. **Wuzhou Song** and Demetri Psaltis. "Tunable optofluidic light switch for reconfigurable solar indoor lighting" **2nd International Conference on Optofluidics**. 2012, Suzhou China. Sep 13-15.
2. Demetri Psaltis and **Wuzhou Song**. "Optofluidic devices and applications" **1th International Conference on Optofluidics**. 2011, Xi'an China. Dec 11-13 (Invited talk)

3. **Wuzhou Song** and Demetri Psaltis. "Optofluidic lock-in spectroscopy on a chip" ***31th Conference on Lasers and Electro Optics (CLEO). 2011, Baltimore***, US. May 1-6 (Oral presentation
4. Andreas E. Vasdekis, **Wuzhou Song**, Julien R. Cuennet, Luciano De Sio, Jae-Woo Choi, Demetri Psaltis. "Surface Optofluidics", ***2010 OSA Annual Meetings - Frontiers in Optics***, Rochester, NY, USA (Invited talk)
5. A.E. Vasdekis, J.G. Cuennet, **W.Z. Song**, J.W. Choi, L. De Sio, C.P. O'Neil, J.A. Hubbell and D. Psaltis. "Surface optofluidics", ***2010 SPIE Optics and Photonics***, San Diego, CA, USA (oral presentation)
6. **Wuzhou Song**, and Demetri Psaltis. "Imaging based optofluidic interferometer on chip" ***30th Conference on Lasers and Electro Optics (CLEO) 2009***, San Jose, California. May 16-21,2009 (Oral presentation)
7. Demetri Psaltis, **Wuzhou Song**, Jae-Woo Choi. "Tuning Mechanisms in Optofluidics"***30th Conference on Lasers and Electro Optics (CLEO) 2009***, San Jose, California. May 16-21,2009 (Invited talk)
8. **Wuzhou Song**, Demetri Psaltis. "Novel tuning methods for optofluidics" ***ISOT2009 International Symposium on Optomechatronic Technologies***, 21-23 Sep 2009, Istanbul, Turkey (Invited talk)
9. **Wuzhou Song**, Demetri Psaltis. "Pressure mediated tunable elastomeric optofluidic devices**"** ***SPIE Photonics West MOEMS-MEMS***. 23-28 Jan 2010, San Francisco, California. (Oral presentation)
10. **Wuzhou Song**, Andreas E. Vasdekis, Demetri Psaltis. "Tunable optofluidic dye laser with novel cavity" ***SPIE Photonics West MOEMS-MEMS***. 23-28 Jan 2010, San Francisco, California. (Oral presentation)
11. **Wuzhou Song**, Andreas E. Vasdekis, Demetri Psaltis. "Optofluidic distributed feedback dye laser via evanescent gain" ***SPIE Photonics LASE-Lasers and Application***. 23-28 Jan 2010,

San Francisco, California. (Oral presentation)

12. **Wuzhou Song**, Andreas E. Vasdekis, Demetri Psaltis. “Tunable optofluidic devices using Micro-Air-Bag" ***3rd EOS Topical Meeting on Optical Microsystems*** (OμS’09)2009, Capri, Italy. Sep 27.(Oral presentation)
13. **Wuzhou Song**, Andreas E. Vasdekis, Demetri Psaltis. “Tunable optofluidic dye laser with integrated air-gap etalon" ***ICO Photonics 2009***, Delphi, Greece.Oct 7-9.(Oral presentation)
14. **Wuzhou Song**, Andreas E. Vasdekis, Jae Woo Choi, and Demetri Psaltis. "Micro-Air-Bag Actuated Tunable Optofluidic Elements" ***29th Conference on Lasers and Electro Optics (CLEO)***. 2009, Baltimore, US. May 31-Jun 5 (Oral presentation)
15. **Wuzhou Song**, Andreas E. Vasdekis, and Demetri Psaltis. "Optofluidic Evanescent Dye Laser" European Conference on Lasers and Electro-Optics and the ***XIth European Quantum Electronics Conference 2009 (CLEO Europe 2009)***, Jun 14-19, Munich, Germany. (Oral presentation)
16. Luciano De Sio, Andreas E. Vasdekis, **Wuzhou Song** and Demetri Psaltis, "A novel fluidic control system for the optofluidic microscope ", ***9th Mediterranean Workshop and Topical Meeting Novel Optical Materials and Applications***, June 07-13,2009. Cetraro, Italy.
17. **Wuzhou Song**, Andreas E. Vasdekis, Demetri Psaltis. “Low threshold optofluidic dye laser for lab-on-a-chip application”. ***The 12th Annual European Conference on Micro & Nanoscale Technologies for the Biosciences*** (Nanotech Montreux). November 17-19, 2008 Switzerland.
18. **Wuzhou Song**, Andreas E. Vasdekis, Zhenyu Li, Demetri Psaltis. “Nanostructured optofluidic dye lasers”. ***2nd European Topical Meeting on Nanophotonics and Metamaterials***. 5 - 8 January 09, Seefeld Tirol, Austria.
19. **W. Z. Song**, A. Q. Liu, C. S. Lim and P. H. Yap, “Optofluidic spectrometer for microchip flow cytometry”, ***μTAS2007(11th International Conference on Miniaturized Systems for Chemistry and Life Sciences)***, October 7-11, 2007, Paris, France. (Oral presentation)

20. X. Zhang, R. Chua, P. H. Yap, **W. Z. Song** and A. Q. Liu "Immersion refractometry analysis of living cells in microfluidic cell culture chip", ***μTAS2007 (11th International Conference on Miniaturized Systems for Chemistry and Life Sciences)***, October 7-11, 2007, Paris, France.
21. **W. Z. Song**, A. Q. Liu, and P. H. Yap, "Optical detection of living cells' refractive index using microfluidic chip via modulated buffer", ***μTAS2006(10th International Conference on Miniaturized Systems for Chemistry and Life Sciences)***, 5-9 November, 2006, Tokyo, Japan. (**Oral** presentation)
22. **W. Z. Song**, A. Q. Liu, C. S. Lim, and P. H. Yap,"A Micro-Optic-Fluidic Spectrometer with Integrated 3D Liquid-Liquid Waveguide", ***OMENS2007(IEEE/LEOS International Conference on Optical MEMS and Nanophotonics)***, August 12-16, Taiwan, Hualien.(Oral presentation)
23. **W. Z. Song**, C. S. Lim, A. Q. Liu and P. H. Yap, "Differential Mach-Zehnder interferometer for simultaneously determining size and refractive index of living cells". ***Transducer 2007 (The 14th International Conference on Solid-state Sensors, Actuators and Microsystems)***, June 2007, Lyon, France.
24. **W. Z. Song**, C. S. Lim, P. H. Yap and A. Q. Liu, "Optofluidic Mach-Zehnder interferometer for simultaneously determining size and refractive index of living cells". ***ICMAT2007(International conference on materials for advanced technologies)***, June 1-6, 2007, Singapore.(Oral presentation)
25. **W. Z. Song**, X. M. Zhang and A. Q. Liu, "Theoretical and experimental studies of polarization dependence loss of shutter type MEMS VOAs", ***APCOT2006 (Asia Pacific Conference of Transducers and Micro-Nano Technology)***, 25-28 June 2006, Singapore.